UNIVERSITÀ DELLA CALABRIA

UNIVERSITA' DELLA CALABRIA

Dipartimento di Fisica

Dottorato di Ricerca in

Scienze e Tecnologie Fisiche, Chimiche e dei Materiali
in convenzione con il CNR

CICLO

XXXI

PARTICLE ACCELERATION AT SHOCKS AND MAGNETIC TURBULENCE IN THE INTERPLANETARY SPACE

Settore Scientifico Disciplinare FIS - 06

Coordinatore: Prof. Vincenzo Carbone

Vincenzo Carbone

Supervisore: Dr. Fabio Lepreti

Fabio Lepreti

Dottorando: Dott.ssa Federica Chiappetta

Federica Chiappetta

Sommario

Il vento solare è un flusso di plasma supersonico e super-alfvénico di origine solare che si propaga nello spazio fino alla Terra e nel resto dell'eliosfera raggiungendo velocità di circa $400 - 800\ \mathrm{km \cdot s^{-1}}$. Esso permea l'intera eliosfera e rappresenta un fantastico laboratorio per la fisica del plasma, in quanto è l'unico ambiente astrofisico in cui le sonde possono misurare in situ i parametri fisici rilevanti. Il plasma del vento solare trasporta con sé il campo magnetico del Sole generando nello spazio un campo magnetico interplanetario. L'interazione del campo interplanetario con quello terrestre determina la formazione di una magnetosfera, nella quale il campo magnetico della Terra è confinato, delimitata da una discontinuità tra i due campi, detta magnetopausa. Il magnetismo è alla base della maggior parte dei fenomeni che vengono osservati nei vari strati dell'atmosfera solare, raggruppati sotto il nome di attività solare. I brillamenti (flares) e le espulsioni di massa coronale (CMEs) sono alcune della manifestazioni più spettacolari e più interessanti dell'attività solare che possono generare onde di shock (shock waves) nello spazio interplanetario. Uno shock è una discontinuità, caratterizzata da un brusco cambiamento in pressione, temperatura e densità del mezzo.
I brillamenti solari e le CMEs possono rilasciare particelle energetiche (Solar Energetic Particles - SEPs) che viaggiano con una velocità maggiore di quella delle particelle già presenti nel plasma spaziale. Le SEPs, seguendo il campo magnetico interplanetario, possono raggiungere la Terra in un'ora o anche meno e sono di particolare interesse perché, specialmente le particelle con energia maggiore di 40 MeV, possono provocare danni alla strumentazione elettronica a bordo delle sonde spaziali, influenzare le comunicazioni e i sistemi di navigazione e mettere a rischio la vita degli astronauti in orbita.
Durante la sua espansione, il vento solare sviluppa un forte carattere turbolento, che evolve verso un stato simile a quello della turbolenza idrodinamica,

descritta da Kolmogorov (1941). Le fluttuazioni a bassa frequenza nel vento solare vengono generalmente descritte dalla magnetoidrodinamica (MHD). La turbolenza magnetoidrodinamica nel vento solare è stata studiata in grande dettaglio negli ultimi anni, grazie alle numerose sonde spaziali che si sono inoltrate nello spazio interplanetario dall'inizio dell'era spaziale.

Questo lavoro di tesi riguarda lo studio delle particelle energetiche (in particolare protoni) agli shock interplanetari, i meccanismi di accelerazione che le producono e la connessione con la turbolenza magnetica nelle regioni upstream e downstream degli shock.

In particolare, viene effettuata un'analisi di correlazione tra gli aumenti di flusso delle particelle energetiche e la turbolenza del campo magnetico osservata nelle regioni "upstream" e "downstream" degli shock interplanetari.
I dati analizzati sono stati acquisiti dalla sonda spaziale Stereo A e coprono un periodo che va dal 2009 al 2016. Gli shock interplanetari presi in esame sono stati divisi in due liste: la prima racchiude 24 eventi che mostrano un aumento di flusso a piccola distanza dallo shock stesso; la seconda, invece, comprende 14 eventi che presentano aumenti di flusso a maggiore distanza dallo shock. Per dare una misura quantitativa della turbolenza magnetica è stato utilizzato il total wave power, calcolato a partire dall'analisi spettrale. A causa della bassa correlazione ottenuta, gli eventi della prima lista sono stati suddivisi ulteriormente a seconda se gli shock si verificavano sulla scia o meno di un evento SEP. Al contrario, ciò non è stato possibile per gli shock della seconda lista visto il minor numero di eventi presenti.
Un'analisi di correlazione parametrica e non parametrica è stata effettuata anche per studiare il grado di compressibilità nelle regioni upstream e downstream degli shock interplanetari per entrambe le liste di eventi selezionati, utilizzando la varianza del campo magnetico.
Inoltre, per avere informazioni sulla propagazione e sull'accelerazione di particelle nello spazio interplanetario, sono stati studiati gli spettri di energia degli shock associati agli eventi SEP della prima lista. In particolare, è stato possibile individuare due tipi di distribuzione che fittano bene gli spettri analizzati: una distribuzione di tipo Weibull, ottenuta per gli shock quasi-perpendicolari e una doppia legge di potenza nel caso degli shock quasi-paralleli. Grazie anche allo studio combinato del flusso di protoni energetici con il numero di Mach e l'angolo tra il campo magnetico e la normale allo shock, è stato possibile individuare il meccanismo di accelerazione dello "shock surfing" come meccanismo capace di spiegare gli spettri di particelle agli shock interplanetari quasi-perpendicolari.

Infine, per quanto riguarda le fluttuazioni del campo magnetico nello spa-

zio interplanetario, è stata studiata la dinamica ad alte frequenze, un problema ancora aperto e non del tutto chiaro. Al contrario delle fluttuazioni magnetiche nel range di scale cinetiche, quelle a basse frequenze sono state ampiamente trattate e mostrano un comportamento di scala universale descritto nell'ambito della cascata turbolenta di energia.
A piccole scale (alte frequenze), invece, la dinamica del plasma nello spazio interplanetario è estremamente complessa, dal momento che mostra contemporaneamente un comportamento dispersivo e dissipativo. Perciò viene introdotto un approccio di tipo browniano che fornisce un quadro generale che unifica le diverse dinamiche presenti nelle fluttuazioni a piccola scala e permette di riprodurre con successo l'andamento degli spettri delle fluttuazioni osservate ad alte frequenze. Questo approccio permette un'interpretazione degli spettri magnetici osservati ad alta frequenza senza alcuna assunzione circa le relazioni di dispersione dalla teoria della turbolenza.

Abstract

The solar wind is a supersonic and super-alfvenic flow of plasma that propagates in space up to the Earth and throughout the heliosphere reaching speeds of about $400 - 800$ km $\cdot$ s^{-1}. It permeates the heliosphere and is a fantastic laboratory for plasma physics, since it is the only astrophysical environment in which spacecrafts can provide in situ measurements of the relevant physical parameters. Embedded within the solar wind plasma is the interplanetary magnetic field. The interaction of the interplanetary field with the magnetic field of the Earth determines the formation of a magnetosphere, in which the magnetic field of the Earth is confined, bounded by a discontinuity between the two fields, called magnetopause. Magnetic field is at the origin of most of the phenomena that are observed in the various layers of the solar atmosphere, called solar activity. Flares and coronal mass ejections (CMEs) are some of the most spectacular and interesting manifestations of solar activity that can generate shock waves in interplanetary space. A shock is a discontinuity, characterized by a sudden change in pressure, temperature and density of the medium.

Solar flares and CMEs can release energetic particles (Solar Energetic Particles - SEPs) that travel faster than the particles already present in the interplanetary space plasma. SEPs, following the interplanetary magnetic field, can reach the Earth in an hour or less and are of particular interest because they can cause damage to the electronic instruments on board the space probes, influence communications and navigation systems and endanger astronauts' life in orbit, especially the particles with energy greater than 40 MeV.

During its expansion, the solar wind develops a strong turbulent character, which evolves towards a state similar to that of hydrodynamic turbulence, described by Kolmogorov (1941). The low frequency fluctuations are generally described by magnetohydrodynamics (MHD). The magnetohydrodynamic

turbulence in the solar wind has been studied in great detail in recent years, thanks to the numerous spacecrafts that have been launched in the interplanetary space since the beginning of the space age.

This work concerns the study of energetic protons at interplanetary shocks, the related acceleration mechanisms and the connection to magnetic turbulence in the upstream and downstream regions of the shocks.

In particular, we performed a correlation analysis between the particle flux enhancements and the magnetic field turbulence observed in the upstream and downstream regions of interplanetary shocks.
The data used in the analysis are taken by the Stereo Ahead spacecraft and cover a period from 2009 to 2016. The interplanetary shocks selected are divided into two lists: the first contains 24 events that show an increase of the proton flux close to the shock itself; instead, the second includes 14 events that present flux enhancements more distant from the shocks. In order to quantify the magnetic field turbulence, we used the total wave power, calculated from the standard spectral analysis methods. Because of the low correlation obtained, in the case of the first list we separated shocks occurring on the wake of a SEP event from NO SEP events. On the contrary, this is not possible for the shocks of the second list due to the smaller number of events.
We also performed a parametric and non-parametric correlation analysis to study the degree of compressibility in the upstream and downstream regions of interplanetary shocks for both lists of selected events, using the variance of the magnetic field.
Moreover, in order to have information on the propagation and acceleration of particles in the interplanetary space, we studied the evolution of the particle energy spectra for shocks associated with the SEP events of the first list. In particular, we identify two types of distribution that well fit the spectra: a Weibull functional form, obtained for quasi-perpendicular shocks and a double power law in the case of quasi-parallel shocks. Thanks also to the combined study of the proton flux enhancements with the Mach number and the shock angle, we identify the shock surfing acceleration as the acceleration mechanism suitable to explain the particle spectra at interplanetary quasi-perpendicular shocks.

Finally, concerning fluctuations of the magnetic field in the interplanetary space, we studied high-frequency dynamics, a problem that is still open and not entirely clear. Unlike magnetic fluctuations in the range of kinetic scales, those at low frequencies have been extensively investigated and show a universal scaling behavior, described in the nonlinear turbulent energy cascade framework.

At small scales (high frequencies), instead, the plasma dynamics in the interplanetary space is extremely complex, since it exhibits simultaneously a dispersive and dissipative character. Therefore, we introduced a Brownian approach that provides a simple description of the high-frequency dynamics of magnetic fluctuations, which is able to successfully reproduce the spectra of the fluctuations observed at high frequencies. This framework allows an interpretation of the observed high frequency magnetic spectra with no assumptions about dispersion relations from plasma turbulence theory.

Contents

Chapter 1

The heliosphere

The solar wind is a stream of charged particles that is continuously released from the Sun and which pervades the interplanetary space and affects also the Earth's magnetosphere. The wind is produced by the expansion of the solar corona and, in its radial motion, carries with it the magnetic field of the Sun, giving rise to the interplanetary magnetic field, which permeates a region surrounding the Sun having dimensions of over 100 AU, called *heliosphere*.

1.1 Heliosphere

The heliosphere is the bubble-like region of space that contains the solar system, the solar magnetic field and the solar wind. The heliosphere partially deflects cosmic rays and it was previously thought that its shape is not perfectly spherical but elongated like the tail of a comet, molded by the ambient flow of the interstellar medium. However, recent observations showed that this model is incorrect and the heliosphere's shape is more complex.

The structure of the heliosphere depends on the interaction of two plasmas: the solar wind, which radially expands from the Sun at supersonic velocity (of the order of 400 $\mathrm{km} \cdot \mathrm{s}^{-1}$), and interstellar plasma (an ionized gas that fills the interstellar spaces) in motion with respect to the Sun at a speed of about 20 $\mathrm{km} \cdot \mathrm{s}^{-1}$. Both plasmas are permeated by magnetic fields (the interplanetary magnetic field and the interstellar magnetic field, respectively), so there exists a surface of separation (discontinuity) between them, because they can not merged. This surface, called *heliopause*, forms the boundary of the heliosphere. Because of the limited data available, it has not yet been possible to establish the real extension of the heliosphere.

The supersonic solar wind encountering the interstellar medium slows to a stop. The point where the solar wind becomes slower than the speed of sound

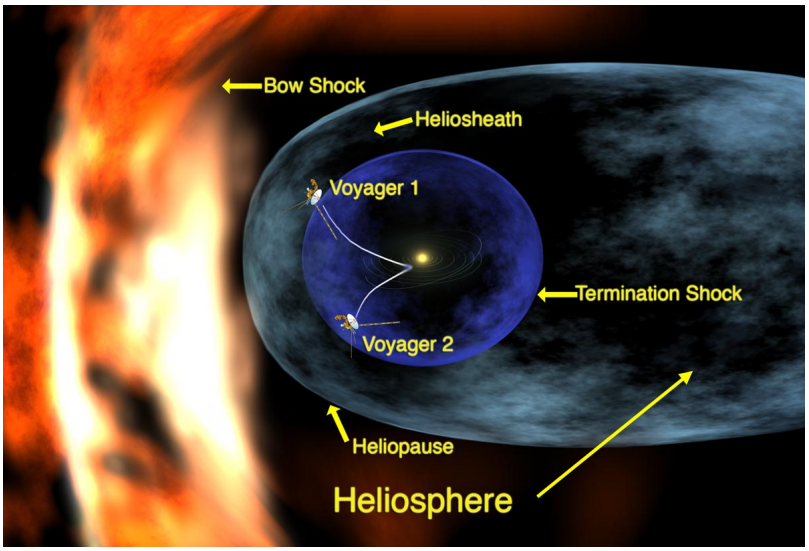

Figure 1.1: Diagram of the heliosphere as it travels through the interstellar medium. Image credit: `https://www.nasa.gov/`.

(subsonic) is called the *termination shock*, a standing shock wave; the solar wind continues to slow as it passes through a transitional region, called *heliosheath* leading to the heliopause, where the interstellar medium and solar wind pressures balance.

Heliospheric plasma mostly consists of ions and electrons. They extend from the lower regions of the solar corona to the interface of the heliosphere with the interstellar medium. To these particles are added also the Galactic Cosmic Rays (GCRs), which do not originate in the heliosphere but they come from interstellar space. There are different types of energetic populations: the population of the Solar Energetic Particles (SEPs) originating from the Sun; the Energetic Storm Particles (ESPs) associated to the Coronal Mass Ejections driven by shock waves; corotating energetic ion events related with the shocks surrounding the Corotating Interaction Regions (CIRs) in the solar wind; the Anomalous Cosmic Rays (ACRs) associated with termination shocks and which are outside the heliosphere.

1.1.1 Termination shock

The termination shock is the region of the heliosphere where the solar wind slows down to subsonic speed due to interactions with the interstellar medium (Local InterStellar Medium or LISM). This causes compression, heating, and a change in the magnetic field.
It is believed to be between 75 and 90 AU from the Sun. According to some observations presented by E.C. Stone at the meeting of the American Geophys-

ical Union of May 2005 (Stone et al., 2005), the Voyager 1 spacecraft passed the termination shock in December 2004, when it was about 94 AU from the Sun. Instead, the Voyager 2 began detecting returning particles when it was only 76 AU from the Sun, in May 2006. This implies that the heliosphere may be irregularly shaped, extending outwards in the Sun's northern hemisphere and pushed inward in the south.

The shock arises because solar wind particles are emitted from the Sun at about 400 $\mathrm{km} \cdot \mathrm{s}^{-1}$, while the speed of sound in the interstellar medium is about 100 $\mathrm{km} \cdot \mathrm{s}^{-1}$ (the exact speed depends on the density, which varies considerably). The interstellar medium, although not very dense, has an almost constant pressure; the pressure of the solar wind, on the other hand, decreases with the distance from the Sun. Thus, at a certain distance from the Sun, when the pressure of the solar wind drops cannot maintain anymore supersonic flow against the pressure of the interstellar medium, the solar wind slows to below its speed of sound, causing a shock wave.
A similar phenomenon is the *bow shock*, a shock wave that occurs when the interstellar wind hits the heliosphere. It slows down and creates a region of turbulence located on the border with the heliopause at a distance of 230 AU.

1.1.2 Heliosheath

The heliosheath is the region of the heliosphere beyond the termination shock. Here the solar wind is further slowed, compressed and made turbulent by its interaction with the interstellar medium. Its distance from the Sun is approximately between 80 and 100 AU and its thickness is estimated to be between 10 and 100 AU.

The Voyager 1 and Voyager 2 spacecraft have studied the heliosheath. Towards the end of 2010, Voyager 1 reached a region of the heliosheath where the solar wind's velocity had dropped to zero. The next year, it was announced that the Voyagers had determined that the heliosheath is not smooth, but is filled with 100 million-mile-wide bubbles created by the impact of the solar wind and the interstellar medium. Voyager 1 and 2 began detecting evidence for the bubbles in 2007 and 2008, respectively. The bubbles probably represent self-contained structures that have detached from the interplanetary magnetic field and they are formed by magnetic reconnection between oppositely oriented sectors of the solar magnetic field as the solar wind slows down.

1.1.3 Heliopause

The heliopause is the theoretical boundary where the Sun's solar wind is stopped by the interstellar medium. Here, the solar wind's strength is no longer great enough to push back the stellar winds of the surrounding stars. This is the boundary where the interstellar medium and solar wind pressures balance. The crossing of the heliopause should be signaled by an abrupt drop in the temperature of charged particles, a change in the direction of the magnetic field, and an increase in the number of galactic cosmic rays. In 2012, Voyager 1 detected a rapid increase in such cosmic rays, suggesting it was approaching the heliopause. In fact, after some months, NASA announced that Voyager 1 had crossed the heliopause and that it is at a distance of 121 AU from the Sun.

1.2 Solar wind

The hypothesis that the Sun emitted plasma clouds was already advanced in the first decades of the XX century by some geophysicists (K. Birkeland, S. Chapman, V.C.A. Ferraro) to explain the geomagnetic storms.
In 1951, the German scientist L. Biermann studied the comets and the fact that their tail always pointed in the opposite direction with respect to the Sun. He postulated that this was due to the Sun's emission of a constant stream of particles capable of push away some particles of the comet, forming its tail. In 1957, E.N. Parker provided the theoretical basis for such plasma stream, introducing the term *solar wind* to describe the phenomenon. Soon the observations provided by instruments on space probes clearly confirmed the existence of the solar wind and its magnetic field, demonstrating its fundamental role in the control of geomagnetic activity.
The solar wind has constantly been the object of interest of the scientific community, probably due to two important aspects. The first concerns its role in the Sun-Earth relations, in fact the solar wind is significantly influenced by changes in the solar magnetic field and transmits this influence to the planets, comets, cosmic rays that are in the wind itself. The second aspect concerns the physical processes that take place in the formation of the solar wind.

1.2.1 Solar wind properties

The solar wind is a stream of charged particles released from the solar corona. This plasma consists of mostly protons, electrons (about 95%) and 5% of alpha particles, with traces of nuclei of heavier elements.

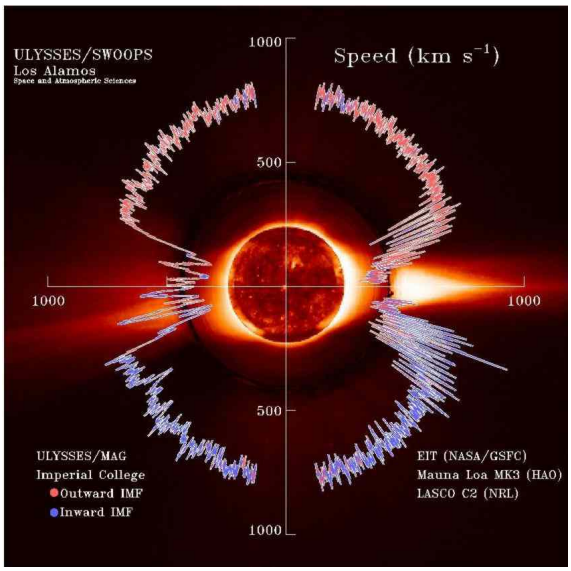

Figure 1.2: Ulysses observations of solar wind speed as a function of helio latitude during solar minimum. Image credit: `https://en.wikipedia.org/`.

Near the Earth, the speed of the solar wind varies from 400 km·s^{-1} to 700 km·s^{-1}, while its density varies from some units to tens of particles per cubic centimeter.

The solar wind is observed to exist in two fundamental states, represented in figure 1.2: the *slow solar wind*, mainly originating from a region around the Sun's equatorial belt, where magnetic field produces bright-loop like structures (coronal streamers), with speeds up to 400 km · s^{-1} at 1 AU, and the *fast solar wind*, coming from the coronal holes (characterized by open magnetic field lines), that travels at around 700 km · s^{-1}.

The most extensive and detailed observations of the solar wind were made by space probes near the Earth's orbit. Some of the physical properties of the plasma and the magnetic field at this distance from the Sun (1 AU = 1.5×10^{13} cm) are summarized in table 1.1a.

The pressure in an ionized gas with equal proton and electron density (n) is

$$p_{\text{gas}} = nk_B(T_p + T_e)\,,$$

where k_B is the Boltzmann constant, T_p and T_e are the proton and electron temperatures. Then

$$\begin{aligned} p_{\text{gas}} &= 3 \times 10^{-10}\text{dyn} \cdot \text{cm}^{-2} \\ &= 30\,\text{pPa}\,. \end{aligned}$$

Sound waves in an ionized gas with pressure p_{gas} and mass density $\rho = n(m_p +$

m_e), where m_p and m_e are the proton and electron masses respectively, travels at a speed

$$c_s = \left[\frac{\gamma p}{\rho}\right]^{\frac{1}{2}} = \left[\frac{\gamma k_B}{m_p + m_e}(T_p + T_e)\right]^{\frac{1}{2}},$$

where γ is the ratio of specific heats at a constant pressure and constant volume and c_s is the speed of sound. Using $\gamma = \frac{5}{3}$ for an ionized hydrogen gas and temperatures from table 1.1a, we find $c_s \approx 60\ \mathrm{km \cdot s^{-1}}$.
Consequently, the solar wind is highly supersonic beacause its speed ($400\ \mathrm{km \cdot s^{-1}}$) is almost an order of magnitude greater than c_s at 1 AU.
Furthermore, the presence of a magnetic field can lead to hydromagnetic effects. It exerts a pressure

$$p_{\mathrm{mag}} = \frac{B^2}{2\mu_0}$$

and using the average magnetic field reported in table 1.1a, we find a magnetic pressure near 1 AU of

$$\begin{aligned} p_{\mathrm{mag}} &\approx 1.5 \times 10^{-10} \mathrm{dyn \cdot cm^{-2}} \\ &\approx 15\,\mathrm{pPa}\,. \end{aligned}$$

This value is comparable to the gas pressure, indicating that magnetic effects will be as important as pressure effects in the solar wind plasma.

Proton density	$6.6\ \mathrm{cm^{-3}}$
Electron density	$7.1\ \mathrm{cm^{-3}}$
He^{2+} density	$0.25\ \mathrm{cm^{-3}}$
Flow speed	$450\ \mathrm{km \cdot s^{-1}}$
Proton temperature	1.2×10^5 K
Electron temperature	1.4×10^5 K
Magnetic field	7×10^{-9} T

(a)

Gas pressure	30 pPa
Sound speed	$60\ \mathrm{km \cdot s^{-1}}$
Magnetic pressure	19 pPa
Alfvén speed	$40\ \mathrm{km \cdot s^{-1}}$
Proton gyroradius	80 km
Proton-proton time collision	4×10^6 s
Electron-electron time collision	3×10^5 s

(b)

Table 1.1: Properties of the solar wind observed (a) and derived (b) near the Earth's orbit (1 AU).

To understand the origin of the solar wind, it is necessary to know some properties of the solar corona. The temperature of the Sun decreases from about 15×10^6 K in its core to about 5000 K on the visible surface of the Sun, where the atmosphere becomes thin enough to let the photons escape. At even higher heights in the atmosphere, the temperature rises again, coming back to around 10^6 K, and then it decreases very slowly as the height increases in the corona. This slow temperature variation is the principal feature of the corona and the physical reason for the formation of the solar wind.
The absence of large Doppler displacements in the low corona emission lines is a proof that the flow velocity is small, especially if compared to the sound velocity of about 160 $\mathrm{km \cdot s^{-1}}$ (considering a temperature of $\sim 10^6$ K). Finally, the models of the solar magnetic field observed on the surface of the corona indicate a force of the mean field of a few milliTesla at the base of the corona. This field is sufficiently strong, so that the magnetic pressure in this region ($p_{\mathrm{mag}} \approx 10$ mPa) is larger than the gas pressure ($p_{\mathrm{gas}} \approx 4$ mPa). Therefore, it is expected that the magnetic effects dominate this region where the solar wind originates.
Comparing the density and temperature values in the corona and at 1 AU we can conclude that these quantities vary with the distance from the Sun. The values shown here are average values or typical values of the region; moreover, at a certain distance from the Sun, solar wind properties can vary greatly over different time scales.

1.2.2 Expansion and structure

The solar corona is an extremely complex system, but we can try to give a rough description through a simple physical model. This theory can be illustrated starting from the equations describing the conservation of mass (or continuity equation) and momentum in an ideal fluid, shown below

$$\frac{\partial \rho}{\partial t} + \nabla \cdot (\rho \mathbf{v}) = 0 \tag{1.1}$$

$$\rho \left[\frac{\partial}{\partial t} + (\mathbf{v} \cdot \nabla) \right] \mathbf{v} = -\nabla p + \frac{1}{c} \mathbf{j} \times \mathbf{B} - \frac{G M_\odot \rho}{r^2} \,. \tag{1.2}$$

For the pressure we use the ideal gas law, $p = n k_B T$, and in the hypothesis of an isothermal atmosphere (constant T) we obtain

$$p = \frac{k_B T}{m} \rho \,. \tag{1.3}$$

To simplify the solution of these equations we make some assumptions: static corona, system in spherical symmetry and negligible magnetic effects. Then, the mechanical equilibrium of the corona implies that the equation of the hydrostastic equilibrium obtained from equation (1.2) must be satisfied,

$$\frac{dp(r)}{dr} + \frac{GM_\odot}{r^2}\rho(r) = 0\,. \tag{1.4}$$

Substituting equation (1.3) in (1.4) we obtain

$$\frac{k_B T}{m} \cdot \frac{d\rho(r)}{dr} = -\frac{GM_\odot}{r^2}\rho(r) \tag{1.5}$$

from which

$$\frac{d\rho(r)}{\rho(r)} = -\frac{GM_\odot m}{k_B T} \cdot \frac{dr}{r^2}\,.$$

Assuming that the corona is isothermal, the previous equation for $\rho(r)$ can be easily integrated, obtaining that the mass density decreases with the increase of r to give

$$\ln \rho' \Big|_{\rho_0}^{\rho} = \frac{GM_\odot m}{k_B T} \cdot \frac{1}{r'} \Big|_{R_\odot}^{r}\,.$$

Then

$$\rho(r) = \rho_0 \exp\left[\frac{GM_\odot m}{k_B T}\left(\frac{1}{r} - \frac{1}{R_\odot}\right)\right]$$

and for $r \to \infty$ we have

$$\rho_\infty = \rho_0 \exp\left[-\frac{GM_\odot m}{k_B T} \cdot \frac{1}{R_\odot}\right] \simeq 10^{-5}\rho_0\,.$$

Since pressure and density are proportional, we get a similar equation for p

$$p_\infty = p_0 \exp\left[-\frac{GM_\odot m}{k_B T} \cdot \frac{1}{R_\odot}\right] \simeq 10^{-5}p_0\,.$$

But the value of ρ_∞ is too big to be realistic. Considering that at the base of the solar corona ($r = R_\odot$) we have a mass density equal to $\rho_0 \simeq 8 \times 10^{-16}$ g $\cdot$ cm^{-3}, ρ_∞ would be of the order of 10^{-20} g $\cdot$ cm^{-3} which is about 4 orders of magnitude higher than the typical density of the interstellar medium ($\simeq 10^{-24}$ g$\cdot$cm^{-3}). From these considerations, we can deduce the impossibility of the existence of an isothermal static corona.

We leave the hypothesis of isothermal corona and assume that the temperature decreases in the corona with increasing distance from the center of the Sun, which is certainly more realistic. A simple model to estimate the behavior of $T(r)$ is to suppose that the heating occurs substantially at the base of

the corona and that the outer corona is maintained at high temperatures by the transport of energy by conduction. Then, the temperature has a slowly decreasing trend with r; denoting the temperature at the base of the corona with T_0, it is obtained

$$T(r) = T_0 \left(\frac{R_\odot}{r}\right)^{\frac{2}{7}} .$$

So, using the temperature trend $T(r)$ in the relation

$$\rho(r) = \frac{m}{k_B}\frac{p(r)}{T(r)} ,$$

equation (1.4) for the pressure becomes

$$\frac{dp(r)}{dr} = -\frac{GM_\odot m}{k_B T_0}\left(\frac{r}{R_\odot}\right)^{\frac{2}{7}}\frac{p(r)}{r^2} .$$

The solution to this differential equation for $p(r)$ is

$$p(r) = p_0 \exp\left[-\frac{7}{5}\cdot\frac{GM_\odot m}{k_B T_0 R_\odot^{2/7}}\left(\frac{1}{R_\odot^{5/7}} - \frac{1}{r^{5/7}}\right)\right] ,$$

for $r \to \infty$, we have

$$p_\infty = p_0 \exp\left[-\frac{7}{5}\cdot\frac{GM_\odot m}{k_B T_0}\cdot\frac{1}{R_\odot}\right] \simeq 10^{-7} p_0 ,$$

which again is too large to be realistic. On the basis of these considerations, the hypothesis of a static corona must be abandoned and we must move towards theories that involve a dynamic balance of the corona. The theoretical problem was solved by Parker in the 1958 (Parker, 1958).

Parker's theory

To overcome the contradictions of the static corona model, a dynamic corona is introduced, continuously expanding outwards and in stationary equilibrium. For simplicity, the magnetic effects are kept negligible, as well as the hypotheses of spherical symmetry and isothermality.
Indicating with $v(r)$ the coronal gas velocity at the distance r, the continuity equation (1.1) is written in the form

$$\frac{dF_{\rm mat}}{dr} = \frac{d}{dr}\left[4\pi r^2 \rho(r) v(r)\right] = 0 ,$$

where F_{mat} is the matter's flow, constant with r. From this equation we have $r^2\rho(r)v(r) = \text{const} = \dot{M}$, where $\dot{M}$ is the loss of the star's mass equal to

$$\dot{M} = \frac{dM}{dt} = 4\pi r^2 \rho(r) v(r)\,.$$

The following momentum equation replaces the relation of hydrostatic equilibrium

$$\rho(r)v(r)\frac{dv(r)}{dr} = -\frac{dp(r)}{dr} - \frac{GM_\odot \rho(r)}{r^2}\,. \tag{1.6}$$

The two equations can be combined with the ideal gas law

$$\frac{dp(r)}{dr} = \frac{k_B T}{m} \cdot \frac{d\rho(r)}{dr}\,,$$

so the equation (1.6) becomes

$$\rho(r)v(r)\frac{dv(r)}{dr} = -v_{\text{th}}^2 \frac{d\rho(r)}{dr} - \frac{GM_\odot \rho(r)}{r^2}\,, \tag{1.7}$$

where $v_{\text{th}} = \left(\frac{k_B T}{m}\right)^{\frac{1}{2}}$ is the thermal velocity. Since $\rho(r) = \frac{\dot{M}}{4\pi r^2 v(r)}$ and considering that $\dot{M}$ is constant, we obtain

$$\frac{d\rho(r)}{dr} = \frac{\dot{M}}{4\pi}\frac{d}{dr}\left[\frac{1}{r^2 v(r)}\right] = -\rho(r)\left[\frac{2}{r} + \frac{1}{v(r)}\frac{dv(r)}{dr}\right]\,. \tag{1.8}$$

After using equation (1.8) in (1.7), through simple steps, we get the dynamic Parker equation

$$\frac{v^2(r) - v_{\text{th}}^2}{v(r)}\frac{dv(r)}{dr} = \frac{2v_{\text{th}}^2}{r} - \frac{GM_\odot}{r^2}\,. \tag{1.9}$$

At this point we indicate with $r_* = \frac{GM_\odot}{2v_{\text{th}}^2}$ the critical distance from the Sun to which a particle of the gas composing the solar corona has a gravitational energy equal to thermal energy.
The solutions of the Parker's equation can be one of the four types showed in figure 1.3. It is necessary to determine which ones are physically acceptable by imposing the following conditions

$$v(r \simeq R_\odot) \simeq 0$$

$$\rho(r \to \infty) \simeq 0\,.$$

So, from equation (1.9) we obtain the following solutions

$$\frac{v^2(r)}{v_{\text{th}}^2} - \ln\left[\frac{v^2(r)}{v_{\text{th}}^2}\right] = 4\ln\left(\frac{r}{R_\odot}\right) + 4\frac{r_*}{r} + C\,. \tag{1.10}$$

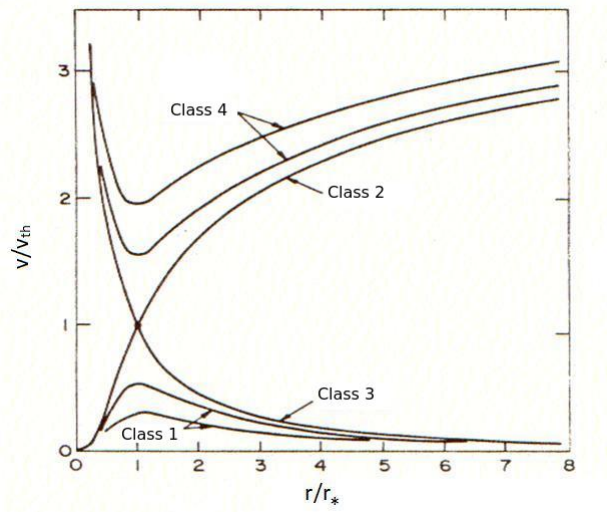

Figure 1.3: Trend of solutions of the Parker's differential equation. Image credit: `http://www.physics.usyd.edu.au/`.

The classes of solution 3 and 4 can be discarded because they do not satisfy the previous boundary conditions; while for solutions of type 1, for $r \to \infty$, $v^2(r) \ll v_{\rm th}^2$, so the equation (1.10) becomes

$$v(r) \simeq v_{\rm th} \left(\frac{R_\odot}{r}\right)^2 \sim \frac{1}{r^2}\,.$$

These solutions are characterized by a subsonic velocity and a constant density; thus they can be excluded because this class does not agree with the observations.
In the case of the solutions of class 2, if $r \to \infty$, $v^2(r) \gg v_{\rm th}^2$, we obtain

$$v(r) = \pm 2 v_{\rm th} \left[\ln\left(\frac{r}{R_\odot}\right)\right]^{\frac{1}{2}}$$

$$\rho(r) = \frac{\dot{M}}{4\pi v(r) r^2} \to 0\,.$$

This solution has a supersonic speed over a critical distance ($r_* \simeq 10\ R_\odot$), which marks the transition from a subsonic to a supersonic regime.
If we consider a temperature of $T = 10^6$ K, we get $v_{\rm th} \simeq 100$ km $\cdot$ s^{-1}, from which it is possible to calculate the speed of solar wind at a distance of 1 AU, in agreement with the observed solar wind velocity ($v_{\rm sw} \simeq 400$ km $\cdot$ s^{-1}).
Therefore, according to the isotermal corona model proposed by Parker, the solar corona is in a state of dynamic equilibrium that leads it to expand, with speeds of several hundred of kilometers per second in the interplanetary space.

1.2.3 Magnetic field

Parker's theory, despite its simplicity, provides a satisfactory description of the solar wind. However, it can not provide an accurate description of the observed solar wind properties, since the magnetic field must also be introduced in the model.
The strength and the structure of the magnetic field are determined by the differential rotation of the Sun, which produces a toroidal field, and by the turbulent motion of the plasma and charged particles of the convective region. In a plasma, at low frequency and large scale, the equations of magnetohydrodynamics are valid and in the ideal case *Alfvèn theorem* holds. It can be expressed by cnsidering, at a fixed instant, an arbitrary surface on a closed circuit and evaluating the flux of the magnetic field vector through this surface. The surface moves and change in time, since it is transported by the motion of the plasma. The flux of the magnetic field through this moving surface remains constant. Moreover, since this flux is proportional to the number of field lines that cross the surface itself, it can be thought that the lines are rigidly connected to the moving plasma, that is magnetic field lines are frozen into the plasma and have to move along with it.

The classical picture of the interplanetary magnetic field is a simple application of the frozen-in condition. Applying this concept to a model of a spherically symmetric, radially expanding solar wind, the result is an extremely simple interplanetary magnetic field. If we define a flux tube with an infinitesimal area dA_0 at the base of the corona ($r = R_\odot$), the uniform radial outflow would form a tube whose cross section, at each radius r , would be a simple map of the original dA_0, but stretched due to the spherical geometry of the expansion, as shown in figure 1.4a. Conservation of magnetic flux within the tube allows us to obtain

$$B(r) = B_0 \left(\frac{R_\odot}{r} \right)^2 , \tag{1.11}$$

where B_0 is the radial magnetic field at the base of flux tube.
It is necessary to consider that the Sun rotates around an axis that is nearly perpendicular to the ecliptic plane (plane of the Earth's orbit). The rotation speed varies with latitude in a system of heliographic coordinates where the solar rotation axis is used to define the positions in space of the solar poles. Near the solar equator, the solar corona and each plasma element of area dA_0 rotate with an angular velocity of

$$\Omega_\odot = 2.7 \times 10^{-6} \mathrm{rad} \cdot \mathrm{s}^{-1} .$$

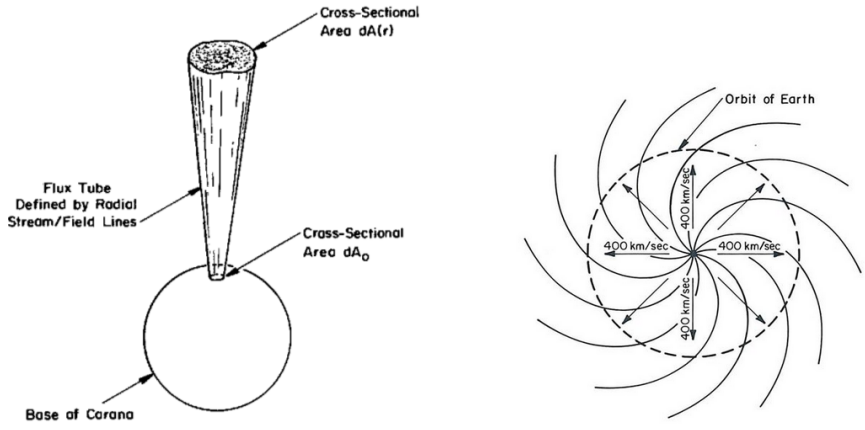

(a) **(b)**

Figure 1.4: Geometry of a flux tube defined by magnetic lines in the radial direction (a); image credit: Kivelson and Russell (1995). Schematic representation of the spiral magnetic field frozen into the solar wind (b); image credit: `https://slideplayer.com/`.

The effect of this rotation on the previous description of the flux tubes is that a plasma element, from a fixed source at the base of the corona, moves and takes the shape of a spiral. So, magnetic field lines frozen into the plasma must assume this same spiral configuration.
The shape of these field lines of force can be expressed mathematically, using a spherical polar coordinate system (r, θ, ϕ) that rotates with the Sun, as

$$r - R_\odot = -\frac{v_r}{\Omega_\odot \sin(\theta)}(\phi - \phi_0)\,,$$

known as the spiral of Archimedes. Then, we have the following relations for the components of the magnetic field

$$\begin{cases} B_r(r) = B_0 \left(\frac{R_\odot}{r}\right)^2 \\ B_\theta = 0 \\ B_\phi(r) = -B_0 \frac{R_\odot^2 \Omega_\odot \sin(\theta)}{rv} \end{cases}$$

As the heliocentric distance increases, the lines become more and more transverse, forming an angle of about 90° with the radial direction, because the radial component decreases more rapidly ($B_r \sim 1/r^2$) than the longitudinal one ($B_\phi \sim 1/r$).
Figure 1.4b shows the spiral geometry of the interplanetary magnetic field lines for a constant solar wind speed of 400 $\mathrm{km \cdot s^{-1}}$. Outside the equatorial plane the field lines wrap around themselves and, moving away from the equator,

they gradually become less enveloping and settle on a conical surface. When these lines come from the poles, they remain almost purely radial.

1.3 Interplanetary shocks

The debate on interplanetary (IP) shock waves and their nature have been of special interest to the space science community in the last few decades because they have a crucial role in space weather since they are responsible for most of the particle acceleration in the solar wind.
Quantitative theoretical models of shock propagation through the interplanetary medium were first developed by Parker (1961). Since the first direct observation of such a shock by the Mariner 2 spacecraft in 1962, many studies, both theoretical and observational, have been done for interplanetary shock waves. This investigation focused, on one side, on the detailed and local characteristics of the shock front and, on the other side, on the relation of interplanetary shocks with large scale solar wind disturbances (solar activity) with which they are connected. In fact, significant releases of plasma and magnetic field from the solar corona, the so called CMEs, can drive different kind of interplanetary shock waves from the vicinity of the Sun to large distances.
One of the most important examples of interplanetary shock wave is the bow shock, which develops in front of the Earth due to the encounter of the supersonic solar wind with the obstacle to its flow presented by the Earth's magnetic field. A bow shock is also formed in front of other planets with a magnetophere and comets where the solar wind interacts with neutral gas from the comet itself.

1.3.1 Classification of IP shocks

Shocks are transition layers across which there is a transport of particles and where the plasma change from one equilibrium state to another. They are characterized by abrupt changes in plasma properties such as flow speed, density, magnetic field strength and temperature. Due to the collisionless nature of space plasmas, these discontinuities produce a great collection of different shock types.
Shocks in the solar wind can be classified into fast shocks and slow shocks depending on whether the magnetic field strength increases or decreases at the shock, respectively. In both cases, when an interplanetary shock moves away from the Sun in the solar wind frame of reference it is called a forward shock, while in the case a shock moves towards the Sun it is called a reverse

shock. Most IP shocks in the solar wind are fast forward shocks while slow shocks are only rarely observed. Close to 1 AU nearly all fast forward shocks in the solar wind are driven by ICMEs (Interplanetary Coronal Mass Ejections). So, interplanetary shock waves can be divided into four categories based on the variation of the proton plasma temperature T, number density of the solar wind plasma N, plasma speed V and the magnitude of the magnetic field B. Another feature of interplanetary shocks is the direction of the magnetic field with respect to the shock normal (normal to the shock surface). Then, it is possible to make a classification of shocks in terms of the shock angle (θ_{Bn}) between the interplanetary magnetic field (IMF) upstream of the shock and the shock normal. Therefore, a shock is parallel when $\theta_{\mathrm{Bn}} = 0$, perpendicular when $\theta_{\mathrm{Bn}} = 90°$ and oblique when $0° < \theta_{\mathrm{Bn}} < 90°$. If the shock angle does not deviate too much from the parallel and perpendicular direction then a shock is called quasi-parallel ($\theta_{\mathrm{Bn}} < 45°$) and quasi-perpendicular shock ($\theta_{\mathrm{Bn}} > 45°$), respectively.

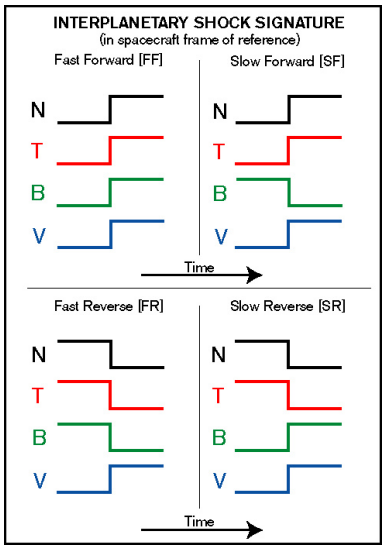

Figure 1.5: Solar wind parameters changes for the four types of interplanetary shocks. Image credit: `https://wind.nasa.gov/`.

The two kinds of shock are quite different in their structure and behavior. In the case of perpendicular shocks, the transition from upstream to downstream is stable and characterized by a steep rise in magnetic field strength known as the ramp. In addition, the magnetic field lines are parallel to the shock surface, therefore particle motions along the field do not let particles escape away from the shock. In contrast, at parallel shocks the transition from the upstream state to the downstream state occurs over a broad and turbulent region and the motion of the particles along the field lines will move them through and away from the shock.

1.4 Solar energetic particles

Solar Energetic Particles (SEPs) are high-energy particles coming from the Sun which had been first observed in the early 1940 s. They consist of protons, electrons and heavy ions with energy ranging from a few tens of keV to many GeV. They are of particular interest and importance because they can constitute a danger for spacecraft systems and human activities in space,

especially particles above 40 MeV.
SEPs can originate either from a solar flare site or from shock waves associated with Coronal Mass Ejections (CMEs), though only about 1% of the CMEs produce strong SEP events. These particles are produced by acceleration processes in the solar atmosphere associated with solar flares, and in coronal and interplanetary shocks created by the interaction of CMEs with the solar wind. In fact, a CME that is evolving may generate an IP shock which propagates in space, deforming the interplanetary magnetic field lines. Energetic particles may escape from their acceleration sites and propagate along these magnetic field lines into the interplanetary space.

SEP events are conventionally classified into two categories, impulsive and gradual, based on the duration of the event itself. The events of the first type have durations from few hours up to a day and they are often associated with flare acceleration processes. These events are related to short-duration of soft X-ray emission and are characterised by low particle fluxes, abundance of heavy elements and ^{3}He enrichment. On the contrary, gradual events have a longer duration (several days) and are accompanied by long-term soft X-ray emission. This type of events shows large intensities in particle fluxes and the composition is similar to solar wind and corona.
The intensity profiles of SEP events show a great variability from one event to another, depending on the different spatial and temporal characteristics, such as the energy of the particles, the presence of seed particle polulations, the efficiency of the shock to accelerate the particles, the transport processes and the position of the source region with respect to the spacecraft location. The high energy particles can also be produced by shock waves in the heliospheric environment, as it happens for ESP (Energetic Storm Particle) events, related to the passage of a CME-driven shock in the interplanetary space, and those associated with shocks that bound Corotating Interaction Regions (CIRs), produced by the interaction between fast and slow solar wind flows.

For SEP events, the acceleration of particles to high energies occurs in a part of the solar corona that is not yet accessible to in situ measurements and until now remote sensing is not able to establish the different mechanisms at work during an acceleration process. However, information on the source of SEP events can be obtained by studying the time evolution of the energy spectra derived from the particle flux recorded in the interplanetary space, provided that the processes of particle release and transport in the interplanetary medium do not distort their original form. In the case of impulsive SEP events, the particle spectrum should be representative of the source spectrum because they should propagate fast enough that the changes in energy can be

neglected (Dröge, 2000). Instead, during gradual SEP events the spectrum should be linked to the characteristics of the CME-driven shock and therefore it can be variable due to the propagation effects. The principal mechanism of acceleration that explains gradual SEP events is the diffusive shock acceleration (Lee, 1983), which predicts a power law energy spectrum. Often the double power law is also used to describe the observed SEP spectra (Tylka et al., 2005), although it is not yet clear the origin of the spectral breaks. Recently, Laurenza et al. (2013) found that the Weibull distribution is the best fit compared to previous models and this distribution can be associated with shock acceleration in terms of a stochastic multiplicative process (Pallocchia et al., 2017).
However, much remains to be learned about the spatial and temporal evolution of the SEP sources and about the basic SEP acceleration and transport processes.

1.5 Earth's magnetosphere

A magnetosphere is the region of space, around a planet, that is controlled by the planet's magnetic field. A planetary magnetic field constitutes an almost impenetrable obstacle to the solar wind plasma. The dynamic pressure of the solar wind presses on the magnetic field, confining it in a magnetospheric cavity that has a long tail.
The solar wind is highly supersonic before reaching the planets, so a shock is formed in front of the obstacle. Most of the solar wind particles are heated and slowed at the bow shock and detour around the Earth in the magnetosheath. The outer boundary of Earth's confined geomagnetic field is called the magnetopause. The interaction of the solar wind with the magnetosphere is a complex process.

1.5.1 Magnetosphere's characteristics

The Earth's magnetosphere is a highly dynamic structure that responds dramatically to changes in the dynamic pressure of the solar wind and the orientation of the interplanetary magnetic field. Solar wind exerts an outward force on every obstacle it encounters, such as the Earth's magnetic field, since both the magnetic field of the Earth and that of the solar wind are frozen in their plasmas. Thus, the solar wind exerts a pressure on the magnetoshere. In a stationary situation, the solar wind force against the magnetosphere and the magnetosphere force against the solar wind are in equilibrium.

The interaction with the solar wind deforms the dipolar magnetic field of the Earth, compressing the field lines on the dayside and stretching them out to form a long tail (the magnetotail) on the nightside. If there are no viscosity, that is, if there are no tangential stress or drag on the boundary, but only forces along the normal to the surface, one would expect the shape of a drop, considering that the magnetic field behind the Earth weakens with distance. The exact form, even in this approximation, is difficult to determine due to the non-linear nature of the postshock region. However, it is necessary to consider the tangential stress which transfers the momentum to the magnetospheric plasma and causes it to flow towards the tail. This stress can be transferred by various processes that operate to transfer magnetic plasma from the dayside to the nightside magnetosphere and so have the potential to alter the shape of the magnetosphere. Reconnection is one of these processes, in which the interplanetary magnetic field lines connect with the planetary ones when the interplanetary and planetary fields are in opposite directions. In the Earth's magnetoshere, reconnection takes place in the magnetopause and in the magnetotail, two regions characterized by relatively thin sheets of electric current separate zones with different magnetic fields.
A current sheet can be defined as a thin surface through which the strength of the magnetic field and/or the direction can change substantially.

Magnetopause

The magnetopause is the name given to the outer boundary that contains within it the magnetosphere; it separates the geomagnetic field and plasma of terrestrial origin from the solar wind plasma. The existence of the magnetopause was proposed for the first time by Chapman and Ferraro (1931), although in terms of an intermittent corpuscular stream from the Sun that was present only during periods of solar activity; however, subsequent studies have shown that the magnetopause is a permanent feature (Dungey, 1954).

The position of the magnetopause can be calculated by requiring the total pressure on the two sides of the boundary to be equal. To a good approximation, the pressure in the magnetosphere, which is mainly magnetic pressure, must correspond to the pressure in the magnetosheath[1], given by the combination of the thermal pressure and the magnetic pressure. The pressure terms

[1]Region of space between the magnetopause and the bow shock. This area of space contains the solar wind plasma that has been heated by the shock wave that the solar wind forms when it meets the magnetosphere.

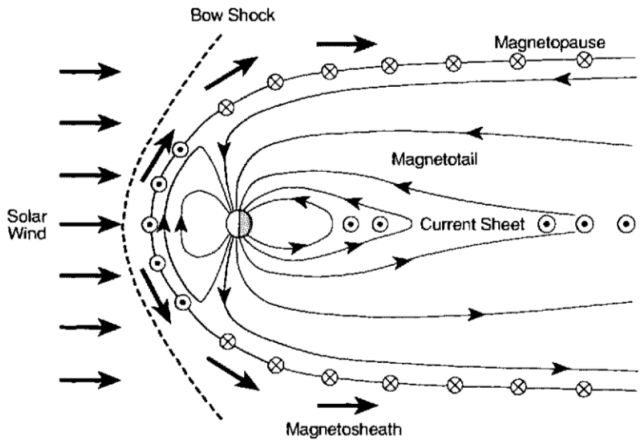

Figure 1.6: Section of the magnetosphere in which the geomagnetic field is perfectly confined by the current sheets flowing on the magnetopause. A second current sheet flows through the midplane of the magnetotail and connects with the magnetopause currents of the flanks of the tail. The solar wind flux is deflected at the bow shock and flows around the magnetosphere, forming the magnetosheath. Image credit: `http://www.physics.usyd.edu.au/`.

in the solar wind and on the nose of the magnetosphere are roughly balanced

$$(\rho v^2)_{sw} \sim \left(\frac{B^2}{2\mu_0}\right)_E . \tag{1.12}$$

The intensity of the magnetic field immediately inside the equatorial dayside magnetopause is greater than twice that of the dipole field at the same position. This happens because the magnetopause current cancels the dipole field outside the magnetopause, and so it must create an equal field, but in the opposite direction, just inside the magnetopause, which is added to the dipole field, doubling it. When a sudden increase in the dynamic pressure of the solar wind, as often follows the passage of an interplanetary shock, reaches the Earth, the magnetosphere is compressed; the magnetopause moves closer to the Earth, and at the same time the magnetopause current intensifies. The movement and intensification of the current are detected on the Earth's surface as a sudden increase in the intensity of the geomagnetic field of a few tens of nanoTesla.

Magnetotail

The geomagnetic tail is the region of the Earth's magnetosphere that stretches away from the Sun behind the Earth. It is a region of great importance for the magnetosphere, because it acts as a reservoir of plasma and

energy, which are released into the inner magnetosphere aperiodically. A current sheet lies in the center of the tail, embedded within a region of hot plasma, the plasma sheet, which separates two zones called tail lobes. These two lobes connect magnetically to the two polar regions of the Earth and are identified as the north and south lobes. The magnetic field in the north (south) lobe is directed towards (away from) the Earth; hence the need for a current sheet to separate these two regions with a magnetic fields in opposite direction.

In a static tail, there must be satisfied pressure balance between the tail lobe and both the plasma sheet and the solar wind. This can be used to estimate the properties of the plasma sheet and the geometry of the distant tail.

Chapter 2

Magnetohydrodynamic turbulence

This chapter presents some of the most important general properties of the magnetohydrodynamic turbulence.
Turbulence is an ubiquitous phenomenon, which each of us can observe directly. The arabesques formed by the smoke of a cigarette or by the coffee poured into a glass of milk, the whirling motion of a river or the motion of the meteorological perturbations observed by satellite are examples of turbulence. Scientifically, the term *turbulence* is used to indicate the motion of an irregular and apparently random fluid both in space and time. The simplest way to illustrate this phenomenon is to consider a cylinder around which a fluid flows. When the fluid velocity is relatively low, it flows around the cylinder in a regural way. As speed increases, a series of vortices is generated in the fluid and the motion becomes irregular and chaotic.

The presence of these turbulent structures was recognized long time ago by Leonardo da Vinci. By studying the movement of water in the rivers, he was the first to use the term turbulence to describe the swirling motion of a fluid.
Turbulence became an experimental science at the end of 19th century, thanks to the research of Reynolds, who made a systematic study of the transition from the laminar regime to the turbulent regime in a fluid. He noticed that the behavior of the fluid can be classified through the value of a parameter, now called *Reynolds number*, given by the combination of the viscosity coefficient of the fluid μ, the mass density ρ, a characteristic velocity U and a characteristic length L

$$Re = \frac{UL\rho}{\mu} .$$

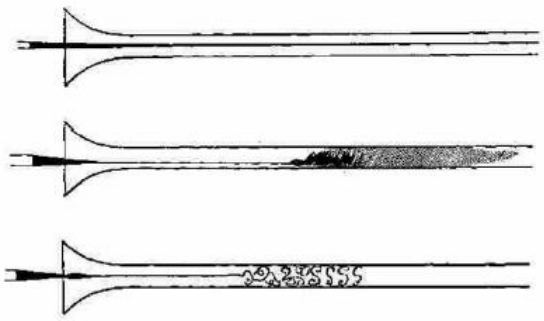

Figure 2.1: Original pictures by Reynolds showing the transition from a laminar to a turbulent state from top to bottom (Reynolds, 1883). Image credit: `https://en.wikipedia.org/`.

When $Re \lesssim 1$, the flow is regular and the motion is laminar. As the Reynolds number increases, the transition from a laminar to a turbulent state occurs. The value of Re for which this transition occurs depends on the configuration considered. In the limit $Re \to \infty$ the turbulence is said to be in a *fully developed state*.

From a stationary and laminar flow, we pass, through successive stages, to a turbulent current, characterized by vortical structures in 3D, by an high level of non-stationarity and a highly unstable nature.

When a fluid is electrically conductive, the turbulent motions are accompanied by fluctuations in the magnetic field. The discipline that studies the dynamics of these fluids is *magnetohydrodynamics*, indicated briefly with the acronym MHD. Conductive fluids are rare in the terrestrial world, where electrical conductors are generally solid. The most common conductive fluids are ionized gases, called *plasmas*, abundant in the extraterrestrial world. In fact, about 99% of all the material in the universe exists in the plasma state. Natural plasmas, as well as laboratory plasmas, are often in a turbulent state, where dynamics become chaotic and unpredictable. At the scales where the plasma can be described by the equations of magnetohydrodynamics, we have *magnetohydrodynamic turbulence*.
Magnetohydrodynamic turbulence plays a fundamental role in the dynamics of astrophysical plasmas in very different environments and on a very wide range of scales, from kilometer to kiloparsec [1] and beyond.

The dynamics of turbulence can not be studied by solving the fluid or

[1]The parsec (pc) is a unit of length used to measure large distances to astronomical objects outside the solar system. It is defined as the distance from the Earth (or the Sun) of a star that has an annual parallax of 1 arcsecond; therefore, 1 pc corresponds to $\approx 3.08567758 \times 10^{16}$ m.

MHD equations analytically, but rather through numerical simulations. For this reason it is good to know the physical and elementary mechanisms that contribute to determine the complexity of the fluid.

2.1 MHD equations

The physical evolution of a conductive fluid can be described by a system of partial differential equations, the equations of magnetohydrodynamics, which can be obtained directly from hydrodynamics and taking into account Maxwell's equations to define the magnetic field and the currents. For the description of the fluid both scalar and vector fields are used.

The first equation to consider in MHD is the continuity equation that expresses the conservation of mass

$$\frac{\partial \rho}{\partial t} + \nabla \cdot (\rho \mathbf{u}) = 0 \,. \tag{2.1}$$

Instead, the momentum equation can be obtained by considering the forces that act on a fluid element δV with mass equal to $\rho \delta V$, where ρ is the mass density.

- *The Lorentz force.* In an electromagnetic field, a particle of charge q_i is subjected to the Lorentz force $q_j(\mathbf{E} + \mathbf{u}_j \times \mathbf{B}/c)$. The force on a macroscopic fluid element is equal to the sum of the forces acting on the individual particles $\delta q \mathbf{E} + \delta \mathbf{j} \times \mathbf{B}/c$, where δq is the net charge and $\delta \mathbf{j}$ the electric current carried by the fluid element. Since in most of the fluids both charge signs are present, which lead to a situation of global neutrality $\delta q \simeq 0$ (called quasi-neutrality and does not imply the disappearance of the electrostatic field), only the magnetic part contributes to the Lorentz force,
$$\frac{1}{c}\mathbf{j} \times \mathbf{B} \,, \tag{2.2}$$
where $\mathbf{j}$ is the current density.

- *The pressure force.* If we assumed that, under conditions of local thermodynamic equilibrium, the pressure tensor is isotropic, the force exerted is
$$-\nabla p \,. \tag{2.3}$$

- *Gravitational force*[2]. The force results

$$\rho \mathbf{g}\,, \tag{2.4}$$

  where $\mathbf{g} = -\nabla\phi_g$.

- *The viscous force.* If the viscosity coefficient is indicated with μ, this force takes the form of

$$\mu\left[\nabla^2\mathbf{u} + \frac{1}{3}\nabla(\nabla\cdot\mathbf{u})\right]. \tag{2.5}$$

Combining the contributions of these forces we obtain the momentum equation or equation of motion

$$\rho\left[\frac{\partial\mathbf{u}}{\partial t} + (\mathbf{u}\cdot\nabla)\mathbf{u}\right] = -\nabla p + \frac{1}{c}\mathbf{j}\times\mathbf{B} + \rho\mathbf{g} + \mu\left[\nabla^2\mathbf{u} + \frac{1}{3}\nabla(\nabla\cdot\mathbf{u})\right]. \tag{2.6}$$

Since the current density $\mathbf{j}$ is related to the magnetic field by Ampère's law,

$$\nabla\times\mathbf{B} = \frac{4\pi}{c}\mathbf{j}\,,$$

substituting $\mathbf{j}$ in the (2.2), the Lorentz force can be written as follows

$$\frac{1}{c}\mathbf{j}\times\mathbf{B} = -\frac{1}{8\pi}\nabla B^2 + \frac{1}{4\pi}\mathbf{B}\cdot\nabla\mathbf{B}\,. \tag{2.7}$$

The first term in the right-hand member acts as a pressure force, so it can be added to the (2.3) to get the total pressure

$$P = p + \frac{B^2}{8\pi} \tag{2.8}$$

and the ratio between the two pressures,

$$\beta = \frac{8\pi p}{B^2}\,,$$

is an important parameter characterizing the strength of the magnetic field in a plasma.

The dynamics of the magnetic field follows from Faraday's law

$$\frac{\partial\mathbf{B}}{\partial t} = -c\nabla\times\mathbf{E}\,,$$

where the electric field $\mathbf{E}$ is determined by the generalized Ohm's law (obtained

[2]In a magnetized plasma gravity is often negligible compared with the Lorentz force.

by considering a fluid in motion)

$$\mathbf{E} + \frac{1}{c}\mathbf{u} \times \mathbf{B} = \frac{1}{\sigma}\mathbf{j}\,,$$

where σ is the electrical conductivity of the fluid.
Substituting $\mathbf{E}$ into Faraday's equation and assuming uniform conductivity, we obtain the advection-diffusion equation that describes the evolution of magnetic field over time

$$\frac{\partial \mathbf{B}}{\partial t} = \nabla \times (\mathbf{u} \times \mathbf{B}) + \eta \nabla^2 \mathbf{B}\,, \tag{2.9}$$

where $\eta = c^2/(4\pi\sigma)$ is the magnetic diffusivity.

Finally, it remains to find the dynamic equation for the pressure. Under conditions of local thermodynamic equilibrium the pressure p is coupled to the density ρ and temperature T by the equation of state. Therefore, we may assume the validity of the ideal gas law and in the case of plasma the equation is written in the form

$$p = 2nk_B T\,,$$

where $n = n_i = n_e$ is the particle number density and k_B is the Boltzmann constant. Since heat conduction is a diffusive process, at sufficiently large scales it can be neglected, so that the change of state in a fluid element is adiabatic,

$$\frac{d(p\rho^{-\gamma})}{dt} = 0\,,$$

which is equivalent to a constant entropy transformation, where the entropy of an ideal gas is $s = c_v \ln(p\rho^{-\gamma})$. As a result we get

$$\frac{\partial p}{\partial t} + \mathbf{u} \cdot \nabla p + \gamma p \nabla \cdot \mathbf{u} = 0\,, \tag{2.10}$$

where the parameter $\gamma = c_p/c_v$ is the adiabatic exponent, given by the ratio of the specific heats at constant pressure and volume.
However, if the heat conduction is not negligible, an equation for energy conservation is needed

$$\rho T \left[\frac{\partial s}{\partial t} + (\mathbf{u} \cdot \nabla)s\right] = \nabla \cdot (\chi \nabla T) + \frac{\mu}{2}\left(\frac{\partial u_i}{\partial x_k} + \frac{\partial u_k}{\partial x_i} - \frac{2}{3}\delta_{ik}\nabla \cdot \mathbf{u}\right)^2\,, \tag{2.11}$$

where χ is the heat diffusivity.

The above equations can be greatly simplified if we consider the hypothesis of incompressible fluid: $\rho = \text{cost}$. Starting from the equation of motion (3.1),

neglecting the terms of gravity and magnetic field, we obtain the *Navier-Stokes equation*[3] (NS)

$$\frac{\partial \mathbf{u}}{\partial t} + (\mathbf{u}\cdot\nabla)\mathbf{u} = -\left(\frac{\nabla p}{\rho}\right) + \nu\nabla^2\mathbf{u}\,, \tag{2.12}$$

where the coefficient $\nu = \mu/\rho$ is the kinematic viscosity. The incompressibility of the flow translates into a condition on the velocity field, $\nabla\cdot\mathbf{u} = 0$. This condition eliminates all high frequency sound waves and is called the incompressible limit.

Using the velocity scale U and the length scale L, we define the dimensionless independent variables $\mathbf{r} = \mathbf{r}'L$ (hence $\nabla = \nabla'/L$), $t = t'(L/U)$, $\mathbf{u} = \mathbf{u}'U$ and $p = p'U^2\rho$, using them in the equation (2.12), we obtain

$$\frac{\partial \mathbf{u}'}{\partial t'} + (\mathbf{u}'\cdot\nabla')\mathbf{u}' = -\nabla' p' + Re^{-1}\nabla'^2\mathbf{u}'\,. \tag{2.13}$$

The Reynolds number $Re = UL/\nu$ is clearly the only parameter that controls the flow of the fluid and represents a measure of the relative strength between the non-linear convective term $(\mathbf{u}\cdot\nabla)\mathbf{u}$ and the viscous term $\nu\nabla^2\mathbf{u}$ that appear in the equation (2.12). For high values of the Reynolds number, the non-linear term dominates, and this indicates that in the dynamics of the fluid flow, turbulence is a non-linear phenomenon.
A particular simplified form of the Navier-Stokes equation is the *Euler equation* and is obtained in the ideal limit in which the flow has negligible viscosity or $\nu = 0$.

In the incompressible case MHD equations can be reduced to

$$\frac{\partial \mathbf{u}}{\partial t} + (\mathbf{u}\cdot\nabla)\mathbf{u} = -\nabla P_{tot} + \nu\nabla^2\mathbf{u} + (\mathbf{b}\cdot\nabla)\mathbf{b} \tag{2.14}$$

and

$$\frac{\partial \mathbf{b}}{\partial t} + (\mathbf{u}\cdot\nabla)\mathbf{b} = -(\mathbf{b}\cdot\nabla)\mathbf{u} + \eta\nabla^2\mathbf{b}\,, \tag{2.15}$$

where we introduced $P_{tot} = P/\rho$ and the variable $\mathbf{b} = \mathbf{B}/\sqrt{4\pi\rho}$, which represents the normalized magnetic field so to have the dimensions of a velocity.

Like the the usual Reynolds number, we can define a *Lundquist number*

$$S = \frac{\mathbf{c}_A L_0}{\eta}\,,$$

with $\mathbf{c}_A = \mathbf{B}_0/\sqrt{4\pi\rho}$ the Alfvén velocity related to the large-scale L_0 magnetic field $\mathbf{B}_0$.

[3]The equation to describe the flow of an incompressible real fluid was first introduced by Claude-Louis Navier in 1823 and later improved by George Gabriel Stokes.

In absence of dissipative terms, the incompressible MHD theory presents three conservation equations. There are two classes of invariants, one that involves fluid variables and one that involves the magnetic field.
The first invariant of interest describes the conservation of the *total energy*, given by the sum of kinetic and magnetic energy

$$E = \int_V (u^2 + b^2)\, d^3\mathbf{r}\,. \tag{2.16}$$

Another important conserved quantity in MHD theory is the *cross-helicity*, which represents a measure of the degree of correlations between velocity and magnetic fields

$$H^C = \int_V \mathbf{u}\cdot\mathbf{b}\, d^3\mathbf{r}\,. \tag{2.17}$$

While E and H^C involve both fluid and magnetic contributions, the last invariant, the *magnetic helicity*, contains only magnetic terms. Considering that the magnetic field is frozen in the plasma, its structures can become very complicated and this invariant offers a measure of this complexity, in particular the degree of connection between the magnetic flux tubes

$$H^M = \int_V \mathbf{a}\cdot\mathbf{b}\, d^3\mathbf{r}\,, \tag{2.18}$$

where $\mathbf{b} = \nabla\cdot\mathbf{a}$, with $\mathbf{a}$ the vector potential.

In the case of an incompressible fluid it is of particular interest to write the MHD equations in terms of the so-called Elsässer variables

$$\mathbf{Z}^{\pm} = \mathbf{u} \pm \mathbf{b}\,,$$

to obtain a more symmetrical form of the equations MHD (2.14) and (2.15)

$$\frac{\partial \mathbf{Z}^{\pm}}{\partial t} + (\mathbf{Z}^{\mp}\cdot\nabla)\mathbf{Z}^{\pm} = -\nabla P_{tot} + \frac{1}{2}(\nu+\eta)\nabla^2\mathbf{Z}^{\pm} + \frac{1}{2}(\nu-\eta)\nabla^2\mathbf{Z}^{\mp} + \mathbf{F}^{\pm}\,. \tag{2.19}$$

To complete the set of equations the relations

$$\nabla\cdot\mathbf{Z}^{\pm} = 0$$

are added to the (2.19).
In the plasma reference system, the Elsässer variables take the form

$$\mathbf{z}^{\pm} = \mathbf{u} \pm \mathbf{b}'\,,$$

where $\mathbf{b}' = \mathbf{b} + \mathbf{c}_A$. It follows that the equation (2.19) can be written in the

form

$$\frac{\partial \mathbf{z}^{\pm}}{\partial t} \mp (\mathbf{c}_A \cdot \nabla)\mathbf{z}^{\pm} + (\mathbf{z}^{\mp} \cdot \nabla)\mathbf{z}^{\pm} = -\nabla P_{tot} + \nu^{\pm}\nabla^2 \mathbf{z}^{\pm} + \nu^{\mp}\nabla^2 \mathbf{z}^{\mp} + \mathbf{F}^{\pm}\,, \quad (2.20)$$

where $2\nu^{\pm} = \nu \pm \eta$ are the dissipative coefficients, obtained from the combination of the kinematic viscosity coefficient and magnetic diffusivity, and $\mathbf{F}^{\pm}$ are eventual external forcing terms.
On linearizing the equation (2.20) and neglecting the viscous and the external forcing terms, we have

$$\frac{\partial \mathbf{z}^{\pm}}{\partial t} \mp (\mathbf{c}_A \cdot \nabla)\mathbf{z}^{\pm} \simeq 0\,. \quad (2.21)$$

The equations (2.21) have solutions of the type $\mathbf{z}^{-}(\mathbf{x} - \mathbf{c}_A t)$ and $\mathbf{z}^{+}(\mathbf{x} + \mathbf{c}_A t)$ that describe respectively the Alfvénic fluctuations propagating in the direction of the magnetic field $\mathbf{B}_0$ and those that propagate in the opposite direction to $\mathbf{B}_0$. Note that MHD equations (2.19) have the same structure as the Navier-Stokes equation; the main difference derives from the fact that nonlinear coupling occurs only between fluctuations propagating in the opposite direction and this influences the description of turbulence.

Since the Elsässer variables are very important in the incompressible MHD theory, ideal invariants can be expressed using this formalism. The energy E and the cross-helicity H^C become respectively

$$E = \frac{1}{4}\int_V \left[(\mathbf{z}^{+})^2 + (\mathbf{z}^{-})^2\right] d^3\mathbf{r}\,, \quad (2.22)$$

$$H^C = \frac{1}{4}\int_V \left[(\mathbf{z}^{+})^2 - (\mathbf{z}^{-})^2\right] d^3\mathbf{r}\,, \quad (2.23)$$

while it is not convenient to express the magnetic helicity H^M in terms of the Elsässer variables. Therefore, we introduce a quantity which, although is not an invariant, plays an important role in MHD turbulence, that is the difference between kinetic energy and magnetic energy, called residual energy, which can be written in the following form

$$E^R = \frac{1}{2}\int_V (u^2 - b^2)\, d^3\mathbf{r} = \frac{1}{2}\int_V (\mathbf{z}^{+} \cdot \mathbf{z}^{-})\, d^3\mathbf{r}\,. \quad (2.24)$$

It is worth to remark that in classical hydrodynamics, dissipative processes are defined through the viscosity and the heat diffusivity. In the magnetohydrodynamic case the number of coefficients increases considerably and, apart from some additional electric coefficients, there is a large-scale magnetic field $\mathbf{B}_0$. This makes the MHD equations intrinsically anisotropic.

2.2 Turbulence phenomenology

The problem of developed turbulence, which occurs at high Reynolds numbers, is of great importance in meteorology, aeronautical engineering, etc., and plays a central role also in theoretical physics, in connection with the study of the phenomena that present scaling invariance.

Due to the high number of degrees of freedom involved and the strong dependence on initial conditions typical of chaotic systems, it is necessary to give up a detailed description of the velocity field (determined by the initial conditions and the boundary conditions) to describe the systems under a developed turbulence regime; in fact, it is impossible to predict the evolution of the system despite the laws of dynamics are deterministic. We can attempt to construct a statistical theory of turbulent states: the velocity field becomes a stochastic variable and probabilistic forecasts can be obtained, which become exact by making temporal averages over long intervals. This marks the passage from a deterministic description to a statistical description of turbulence. A statistical theory of turbulence can only be proposed if we assume that, at high Reynolds numbers, the statistical properties are universal, that is, independent of the mechanism that produces turbulence and of the way in which kinetic energy of the fluid is dissipated.

The theoretically simplest case is that of an incompressible fluid (already assumed in the previous paragraph), homogeneous and isotropic; the homogeneity regards the composition of the fluid, which must not have spatial variations while the isotropy is a more general characteristic and concerns the properties of deformation, elasticity, propagation, etc., which must be the same in each direction.
On a global scale turbulence is generally not homogeneous, however, far from strongly non-homogeneous boundary layers, the variations of the average quantities are usually rather weak, so that a limited region of space can be considered homogeneous. The isotropy assumption is made because the fluid quickly forgets the way, often anisotropic, in which turbulence is generated. The experimental results on hydrodynamic turbulence show that isotropy is usually (but not always) satisfied, even if the addition of a background magnetic field in a plasma has a decisive influence on the dynamics of turbulence; consequently the conditions for isotropy are rarely satisfied.

In fully developed turbulence the dissipation rate of energy is finite, even for very small values of the coefficients ν and η, such that the conditions are different from the ideal case, in which ν vanishes completely, that is the limit $\nu \to 0$ differs from the behavior for $\nu = 0$. However, important information

about non-linear transfer processes can be obtained by considering the statistical equilibrium properties of the ideal system, which is characterized by some integral quantities, namely the ideal invariants.
In order to apply the formalism of statistical mechanics to continuum fluid turbulence, it is convenient to introduce a discretization in the Fourier space by limiting the number of modes included. In the theory of homogeneous turbulence we truncate the Fourier series.

In general, the ideal invariants of the continuum system are not strictly conserved in the truncated system. Quadratic invariants, however, and presumably only these, are sufficiently "robust" to survive truncation. This property is based on the validity of a conservation relation for a set of wave vectors $\mathbf{k}$, $\mathbf{p}$, $\mathbf{q}$ forming a triangle, satisfying $\mathbf{k}+\mathbf{p}+\mathbf{q}=0$. In the presence of only three modes, the conservation relation is

$$\dot{E}_k + \dot{E}_p + \dot{E}_q = T(\mathbf{k},\mathbf{p},\mathbf{q}) + T(\mathbf{p},\mathbf{q},\mathbf{k}) + T(\mathbf{q},\mathbf{k},\mathbf{p}) = 0\,, \tag{2.25}$$

where T is called the non-linear transfer function, which follows from the dynamic equation. The validity of this relation, and of the similar ones for the cross-helicity H_k^C and for the magnetic helicity H_k^M, can be verified by direct calculations starting from the MHD equations written in the Fourier space. In the incompressible case they can be written as

$$\dot{\mathbf{u}}_k = -i\left(\mathbf{I} - \frac{\mathbf{kk}}{k^2}\right)\cdot\sum_p \left[\mathbf{u}_p(\mathbf{k}\cdot\mathbf{u}_{k-p}) - \mathbf{b}_p(\mathbf{k}\cdot\mathbf{b}_{k-p})\right]\,, \tag{2.26}$$

$$\dot{\mathbf{b}}_k = -i\left(\mathbf{I} - \frac{\mathbf{kk}}{k^2}\right)\cdot\sum_p \left[\mathbf{b}_p(\mathbf{k}\cdot\mathbf{u}_{k-p}) - \mathbf{u}_p(\mathbf{k}\cdot\mathbf{b}_{k-p})\right]\,. \tag{2.27}$$

Multiplying the (2.26) for $\mathbf{u}_k$ and the (2.27) for $\mathbf{b}_{-k}$ and adding the results, we obtain the explicit form of the energy-transfer function, from which the equilibrium relation (2.25) is derived, assuming that there are only three modes.

If we suppose to have an ensemble of ideal, truncated and equivalent turbulent systems, the statistical theory shows that the distribution of probabilities at equilibrium (absolute equilibrium) in phase space is given by the Gibbs' functional

$$\rho_G = Z^{-1}\exp(-W)\,, \qquad W = \alpha E + \beta H^M + \gamma H^C\,,$$

where α, β and γ are the Lagrange multipliers that are determined from the invariants, Z is a normalization factor and E, H^C and H^M, defined respectively in the relations (2.16), (2.17) and (2.18), respectively, can be rewritten

as follows using the variables in the phase space

$$E = \frac{1}{2}\sum_k (\mathbf{u}_k \cdot \mathbf{u}_{-k} + \mathbf{b}_k \cdot \mathbf{b}_{-k})\,,$$

$$H^C = \sum_k \mathbf{u}_k \cdot \mathbf{b}_k\,,$$

$$H^M = \sum_k i(\mathbf{k} \times \mathbf{b}_k) \cdot \mathbf{b}_{-k}/k^2\,.$$

After some algebraic passages, we obtain the following ideal spectral densities

$$E_k^K = \frac{4\pi k^2}{\alpha}\left(1 + \frac{k^2 \tan^2\phi}{k^2 - k_0^2}\right)\,,$$

$$E_k^M = \frac{4\pi k^2}{\alpha} \cdot \frac{k^2 \sec^2\phi}{k^2 - k_0^2}\,.$$

Then

$$E_k = \frac{4\pi k^2}{\alpha}\left[1 + \frac{k^2(\tan^2\phi + \sec^2\phi)}{k^2 - k_0^2}\right]\,,$$

$$H_k^C = -\frac{8\pi k^2\gamma}{\alpha^2\cos^2\phi} \cdot \frac{k^2}{k^2 - k_0^2} = -\frac{2\gamma}{\alpha}E_k^M\,,$$

$$H_k^M = -\frac{8\pi k^2}{\alpha\cos^2\phi} \cdot \frac{k_0}{k^2 - k_0^2} = -\frac{2k_0}{k^2}E_k^M\,,$$

with $\sin\phi = \gamma/(2\alpha)$, $k_0 = \beta/(\alpha\cos^2\phi)$ and $E = \int_{k_{\min}}^{k_{\max}} E_k\,dk$ and similarly for H^C and H^M. The values of the multipliers α, β and γ are limited by the condition that ρ_G must be integrable, which means that W must be defined positive; in particular, E_k^K and E_k^M must be positive for any k belonging to the interval $k_{\min} \le k \le k_{\max}$, from which the conditions follow

$$\alpha > 0\,, \qquad |\gamma| < 2\alpha\,, \qquad k_0^2 < k_{\min}^2\,.$$

The ratio β/α is a measure of the magnetic helicity, whereas γ/α is a measure of cross-helicity. It should be noted that the residual energy spectrum, the difference of kinetic and magnetic energies, is always negative

$$E_k^R = E_k^K - E_k^M = -\frac{4\pi k^2}{\alpha} \cdot \frac{k_0^2}{k^2 - k_0^2}\,.$$

Thus the ideal energy spectrum is dominated by the magnetic contribution, especially at high wavelengths.

2.2.1 Energy cascade

In the approximation of homogeneous and isotropic turbulence, it is worth to mention the great contribution given by Richardson (1922) and Kolmogorov (1941). Their works constitute an important description of the phenomenon of turbulence. The first has the merit of having introduced the concepts that underlie the theory of *energy cascade*. According to Richardson, turbulence is made by a collection of eddies at all scales.
The energy is injected at a length scale L and it is transferred, without dissipation, by non-linear processes to small scales until it reaches a characteristic scale l_{d}, where dissipation takes place. The principal idea is that at very high Reynolds numbers, the injection scale L and the dissipative scale l_{d} are completely separated. In a stationary situation, the rate of energy injection must be balanced by the energy dissipation rate and must also be equal to the energy transfer rate measured at any scale l in the inertial range $l_{\mathrm{d}} \ll l \ll L$. In the case of large Reynolds numbers, the fluid system is unable to dissipate all the energy input at the scale L. Therefore, the excess energy must be dissipated at smaller scales where the dissipation process is much more efficient. This is the physical origin for the energy cascade.
Richardson assumed that large-scale turbulent structures are unstable and tend to break up by transferring their kinetic energy to smaller eddies, which in turn propagate the same phenomenon to even smaller scales. This cascade phenomenon repeats itself until the Reynolds number, relative to these structures, is sufficiently small, so the viscous terms determine the dissipation.

The transfer process described above can be represented by a transfer process of a quantity that is conserved. In fact, in the non-linear interactions, the spectral densities of ideal invariants are conserved, as shown in the conservation relations such as (2.25). If the interactions are local, that is dominated by wavenumbers $\mathbf{k}$, $\mathbf{p}$, $\mathbf{q}$ of similar magnitude, the transfer in the k-space occurs in relatively small steps, such that many steps are needed from the injection range to the dissipation range.

In turbulence two types of cascade can occur:

direct cascade which describes the spectral transfer from k_{in} to larger wavenumbers; it is also called normal, since this is the well known transfer in ordinary hydrodynamic turbulence (the Richardson's cascade);

inverse cascade where the transfer proceeds from k_{in} to smaller wavenumbers.

The directions of the cascade can be determined by the structure of the ideal

invariants of the system. Although the states of absolute equilibrium are far from the dissipative turbulence, they indicate the direction of the spectral evolution in a real system, since the non-linear dynamics is identical. A direct cascade is expected for the spectral density of some ideal invariant if the ideal spectrum has a peak at high k since, when it is injected in some intermediate spectral range, the quantity relaxes towards larger wavenumbers. In the opposite case of an ideal spectrum peaked at low k, the quantity should have an inverse cascade. By controlling the ideal spectra for the MHD invariants E_k, H_k^C and H_k^M, it is found that E_k and H_k^C should have direct cascades, while H_k^M should have an inverse cascade. The existence of an inverse cascade of the magnetic helicity was first discussed by Frisch et al. (1975). A condition to have an inverse cascade seems to be that, in the presence of dissipation, the decay of turbulence is selective, that is one of the ideal invariants decays much slower than the other.

2.3 Energy spectra

The hypothesis of an energy cascade, discussed in the previous paragraph, allows us to try understanding the fundamental mechanisms that occur in a turbulent flow and it is compatible with the invariance with respect to scale transformations that appears in the Navier-Stokes equations when the Reynolds number goes to infinity.

Introducing a length scale l, it is easy to verify that the scaling transformations $l \to \lambda l'$ and $\mathbf{u} \to \lambda^h \mathbf{u}'$ (where λ is a scaling factor and h is a scaling index) leave invariant the non-viscous Navier-Stokes equation for any scaling exponent h, as long as $p \to \lambda^{2h} p'$.
When the dissipative term is taken into account, there is a characteristic length scale, i.e. l_d. As already mentioned above, from a phenomenological point of view, this is the length scale where the dissipative effects begin to take place. Of course, since ν is generally very low, l_d is expected to be very small. In fact, there exists a simple relationship for the scaling of l_d and the Reynolds number Re, which is $l_\mathrm{d} \sim LRe^{-3/4}$.

Ideal MHD equations, as is easy to verify, show similar scaling characteristics; in fact, the following scaling transformations $\mathbf{u} \to \lambda^h \mathbf{u}'$ and $\mathbf{B} \to \lambda^\beta \mathbf{B}'$ (where β is a new scaling index different from h) leave the inviscid MHD equations unchanged, providing $p \to \lambda^{2\beta} p'$, $T \to \lambda^{2h} T'$ and $\rho \to \lambda^{2(\beta-h)} \rho'$. This means that velocity and magnetic variables have different scalings, in other words $h \neq \beta$, only when the density scaling is taken into account. In the incompressible case, however, we cannot distinguish between scaling laws for

velocity and magnetic variables.

Furthermore, it is expected that the statistical properties of turbulence at small length scales follow universal scaling laws, independent of boundary conditions.

2.3.1 Kolmogorov theory

Richardson's study of turbulence, and in particular the intuition about the mechanism which is at the base of the energy cascade phenomenon, has been taken up and continued by Kolmogorov, who has contributed most to this model.

The first formal theory of turbulence was obtained by a statistical approach from Kolmogorov in 1941. Through hypotheses on the statistical and physical nature of velocity fields, the 1941 Kolmogorov theory (K41) is able to describe the trend of the energy spectrum of the velocity field. He proposed a developed turbulence approach based on a global scale invariance hypothesis, where it is assumed that, in the cascade process, the energy transfer rate does not depend on the length scale l, in the range $[l_{\mathrm{d}}, L]$ (called *inertial range*, since it is dominated by the inertial forces), and that the energy dissipation rate is uniform in space.

According to this work it is possible to recognize, within homogeneous and isotropic turbulence, numerous whirling structures which can be divided into three main families 2.2:

injection region on large-scale, created by the energy injection mechanism;

inertial region in which energy is transferred to increasingly smaller scales;

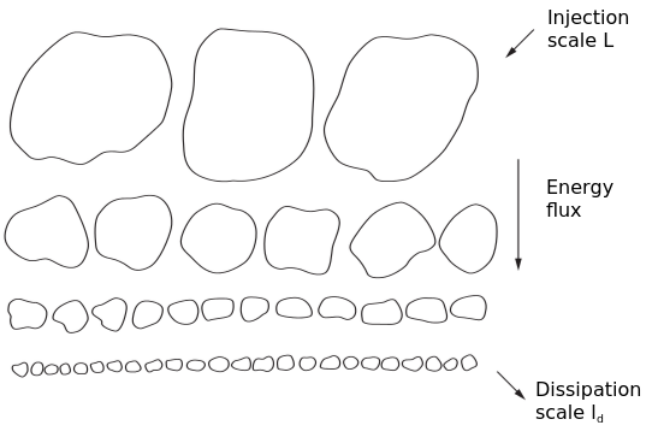

Figure 2.2: Schematic picture of the energy cascade. Image credit: `http://astro.physics.ncsu.edu/`.

dissipative region in which energy is dissipated due to viscous effects.

Kolmogorov has defined as a large scale the *integral* scale L, equivalent to the typical dimensions of the physical system under examination, which generates the production of turbulence. In addition, the larger-scale eddy structures, with typical dimensions of the order of L, are characterized by high Reynolds numbers, so the viscous term is negligible, from which it is obtained that the large structures do not dissipate, but extract energy from the mean motion to produce turbulent kinetic energy.

Concerning the turbulent structures in the inertial region, they occur on the *intermediate* scales and are generated by the non-linear instabilities of the larger eddies. It should be noted that their role is fundamental, since they transfer the turbulent kinetic energy produced at the integral scales to the smaller eddies, without having any significant effect on dissipation. The importance of intermediate scales lies in their universality property since they do not depend on the type of flux in which they evolve.

Finally, at the level of the *dissipative* scale, the (smaller) eddies are dominated by viscous phenomena. These phenomena have short characteristic times and are the fundamental contributors to the dissipation of kinetic energy coming from the larger scales.

Similarity properties give rise to a power law spectrum in the inertial range. In the case of a direct cascade, the inertial range is defined by

$$k_{\mathrm{in}} \ll k \ll k_{\mathrm{d}}\,,$$

where k_{in} and k_{d} indicate the wavenumbers related to the injection process and to the dissipation process, respectively. The inertial range is taken as the interval within which the spectrum exhibits a power law behavior. A typical spectrum is shown schematically in figure 2.3.
In the presence of an inverse cascade there is a second inertial range

$$L^{-1} \ll k \ll k_{\mathrm{in}}\,,$$

where the lower limit is geometrically determined by the size of the system.

The dynamics of the turbulence is controlled by energy injection with a rate of $\epsilon_{\mathrm{in}} \sim U^2/\tau_L$ where U is the velocity scale and τ_L is a characteristic time for the process of energy injection, which results to be $\tau_L \sim L/U$. In the case of a stationary situation the balance between the rates at different scales must be satisfied

$$\epsilon_{\mathrm{in}} = \epsilon_t = \epsilon_{\mathrm{d}} = \epsilon\,, \tag{2.28}$$

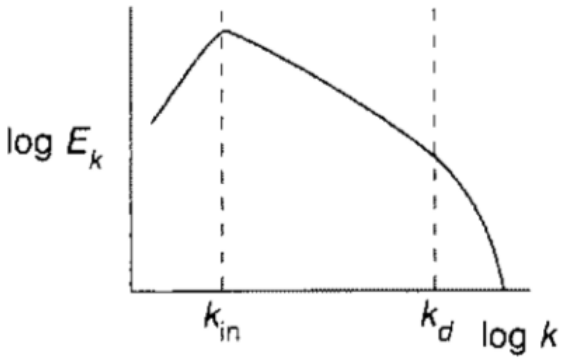

Figure 2.3: Logarithmic plot of a typical energy spectrum. Image credit: `https://slideplayer.com/`.

where ϵ_t is the transfer rate measured at any scale l, in the range $l_\mathrm{d} \ll l \ll L$, and $\epsilon_\mathrm{d} \sim U^2/\tau_\mathrm{d}$ is the energy dissipation rate at the scale L, where τ_d is the characteristic dissipation time which, starting from the Navier-Stokes equation (2.12), is estimated to be of the order of $\tau_\mathrm{d} \sim L^2/\nu$.
The relation (2.28) holds, to a good approximation, even when the injection rate varies with time, since the rapid small-scale dynamics in the inertial and dissipation ranges regulate the spectrum almost instantaneously at large scales, characterized by slower changes.

Considering a scale l_n in the range $l_\mathrm{d} \ll l_n \ll L$, associated with the wavenumber $k_n \sim l_n^{-1}$, we can write the typical time required for the transfer of energy between two nearby scales

$$\tau_n \sim \frac{l_n}{\delta u_n}\,, \tag{2.29}$$

where δu_n is the difference in velocity between the two scales l_n and l_{n+1}.
Because the energy flow is constant over the whole inertial range,

$$\frac{E_n}{\tau_n} \sim \frac{\delta u_n^3}{l_n} \sim \epsilon\,, \tag{2.30}$$

we found the scaling relation

$$\delta u_n \sim \epsilon^{1/3} l_n^{1/3}\,. \tag{2.31}$$

Then, with dimensional arguments, we can derive a law for the turbulent kinetic energy in the inertial range. This relation can be expressed as a function

of the wavenumber and the energy-transfer rate

$$E(k) = E_k = C_{\rm K}\epsilon^{2/3}k^{-5/3}\,, \tag{2.32}$$

which is the well-known *Kolmogorov spectrum*, widely observed in all experimental investigations of turbulence and considered as the main result of the K41 phenomenology of turbulence. The numerical factor $C_{\rm K}$, the Kolmogorov constant, is not determined by scaling arguments but requires a dynamic theory. The Kolmogorov spectrum has been observed in many types of turbulent flows, since it is independent of the geometry of the system and the way in which turbulence is generated, and also the value of the Kolmogorov constant seems to be universal, in particular it is independent of the Reynolds number. The data collected by Sreenivasan (1995) from many experiments, showed that $C_{\rm K}$ is invariant with a small statistical scatter

$$C_{\rm K} = 1.6 \; - \; 1.7\,,$$

over a broad range of Reynolds numbers, $30 \leq Re \leq 3 \times 10^4$; the authors of recent high-resolution numerical simulations have found a value of $C_{\rm K} = 1.65 \pm 0.05$ for $Re \simeq 500$ (Gotoh and Fukayama, 2001).

2.3.2 Iroshnikov-Kraichnan spectrum

The phenomenology of developed turbulence in the case dominated by the magnetic field has been studied by Iroshnikov (1963) and Kraichnan (1965) and then developed by Dobrowolny et al. (1980), to try to explain the occurrence of the observed alfvénic turbulence. In MHD turbulence the Alfvén effect[4] modifies the inertial range scale. According to this effect, small-scale fluctuations are not independent of the macro-state but are strongly influenced by the large-scale magnetic field, which causes the fluctuations to behave roughly like Alfven's waves.

Since non-linear interactions occur only between the fluctuations that propagate in the opposite direction along the magnetic field, the energy cascade undergoes a slowdown. This means that the characteristic time T_l, needed to efficiently transfer energy from one eddy to another at smaller scales, cannot be the time τ_l of the hydrodynamic turbulence (2.29), but it must be increased by a factor $\tau_l/\tau_{\rm A}$ (where $\tau_{\rm A} \sim l/\mathbf{c}_{\rm A}$ is the Alfvén time, that is the interaction

[4] According to the Alfvén effect, only the Alfvén waves that propagate in the opposite direction along a driving magnetic field interact.

time of two wave packets δz_l^+ and δz_l^-), so

$$T_l \sim \frac{(\tau_l)^2}{\tau_\mathrm{A}} \,. \tag{2.33}$$

Doing the substitution $\tau_l \to T_l$ in the (2.30) gives

$$\frac{\delta z_l^4 \tau_\mathrm{A}}{l^2} \sim \epsilon \,.$$

In other words both $\pm$ modes are transferred at the same rate to small scales ($\epsilon^+ \sim \epsilon^- \sim \epsilon$). This is not completely correct, because the Alfven effect causes that the energy transfer rates have the same scaling laws for $\pm$ modes but nothing can be said about the amplitudes of ϵ^+ and ϵ^-. However, when the energy transfer rate is constant, there is a scaling law different from that of Kolmogorov, in particular

$$\delta z_l \sim (\epsilon \mathbf{c}_\mathrm{A})^{1/4} l^{1/4} \,, \tag{2.34}$$

which corresponds to the energy spectrum

$$E_k = C_\mathrm{IK} (\epsilon \mathbf{c}_\mathrm{A})^{1/2} k^{-3/2} \,, \tag{2.35}$$

the *Iroshnikov-Kraichnan spectrum* (IK) of MHD turbulence. The coefficient C_IK (Iroshnikov-Kraichnan constant) should be different from C_K.
The spectrum is less steep than the Kolmogorov spectrum, since the factor τ_l/τ_A, by which the energy transfer time is longer, increases with decreasing of l, and therefore more and more high amplitudes are required, compared with the hydrodynamic case, in order to produce the same energy transfer.
Moreover, contrary to the Kolmogorov spectrum, which depends only on the quantity ϵ, the MHD energy spectrum depends also on the macroscopic quantity $\mathbf{c}_\mathrm{A}$ and thus cannot be derived from a dimensional analysis without further assumptions.

2.4 Intermittency

Turbulence is usually associated with the idea of self-similarity, which means that the spatial distribution of turbulence eddies is equal on any scale in the inertial range. This is a primary assumption in the phenomenology of Kolmogorov K41 and, on the same line, in the phenomenology of Iroshnikov-Kraichnan IK. Nevertheless, it is known that this picture is not exactly true, since it ignores the fact that small scale structures cannot be equally dis-

tributed so as to fill the whole space. In fact, the numerical simulations in the turbulence field show that the smaller eddies, those corresponding to higher frequencies, become more and more sparse in time and in space as the scale decreases. This behavior is called *intermittent* and apparently violates self-similarity.

A system is called self-similar or scale-invariant if it is reproduced by an enlargement of some part of it. Self-similarity is a widespread phenomenon both in physics and in biology, but it should be kept in mind that while a mathematical system can be exactly self-similar, in nature this property exists only for a certain range of scale.

2.4.1 Structure functions

To give a quantitative description of the turbulence, it is not enough just to take into account the behavior of the eddies of a certain size, but it is also necessary to consider the increase of the velocity, or some other field,

$$\delta\mathbf{u}(\mathbf{x},\mathbf{l}) = \mathbf{u}(\mathbf{x}+\mathbf{l}) - \mathbf{u}(\mathbf{x})$$

between two points separated by $\mathbf{l}$. Thus, it is obtained a longitudinal component

$$\delta u_{\parallel} = \delta\mathbf{u}(\mathbf{x},\mathbf{l}) \cdot \frac{\mathbf{l}}{l}$$

and two transverse, or lateral, components $\delta u_{\perp}$. The statistical distribution of the velocity of eddies of size l is described by the moments of the increments called *structure functions*, both longitudinal and lateral

$$S^{(n)}(l) = \langle [\delta u_{\parallel}(l)]^n \rangle \,, \qquad U^{(n)}(l) = \langle [\delta u_{\perp}(l)]^n \rangle \,,$$

where it is assumed that the turbulence is homogeneous and isotropic, such that the moments depend only on the distance l, and both transverse moments are equal. The set of moments $S^{(n)}(l)$ is equivalent to the probability distribution function (PDF) of the velocity increments.

The structure functions are related to the correlation functions

$$\langle u_1(\mathbf{x}) u_2(\mathbf{x}) \cdots u_k(\mathbf{x}) \rangle \,,$$

in particular to the longitudinal correlation functions

$$\langle u_{\parallel}(\mathbf{x})^{n-1} u_{\parallel}(\mathbf{x}+\mathbf{l}) \rangle = C^{(n)}(l)$$

and the simplest relations are

$$S^{(2)}(l) = 2\left[C^{(2)}(0) - C^{(2)}(l)\right], \qquad S^{(3)}(l) = 6C^{(3)}(l), \tag{2.36}$$

which can easily be verified. In the same way, we can found the relations between the lateral structure functions and the correlation functions of the transverse velocity components.

At the second order, the structure functions and correlation functions are related to the energy spectrum $E(k)$. In particular, it is obtained

$$C^{(2)}(l) = 2\int_0^\infty \left[-\frac{\cos(kl)}{(kl)^2} + \frac{\sin(kl)}{(kl)^3}\right] E(k)\, dk$$

and using the (2.36),

$$S^{(2)}(l) = 4\int_0^\infty \left[\frac{1}{3} + \frac{\cos(kl)}{(kl)^2} - \frac{\sin(kl)}{(kl)^3}\right] E(k)\, dk\,. \tag{2.37}$$

If the energy spectrum follows a power law of the type $E_k \sim k^{-\alpha}$, it is easy to verify that $S^{(2)} \sim l^{\alpha-1}$, since the relation (2.37), with $\kappa = kl$, becomes

$$S^{(2)} \sim l^{\alpha-1}\int_0^\infty \left[\frac{1}{3} + \frac{\cos\kappa}{\kappa^2} - \frac{\sin\kappa}{\kappa^3}\right] \kappa^{-\alpha}\, d\kappa\,, \tag{2.38}$$

where the integral converges for $1 < \alpha < 3$.

Higher-order structure functions play a crucial role in the theory of turbulence. The interest in structure functions derives from their scaling properties, unlike correlation functions that generally do not show scaling behavior. Thus in the inertial interval we get

$$S^{(n)}(l) = a_n l^{\zeta_n}\,. \tag{2.39}$$

This scaling property ensures that the complete information, in the inertial range, is contained in the set of scaling exponents ζ_n and in the coefficients a_n, fixed by the values of $S^{(n)}$ at some $l = l_0$. Self-similarity requires that the scaling exponents are linear in n

$$\zeta_n = cn\,, \qquad c > 0\,.$$

Note that the more general linear relation $\zeta_n = an + b$, $b \neq 0$, does not correspond to a self-similar behavior, but describes an intermittent system. The

phenomenology of Kolmogorov K41, $\delta u(l) \sim l^{1/3}$, implies the linear relation

$$\zeta_n = n/3\,,$$

while for the Iroshnikov-Kraichnan IK phenomenology

$$\zeta_n = n/4\,.$$

The information obtained from the direct simulations of the Navier-Stokes equation have allowed to reformulate the theoretical framework originally proposed by Kolmogorov. While the first experimental results and the first numerical simulations were in agreement with Kolmogorov's predictions, more accurate analysis showed small but significant deviations. In fact, the experimental data showed that the energy dissipation occurred intermittently and not uniformly as expected by Kolmogorov, that is the local dissipation rate varies rapidly in space and in time

$$\epsilon(\mathbf{x}) = \frac{1}{2}\nu \sum_{t,j} \left(\partial_t u_j + \partial_j u_t\right)^2 \,.$$

This give rise to some doubt about the rigorous validity of the K41 phenomenology (2.31),an inconsistency already noted by Landau after the publication of the Kolmogorov theory. Based on the criticism of Landau, Obukhov (1962) proposed that $\langle\epsilon\rangle$ in the K41 relation should be replaced by

$$\epsilon_l = \frac{1}{V_l}\int_{V_l} \epsilon(\mathbf{x}) dV\,,$$

obtaining the following scaling law

$$\delta u_l \sim \epsilon_l^{1/3} l^{1/3}\,,$$

from which

$$S_{\parallel}^{(n)}(l) = \langle[\delta u_{\parallel}(l)]^n\rangle = d_n \langle\epsilon_l^{n/3}\rangle l^{n/3}\,. \tag{2.40}$$

Indicating with μ_n the exponents of ϵ_l

$$\langle\epsilon_l^n\rangle \sim l^{\mu_n}\,,$$

if we put the (2.40) into (2.39) we get the relation

$$\zeta_n = \frac{1}{3}n + \mu_{n/3}\,. \tag{2.41}$$

2.4.2 Exact relations of turbulence

The phenomenological approach, such as the K41 theory and the more general framework of structure functions, is based exclusively on some symmetry properties of turbulence without a direct reference to dynamics, such as the Navier-Stokes equations.
There are, however, some exact relationships derived from the equations of dynamics, which require only the homogeneity and the isotropy of turbulence and are extremely useful when one wants to verify the validity of the hypotheses. Below we analyze three exact relations: the 4/5 law of Kolmogorov for the turbulence of Navier-Stokes, the 4/3 law of Yaglom for the scalar convection, and a relation for MHD turbulence.
The first relation was obtained by Kolmogorov (1941, 1991) and derives from the Navier-Stokes equation. So, from equation (2.40), for the third order structure function ($n = 3$), we obtain

$$S^{(3)}(l) = \langle (\delta u_{\parallel}(l))^3 \rangle = -\frac{4}{5}\epsilon l \,, \tag{2.42}$$

where $\epsilon = \langle \epsilon_l \rangle$ is the mean energy dissipation per unit mass, which is independent of the statistics ϵ_l. Since the relation (2.42) is valid in the inertial range for homogeneous and isotropic Navier-Stokes turbulence, it is often used to define the extension of the inertial range in observations and numerical simulations of turbulence.
For thermal convection Yaglom (1949) derived the 4/3 law in which the temperature (T) or any passive scalar[5](θ) follows a simple advection-diffusion equation. Using the properties of homogeneity and isotropy, we obtain

$$\langle \delta u_{\parallel} (\delta\theta)^2 \rangle = -\frac{4}{D}\epsilon_\theta l \,, \tag{2.43}$$

which is Yaglom's 4/3 law for scalar turbulence, with $D = 3$, where ϵ_θ is the scalar dissipation rate.
In the case of MHD turbulence we get

$$\langle \delta z_{\parallel}^{-} \delta z_i^{+} \delta z_i^{+} \rangle = -\frac{4}{D}\epsilon^{+} l \tag{2.44}$$

with ϵ^+ the dissipation rate. This relation represents the Yaglom's law for MHD turbulence, as obtained from Politano and Pouquet (1998), and is formally similar to both Yaglom's law for convection of a scalar field and to the

[5]With passive scalar we mean a scalar quantity that does not influence the state of velocity field; in other words, the velocity field influences the dynamics of the scalar, while the opposite does not happen.

Kolmogorov law for hydrodynamic turbulence. The main difference with respect to the latter is that the MHD relation (2.44) contains both longitudinal and lateral structure functions.

2.5 High frequency spectra

Magnetic fluctuations in solar wind have been studied in the past, based on the frozen-in approximation (Taylor's approximation) and its underlying hypothesis is that the advection due to turbulent fluctuations on small scales can be neglected and the advection of a turbulent field is considered solely due to the largest scales, since in turbulence most of the energy is contained in large integral scales. This hypothesis allows to interpret time series, measured at a single point in space, as spatial variations in the mean flow.
In a typical solar wind turbulence power spectrum (as shown in figure 2.4) three length scales can be identified: the Correlation or integral length λ_C represents the largest separation distance over which eddies are still correlated, the Taylor scale λ_T is the scale at which viscous dissipation begins to affect the eddies and the Kolmogorov scale λ_K characterizes the smallest dissipation-scale eddies.

The energy of very large-scale magnetic fluctuations is transported down to small scales by a turbulent cascade, into the kinetic range where the turbulent fluctuations can be dissipated by some mechanism. While the inertial range in solar wind can be described more or less in a way similar to the hydrodynamic turbulence, the dissipative region is likely to operate differently

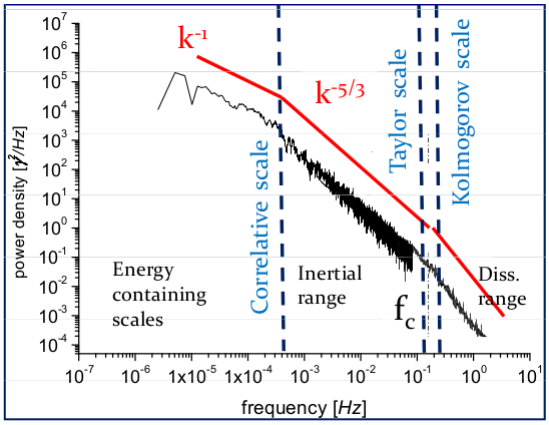

Figure 2.4: Typical power spectrum of interplanetary magnetic field at 1 AU. The low-frequency range refers to the Helios 2 observations (Bruno et al., 2009) while the high-frequency to WIND observations (Leamon et al., 1998). Image credit: Bruno and Carbone (2013).

from its fluid counterpart. The main reason for this is the fact that the solar wind behaves formally like a collisionless plasma, that is the usual viscous dissipation is negligible. At the same time, in a magnetized plasma there is a certain number of characteristic scales, then understanding the physics of the generation of small-scale region of turbulence is an important topic for the basic plasma physics.
With small scales we indicate scales that vary between the ion-cyclotron frequency $f_{\rm ci} = eB/m_i$ (or the ion inertial length $\lambda_i = c/\omega_{pi}$) and the electron-cyclotron frequency. Below the ion-cyclotron frequency, the spectrum follow the usual power law $f^{-\alpha}$ with a spectral index close to the Kolmogorov value of $\alpha \simeq 5/3$, while at higher frequencies the spectrum steepens significantly (typically $\alpha \simeq 7/3$) and Leamon et al. (1998) attribute this steepening to the occurrence of a dissipative range. However, how magnetic energy dissipates in the energy cascade still remains an open question.

Indeed, Perri et al. (2009) investigated the scaling behavior of the eigenvalues of the variance matrix of magnetic fluctuations, which give information on the anisotropy of the high-frequency region. The results indicate that this region is strongly anisotropic, since the minimum variance direction is almost parallel to the background magnetic field at scales larger than the ion-cyclotron scale. Another interesting result, below this scale, is that the eigenvalues of the variance matrix have a strong intermittent behavior with high localized fluctuations; this behavior generates a cross-scale effect in magnetic turbulence. The probability density functions of the eigenvalues evolve with the scale, becoming power laws at scales smaller than the ion-cyclotron scale. Then, it is not possible to define a characteristic value for the eigenvalues of the variance matrix at small scales. As a consequence, the absence of a characteristic value indicates that a typical power spectrum at small scales cannot be defined.

2.5.1 The dispersive range

The existence of a magnetic power spectrum with a slope close to 7/3 suggests that the high-frequency region can be interpreted as an energy cascade due to dispersive effects. So, in this region the Hall-MHD model can be used for the description of turbulence, since it is the most simple model to study dispersive effects in a fluid-like structure. Taking into account the effect of ion inertia, the generalized Ohm's law gives

$$\mathbf{E} = -\mathbf{u} \times \mathbf{B} + \frac{m_i}{\rho e}(\nabla \times \mathbf{B}) \times \mathbf{B}\,, \tag{2.45}$$

where the second term oh the right is the Hall term. Therefore, the equation (2.9) that describe the evolution of magnetic field over time becomes

$$\frac{\partial \mathbf{B}}{\partial t} = \nabla \times \left[\mathbf{u} \times \mathbf{B} - \frac{m_i}{\rho e} (\nabla \times \mathbf{B}) \times \mathbf{B} + \eta \nabla \times \mathbf{B} \right] , \tag{2.46}$$

which contains three different processes and then three different times. Introducing a length scale l, we have characteristic fluctuations ρ_l, B_l and u_l and we can define the eddy-turnover time $T_{NL} \sim l/u_l$ related to the convective process, an Hall time $T_H \sim \rho_l l^2/B_l$ and a dissipative time $T_D \sim l^2/\eta$.
The alfvénic turbulent cascade at large scales is realized in a time T_{NL}, while at small scales dissipation takes place. Instead, at intermediate scales the cascade is realized in a time T_H and the mean volume rate of the energy transfer becomes $\epsilon_V \sim B_l^2/T_H \sim B_l^3/l^2\rho_l$ because at these scales density fluctuations are important.

Since the energy cascade is considered as a hierarchy of eddies at different scales, we can write the ratio of the mass density between two successive levels $l_n > l_{n+1}$

$$\frac{\rho_n}{\rho_{n+1}} \sim \left(\frac{l_n}{l_{n+1}} \right)^{-3r}$$

with $0 \leq |r| \leq 1$ a measure of the degree of compression; then, the spectral energy density becomes

$$E(k) \sim k^{-7/3+r} . \tag{2.47}$$

The scaling exponents observed in solar wind in the range $2 \leq \alpha \leq 4$ (Leamon et al., 1998), can be reproduced by degree of compression between $-5/6$ and $1/6$.

Chapter 3

Acceleration of energetic protons at interplanetary shocks

Populations of energetic particles are an important component of the heliospheric environment and they are distributed from the lower corona to the interface of the heliosphere with the interstellar medium. The majority of these energetic particles are accelerated by the variety of shock waves present in the solar wind. Solar energetic particles can originate either from a solar flare site or by shock waves associated with CMEs (Reames, 1999). In particular, CME driven shock waves in the corona and in the interplanetary space are thought to be the main locataions for the acceleration of SEPs in gradual events. An increase in the intensity of energetic charged particles observed in concomitance with an interplanetary shock (ESP) has been referred to as an energetic storm particle event. There are a wide variety of different types of ESP events: classical, spike, step-like or irregular according to their time profile (Lario et al., 2003). In any case the proton intensity increases are more frequently observed in the low-energy ion fluxes. Another important population of energetic particles are those associated at Corotating Interaction Region (CIR) related shock waves, where CIRs are produced by the interaction between fast and slow solar wind streams.
The association of energetic particles with collisionless shocks implies an acceleration mechanism that is related with the shock itself.
In this work we performed a correlation analysis between the energetic proton flux enhancements and the magnetic field turbulence observed in the upstream and downstream regions of interplanetary shocks, by using in situ data recorded by instruments onboard the STEREO Ahead spacecraft to understand if turbulence can play a role in particle acceleration. Hence, we investigated the energy spectra of the protons measured during enhancements

at shock waves, that give information on the propagation and acceleration of the particles in the interplanetary space to possibly discuss the acceleration mechanisms at work.
We remark that it is very important to study the populations of energetic particles in order to understand the particle acceleration mechanisms, which is still an unsolved key fundamental problem in Astrophysics and fundamental Physics. Moreover, solar energetic particles are very important in the space weather contest as they can impact on the Earth's magnetosphere and this can affect short-circuiting power grids that cause blackouts, disrupting communications, damaging satellites, and endangering astronauts with radiation.

3.1 Acceleration mechanisms

One of the most interesting questions of astrophysics concerns the processes that can accelerate particles to high energies in space plasmas. All acceleration mechanisms are electromagnetic in nature. The acceleration process, in the most general situation, is described by the equation of motion for a charged particle

$$\frac{d}{dt}(\gamma m\mathbf{v}) = q\,(\mathbf{E} + \mathbf{v} \times \mathbf{B}) \tag{3.1}$$

where $\gamma = 1/\sqrt{1 - v^2/c^2}$ is the Lorentz factor, m is the proton mass, q is the proton charge, $\mathbf{v}$ is the velocity, $\mathbf{E}$ and $\mathbf{B}$ are the electric and magnetic fields, respectively. The acceleration of particles is due to magnetic fields variable over time. In fact, in completely ionized gases, the electric fields can not be maintained stationary because free charged particles, recombining, cancel any other electric field. Therefore, only changing magnetic fields, which determine the formation of induced electric fields, can lead to acceleration mechanisms. Acceleration can occur in very extensive sources and with not much intense magnetic fields, like the waves produced in the explosion of supernovae, or in extremely compact objects with rapidly variable magnetic fields, such as rotating neutron stars and pulsars with very small periods of rotation.

The acceleration of the particles can be regular or stochastic. The first acceleration mechanism is very fast but occurs in regions with extremely high density, in which the loss of energy for collisions becomes important.
On the other hand, stochastic acceleration mechanisms they are characterized by a continuous but gradual increase in energy of the particles, following successive crossings of a region with non homogeneous magnetic field. Processes of this type, even if they are rather slow, have the advantage of producing energy spectra that can cover several decades.

3.1.1 Stochastic and diffusive shock acceleration

Diffusion of charged particles in the turbulent magnetic fields carried along with a moving plasma is a possible mechanism for energy gains and losses. Fermi (1949) first postulated that the particles are accelerated via diffusion as a result of collisions with non-uniform magnetic fields in random motion in the interstellar medium. This perturbation of the field behaves like a magnetic mirror, in motion with a speed $v = \beta c$, where c is the light speed. Following each reflection on this mirror, the particles can either gain or lose energy in a given encounter, depending on whether the particle-cloud scattering is head-on or tail-on. After many encounters there is a net gain of energy, so that particles would, on average, be accelerated.
This process is called *second-order Fermi acceleration*, or *stochastic acceleration* because the mean energy gain per bounce depends on the mirror velocity squared, β^2. This is thought to be the primary mechanism by which particles gain non thermal energies in many astrophysical environments, such as radio galaxies, solar flares, the interstellar medium, and supernova remnants.

The mechanism just described is considered to be inefficient in accelerating particles to high energies. A more efficient mechanism is the *first-order Fermi acceleration*, or *diffusive shock acceleration* (DSA), in which the particles are accelerated by a shock wave and in this case the energy gain is proportional to β.
Shock waves typically have magnetic inhomogeneities in the upstream and downstream regions. Consider the case of a charged particle traveling through the shock wave (from upstream to downstream). If it encounters a change in the magnetic field, this can reflect it back through the shock (downstream to upstream) at increased velocity. If a similar process occurs upstream, the particle will again gain energy. These successive reflections greatly increase its energy. This mechanism only requires the existence of a shock and of scattering processes on both sides of the shock wave. Another important aspect is the perfect symmetry between the processes occurring both upstream and downstream of the shock.
The energy spectrum of particles undergoing this process turns out to be a power law, that explain the observed cosmic ray spectrum up to about 10^{15} eV (Blandford and Eichler, 1987).
Furthermore, Giacalone (2012), in a study of particle acceleration at interplanetary shock, highlighted that the energy spectra are consistent with a power law dependence at low energies (in the range from a few tens up to a few hundred of keV), in agreement with that predicted by DSA. However, this

acceleration mechanism does not fully address the several problems related to the phenomenon.
Moreover, observations of Solar Energetic Particle (SEP) events have shown that the predicted power law is valid on a limited energy interval (Mewaldt et al., 2005), below a characteristic energy where the spectrum has a rollover. This rollover energy is supposed to depend on various conditions at the interplanetary shock. In fact, the form of the energy spectral rollover is affected by the rate of ion escape upstream of the foreshock and by the nonlinear evolution and magnetic field amplification in the foreshock, that controls the acceleration timescale (Lee et al., 2012).
Ellison and Ramaty (1985) argued that the power law spectra should rollover at high energies due to increasing diffusion coefficient with energy and introduced an exponential decay to take into account this feature.
Moreover, at quasi-perpendicular shock the upstream wave energy density which is responsible for particle scattering may to be not sufficient. For instance, Zank et al. (2006) developed a basic theory for particle acceleration at highly perpendicular shocks based on the convection of solar wind turbulence into the shock. Assuming that the particles can be injected and accelerated diffusively at the shock, they showed how the injection energy increases with increasing obliquity; in fact, quasi-perpendicular shocks require much higher energies than quasi-parallel shocks. Perpendicular interplanetary shocks are more probable to accelerate a preexisting energetic particle population, such as flare accelerated particles, than in situ solar wind particles. Diffusive shock acceleration is difficult at nearly perpendicular shocks.

3.1.2 Shock drift and shock surfing acceleration

Since the diffusive shock acceleration requires the ions to cross the shock front many times, quasi-perpendicular shocks present a theoretical problem because the magnetic field prevents the ions from coming back upstream. It has been shown that a minimum velocity, equal to a few times that of the upstream solar wind plasma, is sufficient to overcome this barrier (Webb et al., 1995). In other words, Larmor radii must be large enough to allow the orbits to reach the shock front after turbulent backscattering collisions. Considering that ions within the upstream region are not sufficiently heated to satisfy this criterion, a pre-injection mechanism is required.
Two non-Fermi mechanisms, that can give particles pre-acceleration to reach the energy threshold required to start the DSA at quasi-perpendicular shocks, have been proposed: *shock drift*, SDA, (Pesses et al. (1982); Decker (1988))

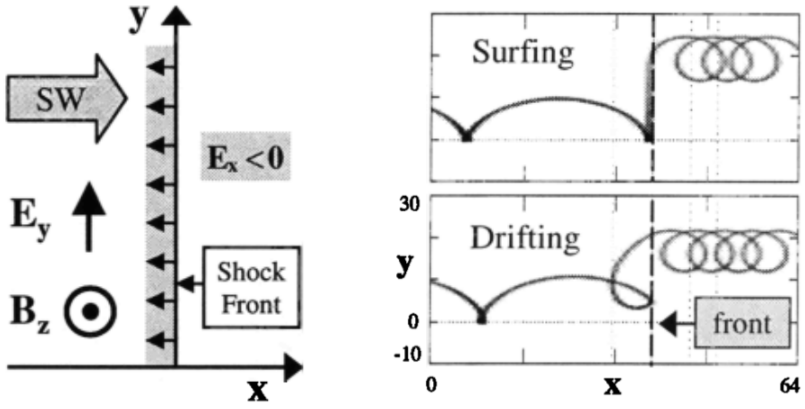

(a) **(b)**

Figure 3.1: Panel (a) shows a pattern of a perpendicular shock geometry and the orientations of electric and magnetic fields. Panel (b) is a plot of the trajectories of particles in shock surfing and drift shock acceleration, respectively from the top to the bottom. Image credit: Lever et al. (2001).

and *shock surfing*, SSA, (Sagdeev (1966); Lee et al. (1996); Zank et al. (1996)).

Consider a perpendicular shock with the orientation of the fields as shown in figure 3.1a, where the solar wind velocity $\mathbf{u}$ is in the x direction, $\mathbf{u} = u\widehat{x}$, the magnetic field is along z, $\mathbf{B} = B\widehat{z}$ and the shock normal is $\mathbf{n} = -\widehat{x}$, namely positive x is downstream. In the shock stationary frame, the flowing magnetized plasma produces a convective electric field, $\mathbf{E}_{\rm c} = -\mathbf{u} \times \mathbf{B}/c$. So, the ion guiding centers drift downstream at the mean plasma velocity without movement perpendicular to the bulk flow.
In the shock drift acceleration, the central source for the displacement of the guiding center is the magnetic field gradient at the shock ramp. It causes a drift of particle guiding centers so that the particles can gain energy moving along the direction of the convective electric field as they proceed downstream through the front. In other words, the electric potential energy is converted in kinetic energy.

In the shock surfing model, particles may be trapped upstream of the shock (they surf the wave) and accelerated, along the shock front and perpendicularly to the magnetic field, through the combined action of the electrostatic potential gradient and the Lorentz force. Particles are de-trapped when reach enough kinetic energy to breach the potential barrier and escape downstream (figure 3.1b). The speed

$$v \simeq v_A \left(\frac{m_p}{m_e}\right)^{1/2} (M_A - 1)^{3/2}\,, \tag{3.2}$$

where v_A is the Alfvén velocity, m_p/m_e is the ratio between the ion and electron mass and M_A is the Alfvén Mach number (Ohsawa, 1987).
It is found from a nonlinear wave theory based on a two-fluid cold plasma model that in a magnetosonic shock wave a potential jump ($e\varphi \simeq 2m_p v_A^2(M_A - 1)$) is formed; its dependence on the propagation angle θ is rather weak. On the other hand, the width of a quasi-perpendicular shock is of the order of the electron inertial length ($\Delta \sim (c/\omega_{pe})[2(M_A - 1)]^{-1/2}$) for shocks having propagation angles in the region $\theta_c \lesssim \theta \leqq 90°$, where θ_c is 88.7° for a proton plasma. Hence, the electric field strength normal to the wave front ($E \sim \varphi/\Delta$) is very strong. Since the particles trapped by a quasi perpendicular shock can be accelerated to the drift speed, $v \sim cE/B$, they can be accelerated up to the speed given by equation (3.2). For the oblique shocks with $\theta \ll \theta_c$, the width of shock is rather large and, then, the resonant acceleration is about $(m_p/m_e)^{1/2}$ times smaller than that in a quasi-perpendicular shock.
Trapped ions move in the direction of the wave propagation with a speed similar to that of the shock wave. So, an ion velocity along the wave front increases with the time t as $v \simeq \omega_p v_{sh} t$, where ω_p is the proton cyclotron frequency and $v_{sh} = M_A v_A$ is the propagation speed of the shock. Consequently, also the kinetic energy increases with the time, according to the relation

$$E \simeq \frac{m_p}{2}\omega_p^2 v_{sh}^2 t^2 \,. \tag{3.3}$$

Therefore, the trapped ions can be accelerated up to the maximum velocity given by equation (3.2) in a time

$$t_{max} \simeq \left(\frac{m_p}{m_e}\right)^{1/2} \omega_p^{-1} M_A^{-1} \,, \tag{3.4}$$

obtained using the electric field normal to the wave front ($E \sim (m_p/q_p)v_A^2$ $(c/\omega_{pe})^{-1}(M_A - 1)^{3/2}$, where ω_{pe} is the electron plasma frequency).
So, it is as if the surfing ion is temporarily delayed by the quasi perpendicular shock and accelerated during its permanence at the shock front when it feels the convective electric field.

3.2 Datasets

3.2.1 STEREO spacecraft

STEREO (Solar TErrestrial RElations Observatory) is a solar observation mission, the third in NASA's Solar Terrestrial Probes program (STP). It consists of two nearly identical probes launched into orbits that provide

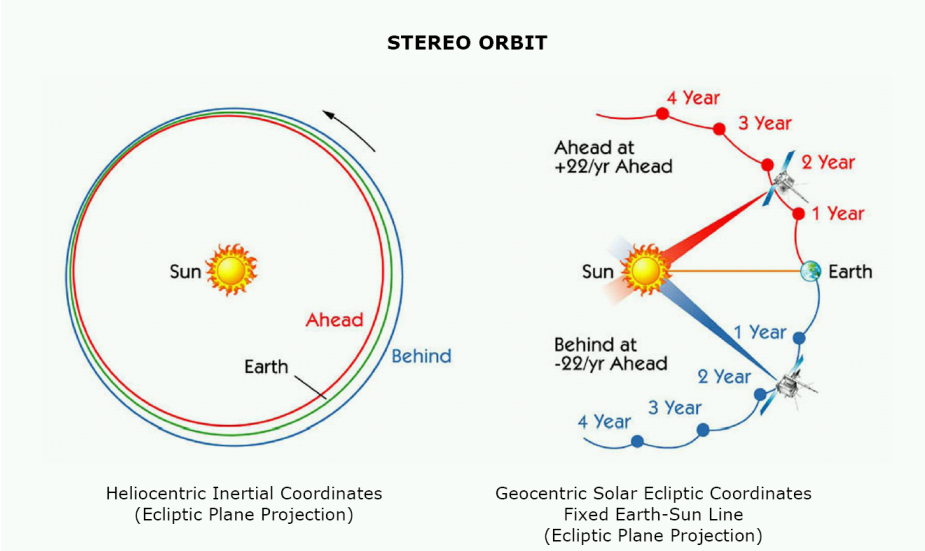

Figure 3.2: Orbits of STEREO observatories and Earth. Image credit: `https://it.wikipedia.org/`.

stereoscopic images of the Sun. Because the satellites are at different points along the Earth's orbit, but distant from the Earth (figure 3.2), they can photograph parts of the Sun that are not visible from the Earth. This permits to directly monitor the far side of the Sun, instead of deducing the activity on the far side from data that can be obtained from Earth's view of the Sun.
In particular, STEREO's scientific objectives are to understand the causes and mechanisms of coronal mass ejections (CMEs) start and to describe their propagation through the heliosphere, to discover the mechanisms and sites of energetic particle acceleration in the low corona and the interplanetary medium and, overall, to better interpret the structure of the solar wind. Before STEREO, the detection of the sunspots that are associated with CMEs on the far side of the Sun was only possible using helioseismology, which gives low-resolution maps of the solar activity. Considering the Sun rotates every 25 days, some detail on the far side was invisible to Earth; so this was one of the principal reasons for the STEREO mission.

The two STEREO spacecraft were launched on October 26, 2006, from Cape Canaveral Air Force Station in Florida, on a Delta II rocket into highly elliptical geocentric orbits. The two space probes were in slightly different orbits, the "ahead" (A) spacecraft was ejected to a heliocentric orbit inside Earth's orbit while the "behind" (B) spacecraft, being released in the opposite direction from spacecraft A, entered a heliocentric orbit outside the Earth's orbit. STEREO A takes 347 days to complete one revolution of the Sun and STEREO B takes 387 days.

The following four instrument packages are mounted on each spacecraft:

- The Sun-Earth Connection Coronal and Heliospheric Investigation (SECCHI) pictures and studies coronal mass ejections during their entire journey;
- STEREO/WAVES (SWAVES) instrument monitors radio disturbances travelling from Sun to Earth;
- PLAsma and SupraThermal Ion Composition (PLASTIC) studies CME particles (protons, alpha particles and heavy ions);
- In-situ Measurements of Particles and CME Transients (IMPACT) samples the three-dimensional distribution of solar wind electrons, energetic particles and interplanetary magnetic field.

Plasma characteristics of protons, alpha particles and heavy ions are provided by PLASTIC instrument. This experiment gives measurements of mass and charge state composition of heavy ions, distinguishing the CME plasma from ambient coronal plasma.
IMPACT samples the 3-D distribution of solar wind plasma electrons, the characteristics of the solar energetic particles (SEP) ions and electrons accelerated in coronal mass ejections and solar flares, and the local magnetic field vector. It is a suite of seven instruments:

- SWEA (Solar Wind Electron Analyzer) is designed to measure the distribution function of the solar wind electrons from below 1 eV to several keV, with high spectral and angular resolution;
- STE (Suprathermal Electron Telescope) detects electrons in the energy range $2 - 20$ keV, which are the superhalo component of the solar wind electron distribution;

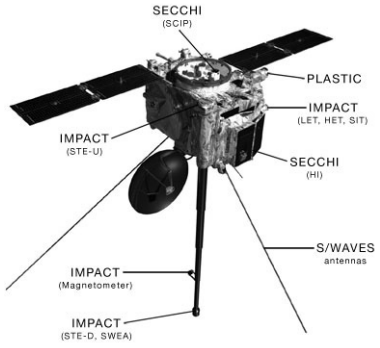

Figure 3.3: The scientific instrumentation on board the two STEREO probes. Image credit: `https://it.wikipedia.org/`.

- MAG (Magnetometer) is a tri-axial flux gate with sensors that use a ring core geometry;
- SEPT (Solar Electron Proton Telescope) consists of two telescopes that separate and measure electrons in the energy range $20 - 400$ keV and protons from 20 to 7000 keV;
- SIT (Suprathermal Ion Telescope) is a time-of-flight ion mass spectrometer that determines elemental composition of He-Fe ions over the energy range 30 keV/nucleon to 2 MeV/nucleon;
- LET (Low Energy Telescope) is made up of 14 detectors designed to measure protons and helium ions from 1.5 to 13 MeV/nucleon, and heavier ions from 2 to 30 MeV/nucleon;
- HET (High Energy Telescope) consists of six detectors designed to estimate protons and helium ions to 100 MeV/nucleon, and energetic electrons to 5 MeV.

The first three of these are located on the IMPACT boom/mast that extends a total of 4.5 meters antisunward on each spacecraft, while the latter four instruments make up the SEP subsystem which is mounted on the spacecraft body.

3.2.2 Selection of events

We studied particle enhancements at interplanetary shocks, by using STEREO A data over the period $2009 - 2016$. The events studied have been selected by comparing two interplanetary shock lists. The first is the Heliospheric Shock Database generated and maintained at the University of Helsinki, `http://ipshocks.fi/database/`; while the second can be found at the following link, `http://www-ssc.igpp.ucla.edu/forms/stereo/stereo_level_3.html`, compiled by Jian et al. (2013).
These lists include the time of each shock passage at the spacecraft and different characteristics of the shock, such as the magnetosonic Mach number, the compression ratio, the shock-normal angle and the plasma beta. In addition, the lists give information about the type of the shock, forward or reverse, and the source of the shock, such as a SIR (Stream Interaction Region) or an ICME (Interplanetary Coronal Mass Ejection).

We selected only shocks at which an effective enhancement in proton flux is observed at energies $4 - 6$ MeV. We used the $4 - 6$ MeV LET data because

it is an intermediate energy range above > 1 MeV where particle acceleration might be produced by a different mechanism that work at few hundreds keV (Kallenrode, 1996). Nevertheless, it is not too huge to prevent a good statistical sample of events given that the occurrence frequency of ESPs is a decreasing function of the energy (Dresing et al., 2016). To evaluate the real increase in proton flux, we used a pre-increase flux (background) value (before the shock passage time) where the solar wind is almost undisturbed. Thus, if j_{peak} indicates the maximum proton flux value within few hours around the shock, and $j_{background}$ is the background value, the relative increase in proton flux is given by the

$$j_{normalized} = \frac{j_{peak}}{j_{background}}. \tag{3.5}$$

To simplify the notation, hereinafter we will use j_p, j_b and j_n instead of j_{peak}, $j_{background}$ and $j_{normalized}$, respectively.

If the value of j_n was higher than 1.5, the event was considered as a ESP event. We recorded the data referred to the selected shocks in two separate lists, depending on how much the peak is close to the shock, in order to study its correlation with the shock itself: in the List 1 the events that present a peak within three hours before or after the shock passage time, in order to include most of the events of shock-spike type and those with increases of longer duration (table 3.1); while in the List 2 we collected those with the increment detected more than three hours before or after the shock up to 15 hours (table 3.2).

Finally, the identified ESP events were cross-checked with the list of solar energetic particle events, `https://umbra.nascom.nasa.gov/SEP/`. Consequently, we reported in the two tables if a SEP was in progress at the shock arrival (hereafter, we call these cases as SEP) or if it is not present at the shock passage (NO SEP). A number of 24 ESP events was identified in List 1, 16 of which are SEP whereas, 8 are not associated. List 2, instead, includes 14 ESP events, 9 are SEP while 5 are associated at NO SEP events.

Table 3.1: Parameters of the 24 shocks of the List 1, associated with enhancements in the proton flux. Columns: the number of the shock, doy, date, time, type (FF for Fast Forward shock and FR for Fast Reverse shock), source of the shock, coincidence with an SEP, ratio between the magnetic field downstream (B_{down}) and upstream (B_{up}), compression ratio ($\frac{N_{down}}{N_{up}}$), beta of the plasma (β), shock-normal angle (θ_{Bn}) and Mach number (M_{ms}).

#	DOY	DATE	TIME	TYPE	SOURCE	EVENT	$\frac{B_{down}}{B_{up}}$	$\frac{N_{down}}{N_{up}}$	β	θ_{Bn}	M_{ms}
1	46	15/02/2010	04 : 41 : 31	FF	a bump in solar wind	NO SEP	1.70	1.84	0.53	86.18	1.27
2	68	09/03/2011	06 : 47 : 40	FF	ICME	SEP	1.68	3.80	0.76	52.05	1.99
3	81	22/03/2011	18 : 21 : 06	FF	ICME	SEP	2.04	2.63	0.09	87.20	1.51
4	254	11/09/2011	08 : 51 : 29	FF	faster wind	SEP	1.78	2.00	0.22	88.68	1.29
5	332	28/11/2011	14 : 51 : 25	FF	ICME	SEP	2.48	4.18	0.87	61.97	1.87
6	04	04/01/2012	16 : 40 : 39	FF	SIR (embedded ICME)	SEP	1.51	2.46	0.71	32.69	0.93
7	29	29/01/2012	13 : 04 : 18	FF	ICME	SEP	2.81	4.38	0.39	86.92	1.86
8	78	18/03/2012	19 : 30 : 49	FF	ICME	SEP	2.00	3.06	0.79	48.31	1.64
9	79	19/03/2012	19 : 17 : 43	FF	ICME	SEP	1.47	1.42	0.28	44.50	1.66
10	149	28/05/2012	02 : 48 : 40	FF	ICME	SEP	5.89	10.13	0.93	73.21	2.60
11	177	25/06/2012	20 : 55 : 59	FF	ICME	NO SEP	2.26	3.91	0.64	46.16	1.26
12	191	09/07/2012	02 : 33 : 26	FF	SIR	SEP	1.92	2.10	0.58	17.68	1.56
13	25	25/01/2013	00 : 14 : 12	FF	ICME	NO SEP	1.52	3.10	1.05	88.46	1.10
14	112	22/04/2013	10 : 08 : 20	FF	ICME	NO SEP	2.50	4.68	1.95	78.52	1.75
15	305	01/11/2013	10 : 55 : 16	FF	ICME	NO SEP	2.05	2.83	1.05	48.78	1.39
16	335	01/12/2013	22 : 29 : 46	FF	ICME	SEP	2.95	9.78	0.17	85.66	1.75
17	36	05/02/2014	03 : 27 : 37	FF	ICME	NO SEP	2.01	2.33	1.72	83.78	1.80
18	53	22/02/2014	08 : 00 : 03	FF	ICME	SEP	2.07	3.09	1.20	61.88	1.54
19	53	22/02/2014	23 : 06 : 24	FF	ICME	SEP	1.74	2.59	1.66	79.48	1.30
20	162	11/06/2014	00 : 14 : 42	FF	ICME	SEP	2.20	2.86	1.54	88.49	1.54
21	193	12/07/2014	17 : 19 : 11	FF	ICME	SEP	2.29	2.41	0.58	74.27	1.79
22	223	11/08/2014	09 : 03 : 27	FF	ICME	NO SEP	1.90	3.85	0.12	38.52	0.91
23	09	09/01/2016	18 : 08 : 20	FF	ICME	SEP	1.41	/	1.89	48.52	1.41
24	216	03/08/2016	17 : 11 : 29	FF	SIR	NO SEP	1.45	/	1.62	78.15	1.34

Table 3.2: Parameters of the 14 shocks of the List 2, associated with enhancements in the proton flux. Columns: the number of the shock, doy, date, time, type (FF for Fast Forward shock and FR for Fast Reverse shock), source of the shock, coincidence with an SEP, ratio between the magnetic field downstream (B_{down}) and upstream (B_{up}), compression ratio ($\frac{N_{down}}{N_{up}}$), beta of the plasma (β), shock-normal angle (θ_{Bn}) and Mach number (M_{ms}).

#	DOY	DATE	TIME	TYPE	SOURCE	EVENT	$\frac{B_{down}}{B_{up}}$	$\frac{N_{down}}{N_{up}}$	β	θ_{Bn}	M_{ms}
1	356	22/12/2009	23 : 51 : 15	FR	SIR	NO SEP	1.91	1.77	1.27	53.74	2.02
2	167	16/06/2011	03 : 10 : 22	FF	SIR	NO SEP	2.49	4.28	0.92	57.16	1.96
3	78	18/03/2012	19 : 30 : 49	FF	ICME	SEP	2.00	2.16	0.79	48.31	1.64
4	191	09/07/2012	02 : 33 : 26	FF	SIR	SEP	1.92	2.10	0.58	17.68	1.56
5	202	20/07/2012	06 : 00 : 58	FF	SIR	SEP	2.48	7.76	0.77	50.42	1.37
6	202	20/07/2012	22 : 43 : 10	FF	ICME	SEP	1.81	2.62	1.66	25.31	2.26
7	245	02/09/2013	02 : 19 : 45	FF	SIR	NO SEP	1.22	2.30	0.73	0.34	0.60
8	360	26/12/2013	05 : 04 : 11	FR	SIR (embedded ICME)	SEP	1.72	1.32	1.45	81.19	1.49
9	20	20/01/2014	19 : 21 : 50	FF	front edge of SIR	NO SEP	1.86	1.41	0.48	62.56	2.22
10	32	01/02/2014	06 : 19 : 25	FF	slow wind	SEP	1.63	1.75	0.98	62.96	1.12
11	70	11/03/2014	09 : 37 : 09	FF	ICME	SEP	2.86	5.76	1.21	62.69	1.98
12	89	30/03/2014	21 : 38 : 00	FF	ICME	SEP	2.83	6.53	0.78	39.48	2.51
13	178	27/06/2014	21 : 58 : 00	FF	1 day before SIR	NO SEP	1.48	1.23	1.25	37.92	2.52
14	09	09/01/2016	18 : 08 : 20	FF	ICME	SEP	1.41	/	1.89	48.52	1.41

Figures 3.4 and 3.5 show two examples of events (SEP and NO SEP associated) with ion intensities taken, respectively, from SEPT instrument in the top panel, from LET in the middle panel and from HET instrument in the lower panel.

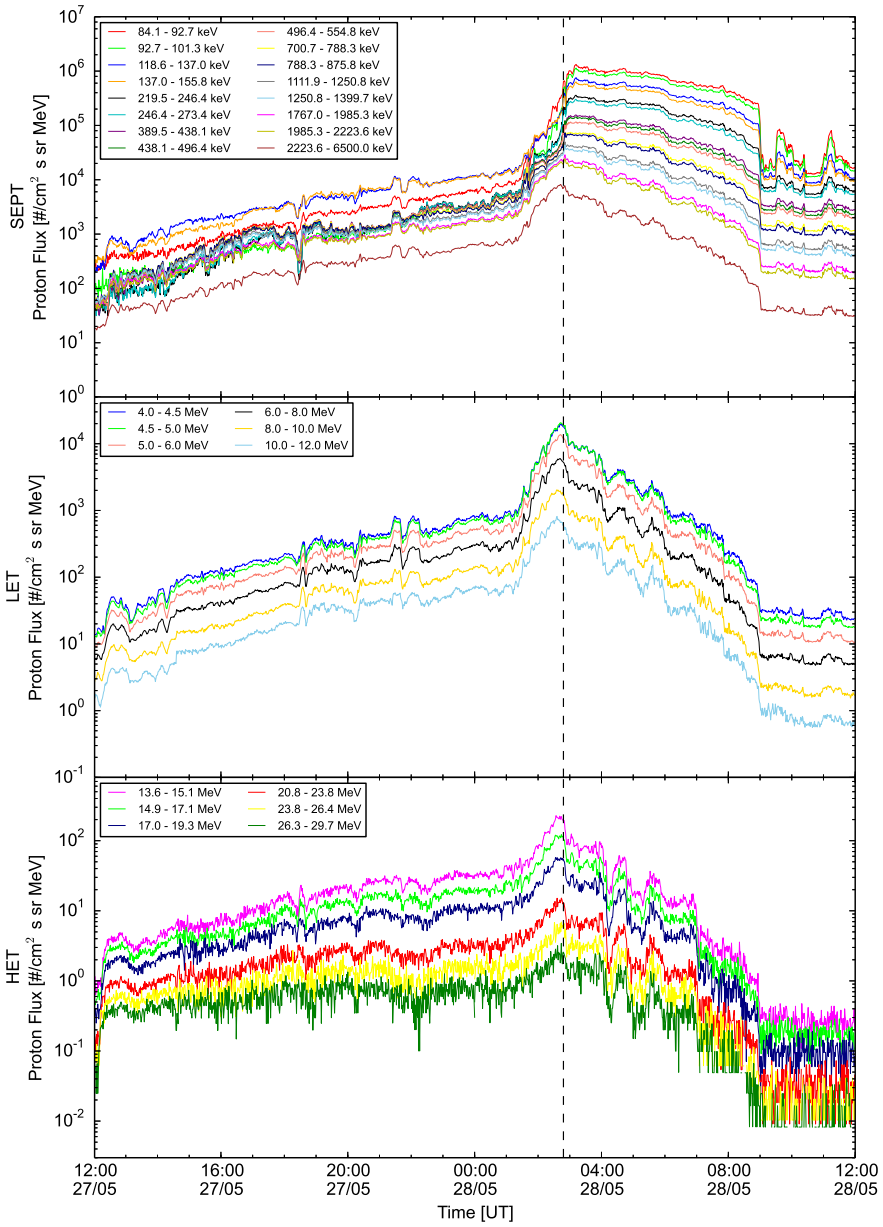

Figure 3.4: Ion intensities around the shock crossing on 28 May 2012, 02 : 48 UT (shock #10 of the List 1), observed by STEREO A. The upper panel shows data recorded by SEPT instrument in the energy range of $84.1 - 6500.0$ keV, the middle panel displays proton intensties taken from LET in the energy range of $4.0 - 12.0$ MeV and the lower panel shows data in the energy range of $13.6 - 29.7$ MeV from HET. The vertical dotted line indicates the time of the shock passage over the spacecraft.

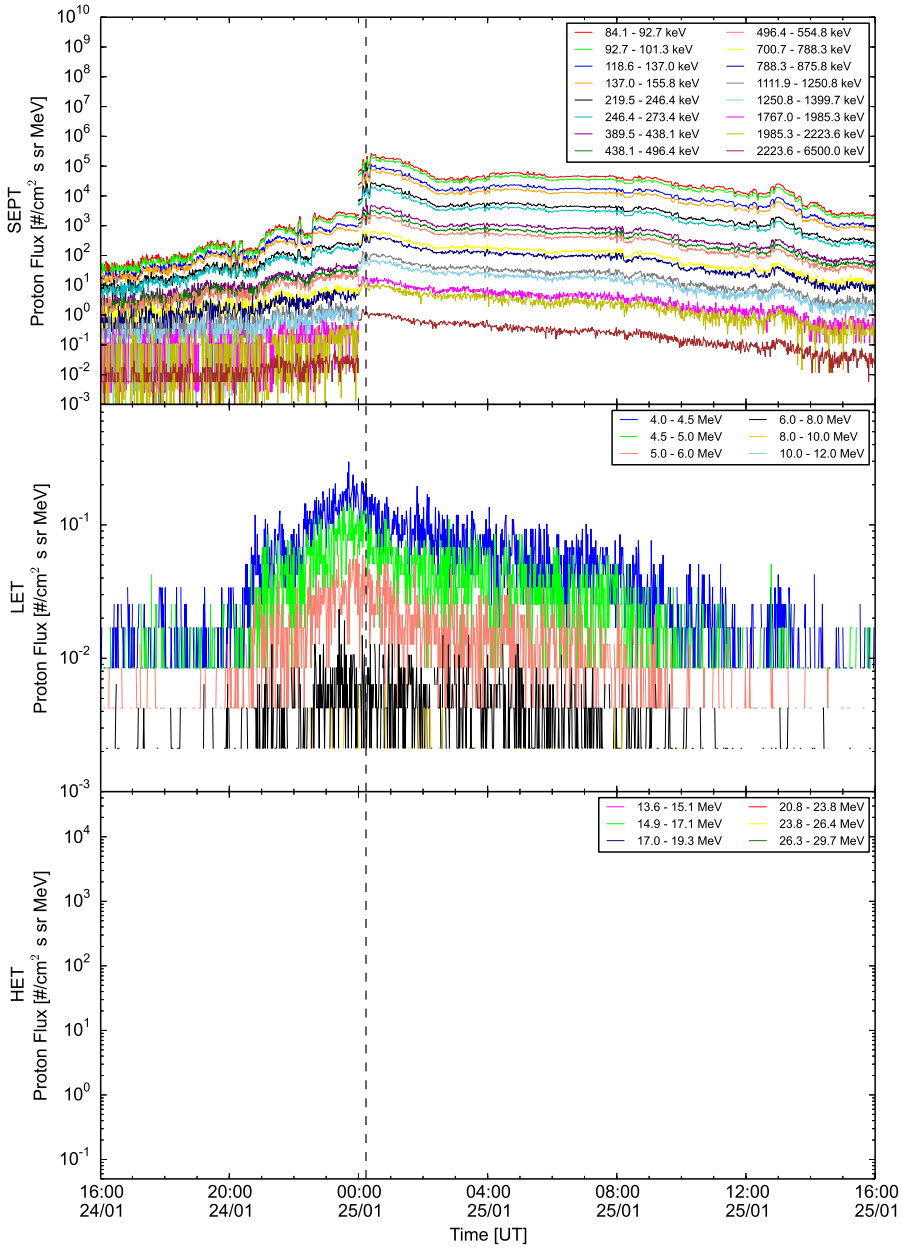

Figure 3.5: Ion intensities around the shock crossing on 25 January 2013, 00 : 14 UT (shock #13 of the List 1), observed by STEREO A. The upper panel shows data recorded by SEPT instrument in the energy range of $84.1 - 6500.0$ keV, the middle panel displays proton intensties taken from LET in the energy range of $4.0 - 12.0$ MeV and the lower panel shows data in the energy range of $13.6 - 29.7$ MeV from HET (there are no data for this energy range). The vertical dotted line indicates the time of the shock passage over the spacecraft.

3.2.3 Magnetic field and proton flux data

We performed the analysis of magnetic field turbulence around the shock using the two sets of data (List 3.1 and List 3.2) distinguishing between ESPs occurring during an SEP event and NO SEP events. The magnetic field data used in this study are provided in the RTN coordinate system. It is a coordinate system centered into the spacecraft. The Radial component, R, points from the spacecraft to the Sun, the Tangential component, T, is the cross product of the solar rotational axis and R axis, and lies in the solar equatorial plane and the Normal component, N, completes right handed triad.
We used magnetic field data with a high time resolution of 0.125 s from IMPACT/MAG instrument onboard STEREO A spacecraft, available at `https://cdaweb.sci.gsfc.nasa.gov/index.html/`. Instead, for the energetic proton flux enhancements we retrieved 1-hour averaged data of energetic particle intensities ($\#/\mathrm{cm}^2$ s sr MeV) in the energy range $4-6$ MeV measured by LET sensor onboard STEREO A, `http://www.srl.caltech.edu/STEREO/`. Figure

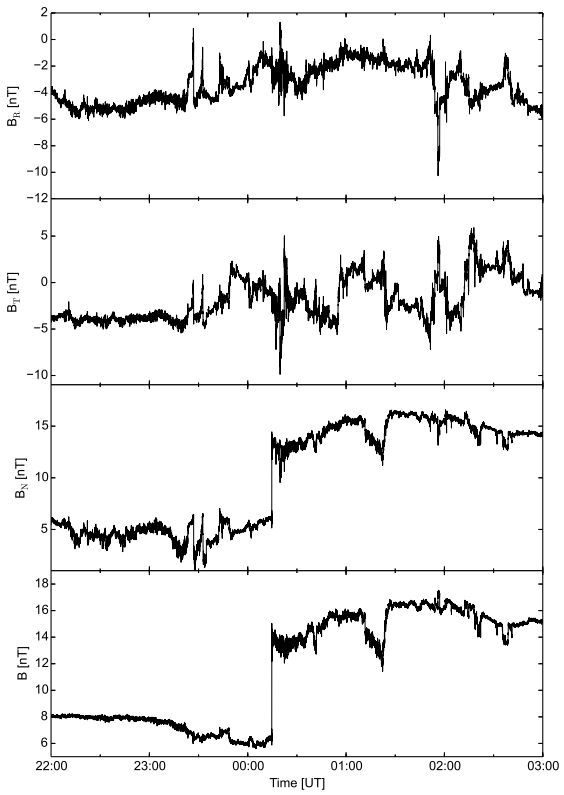

Figure 3.6: Magnetic field components and magnitude in solar-polar coordinates (RTN) with a time resolution of 0.125 s of the shock that occurred on 11 June 2014, 00 : 14 UT (shock #20 of the List 1).

(3.6) shows an example of the magnetic field measurements for the magnitude and the RTN-components for one of the selected shocks, denoted with the number #20 in the first List and occurred on 11 June 2014, 00 : 14 UT.

3.3 Analysis of magnetic field turbulence and energetic protons at interplanetary shocks

In this section we show the results obtained from the correlation analysis between the energetic proton flux enhancements in the $4 - 6$ MeV range and the magnetic field turbulence observed in the upstream and downstream regions of interplanetary shocks, by using in situ data recorded by the LET and IMPACT/MAG instruments onboard the STEREO Ahead spacecraft as described in the previous section.

3.3.1 Method of analysis

The spectral analysis at the selected shocks was performed both in the upstream region and in the downstream region of the shock, using a total sampling time of $t_{\max} = 4096$ s with a resolution of $t_{\min} = 0.125$ s.
In order to quantify the magnetic field turbulence we used the fast Fourier transformation (Yuen and Fraser, 1979). In this standard method for spectral analysis there are two frequency limits. First, an upper limit given by the Nyquist frequency $f_{\max} = f_{\mathrm{Ny}} = 1/2\, t_{\min}$; secondly, the inverse of the total sampling time $f_{\min} = 1/t_{\max}$ as a lower limit. Since the resolution of the IMPACT/MAG instrument is 0.125 s and the total sampling time of the magnetic field is 4096 s (that is approximatively 1 hour) we obtain a frequency range of $2.4 \cdot 10^{-4}$ Hz and 4 Hz.
In figure 3.7 we show an example of the spectra of the upstream turbulence related to the shock #20 in table 3.1, obtained with a standard FFT procedure for the magnitude and the RTN-components of the magnetic field. These panels show a different behavior for the magnitude and for the single components, but they do not display clearly distinct peaks.
Before the spectral analysis, it is essential to substract the mean value of the magnetic field. Hence, since we are interested just in the turbulent fluctuations, we define a turbulence measure as

$$T = \sum_{i=f_{\min}}^{f_{\max}} |F(i)| \tag{3.6}$$

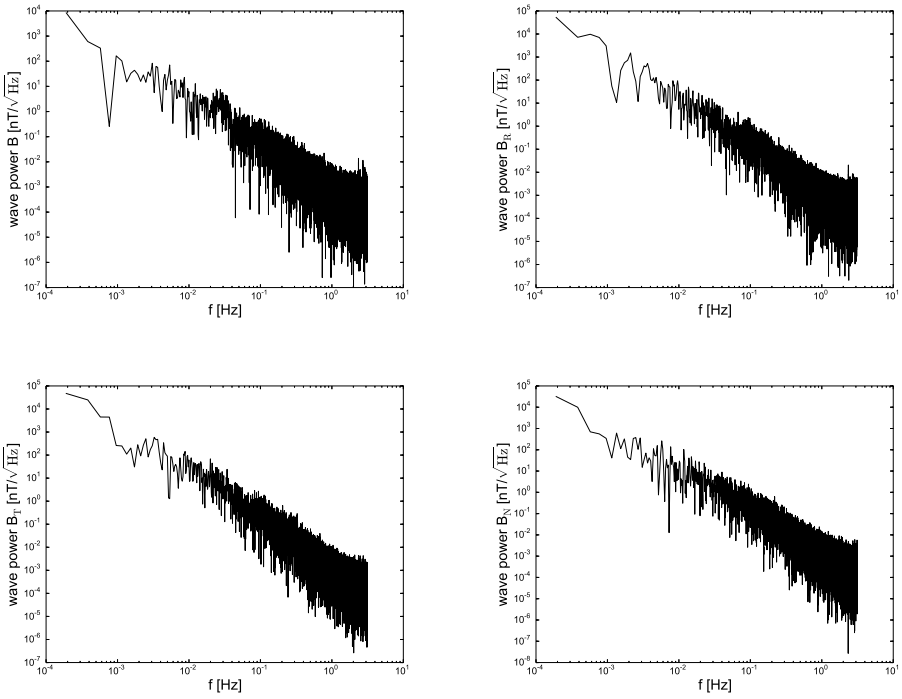

Figure 3.7: Spectral anaysis of shock occurred on 11 June 2014 at 00 : 14 UT in the upstream region for the magnitude and the RTN components of the magnetic field on a double logarithmic scale.

as the sum of the magnitude of the Fourier coefficients $F(i)$ obtained from the magnetic field after removing average. This turbulence measure was calculated both in the upstream and downstream regions of the shocks ($T_{\mathrm{up/down}}$). The measure of turbulence defined in equation (3.6) is the one used by Claßen et al. (1999), but we obtained similar results for correlation coefficients if we use the absolute square of the Fourier coefficients $|F(i)|^2$ or the variance σ^2.

Afterwards, we performed a correlation analysis between the $4-6$ MeV proton flux enhancements and the magnetic field turbulence. To this aim we used the proton flux $\mathrm{j_n}$ and the measure of turbulence T, as defined in the equations (3.5) and (3.6), respectively. The study was done both for the shocks belonging to the List 1 (see table 3.1) and those belonging to the List 2 (see table 3.2), making the distinction between the shocks occurring on the wake of a SEP event and those taking place on a great background (NO SEP).

Results for List 1

The following plots are obtained by applying the analysis described above for all the shocks of the first list, plotting the $4-6$ MeV proton flux enhancement $\mathrm{j_n}$ as a function of the turbulence measure T. This was done for all the components and for the magnitude of the magnetic field and in each figure we reported the correlation graphs of the upstream and downstream intervals of the shocks. In addition to the parametric correlation analysis, represented by the linear correlation coefficient r, we also performed a nonparametric analysis (Spearman's correlation), the results of which will be discussed later, although we can note that:

- the correlation coefficients are very low in the upstream region for any B components and magnitude;
- they are slightly better for the R and T components (i.e. those in the equatorial plane of the Sun) and magnetic field magnitude in the downstream region.

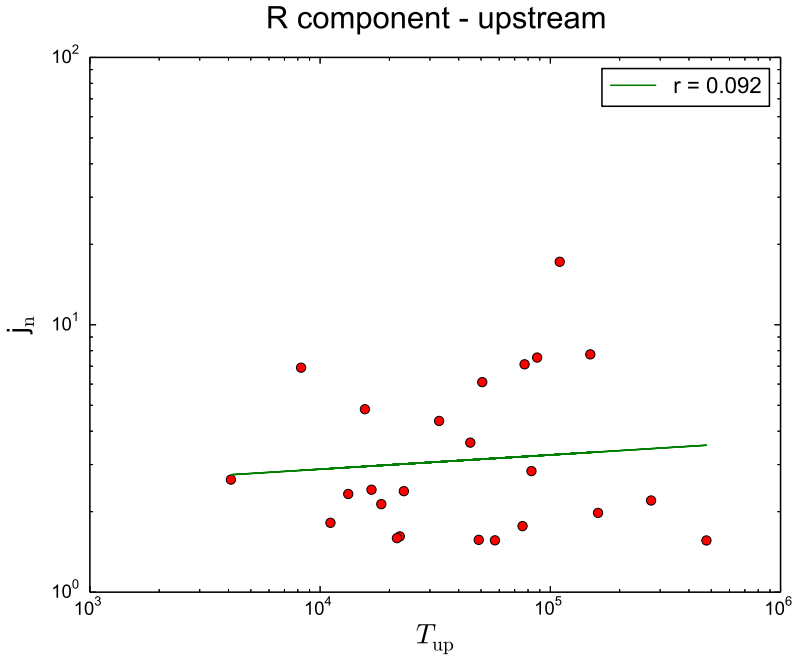

(a)

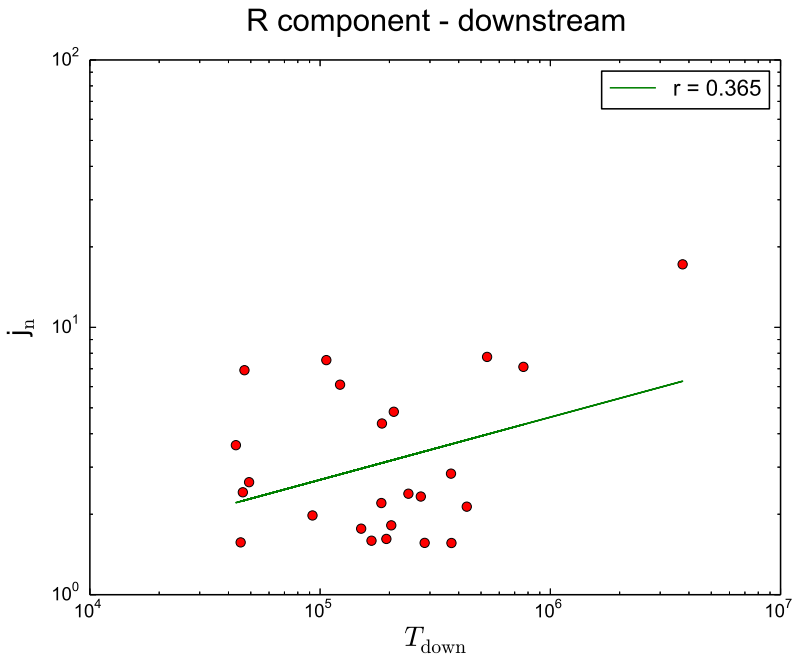

(b)

Figure 3.8: Proton flux enhancements in the $4-6$ MeV versus turbulence measure for the R component of the magnetic field for the shocks of the first list. Panel (a) shows the correlation in the upstream region of the shock while panel (b) in the downstream region. r is the correlation coefficient of the linear fit indicated by the green line.

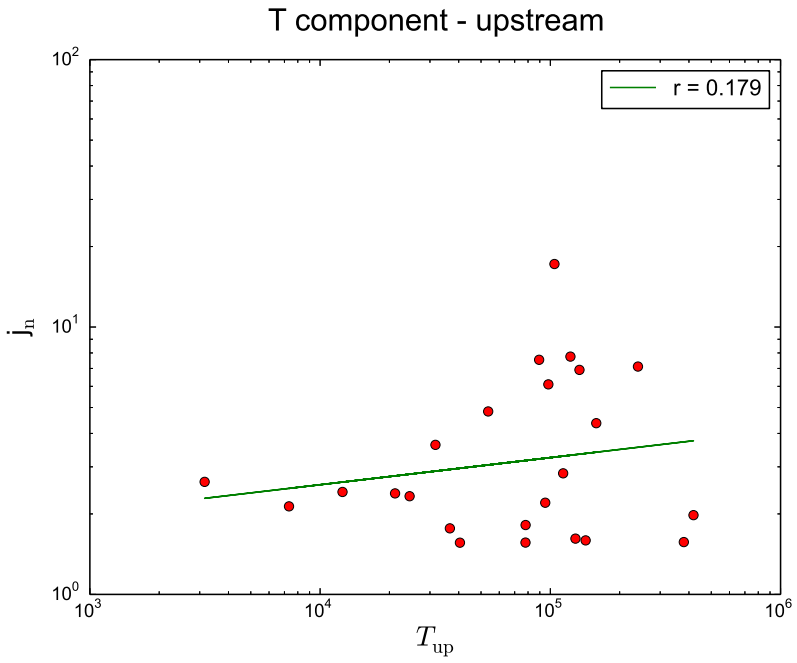

(a)

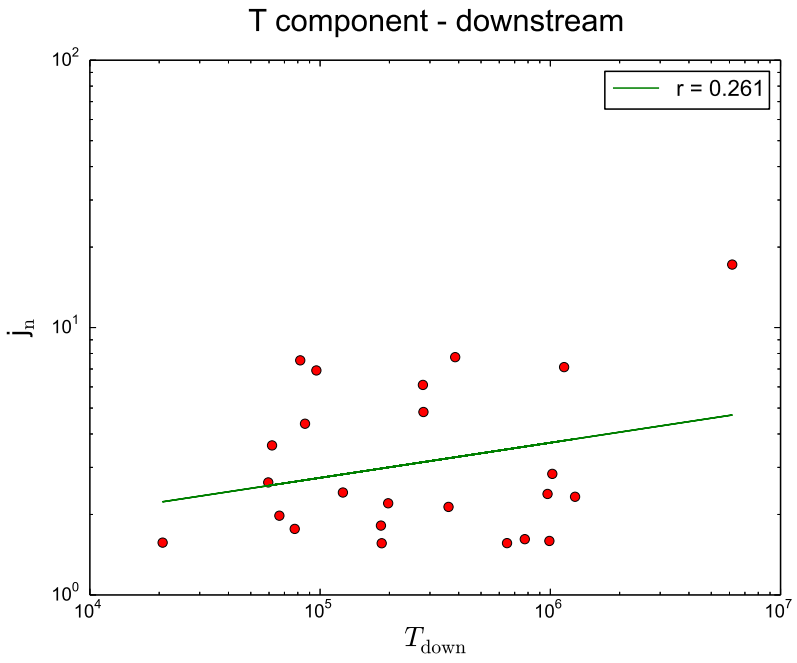

(b)

Figure 3.9: Proton flux enhancements in the $4-6$ MeV versus turbulence measure for the T component of the magnetic field for the shocks of the first list. Panel (a) shows the correlation in the upstream region of the shock while panel (b) in the downstream region. r is the correlation coefficient of the linear fit indicated by the green line.

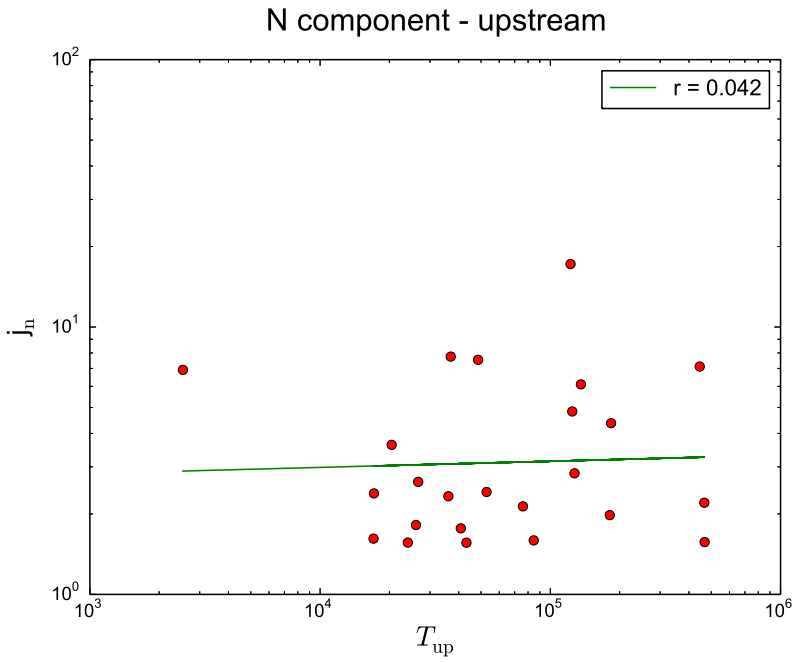

(a)

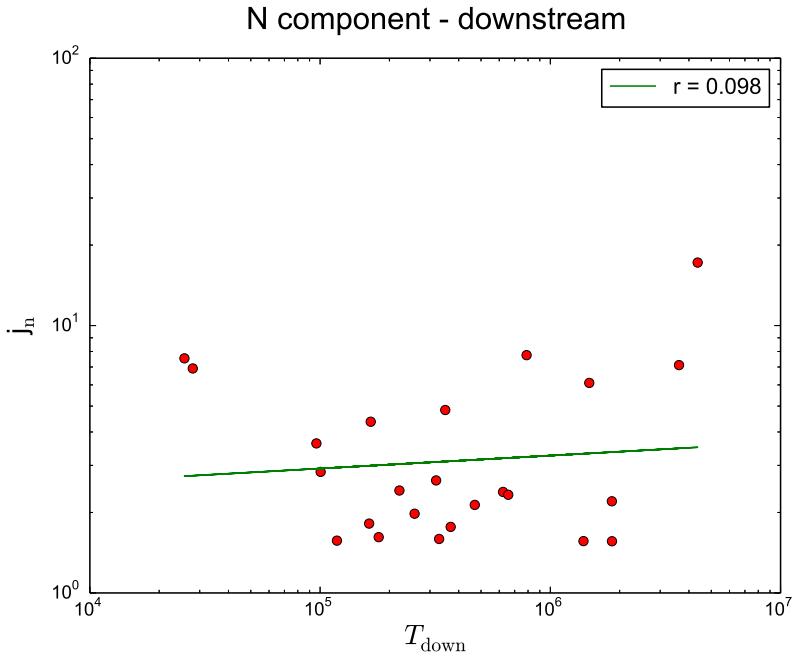

(b)

Figure 3.10: Proton flux enhancements in the $4-6$ MeV versus turbulence measure for the N component of the magnetic field for the shocks of the first list. Panel (a) shows the correlation in the upstream region of the shock while panel (b) in the downstream region. r is the correlation coefficient of the linear fit indicated by the green line.

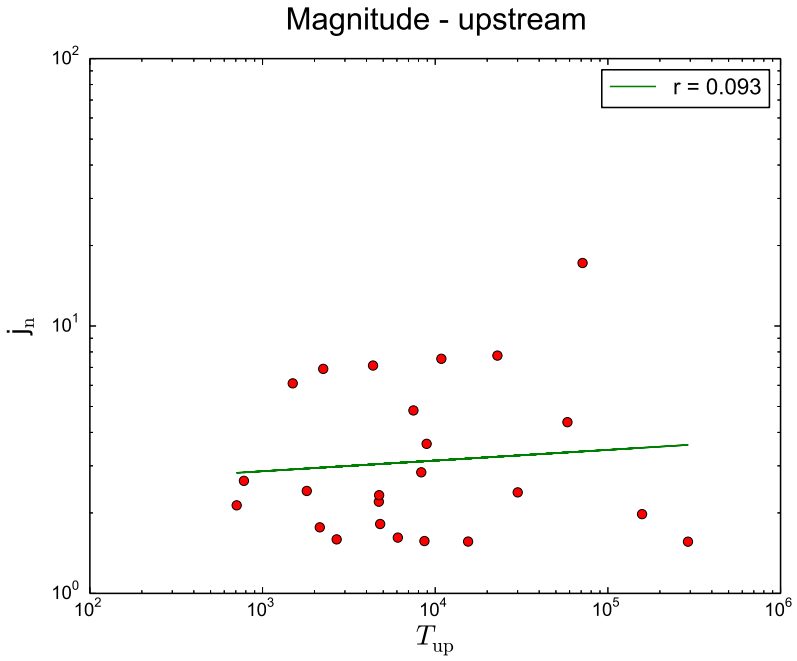

(a)

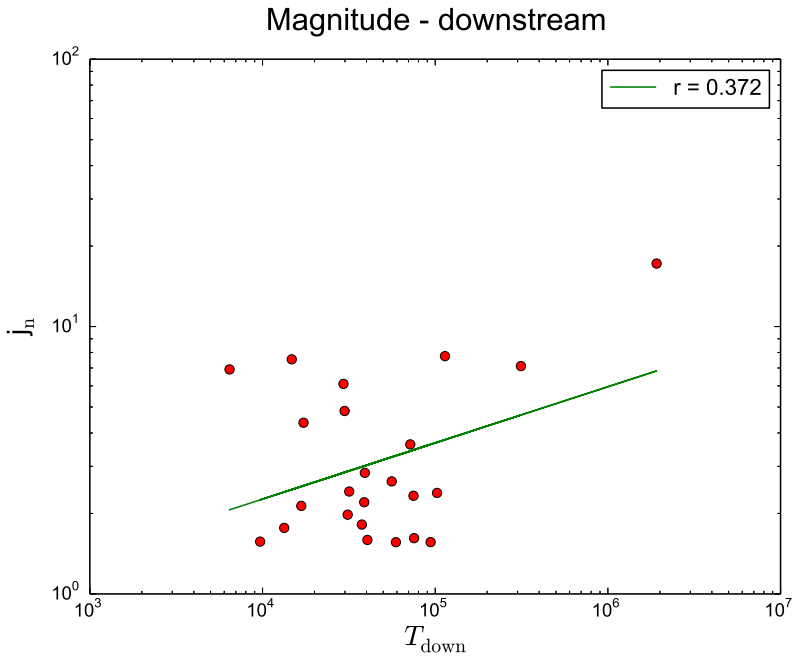

(b)

Figure 3.11: Proton flux enhancements in the $4-6$ MeV versus turbulence measure for the magnitude of the magnetic field for the shocks of the first list. Panel (a) shows the correlation in the upstream region of the shock while panel (b) in the downstream region. r is the correlation coefficient of the linear fit indicated by the green line.

Results for List 1: SEP events

Since the correlation coefficients obtained for all ESP events of List 1 are low, we separate the events that occur on the wake of a SEP event from those that are not associated with a SEP, in order to study the link between the two considered quantities for the two groups of events, separately. We report below the plots of the flux j_n as a function of the total wave power T relative to the shocks of the list 1 that occur in presence of SEP event in the upstream and downstream regions of the interplanetary shocks. We did this correlation analysis for the three components (R,T,N) and for magnitude of magnetic field and we got:

- higher correlations in the downstream region than the upstream region;
- for downstream region, higher correlations for the R and T components and magnitude than the N component of magnetic field.

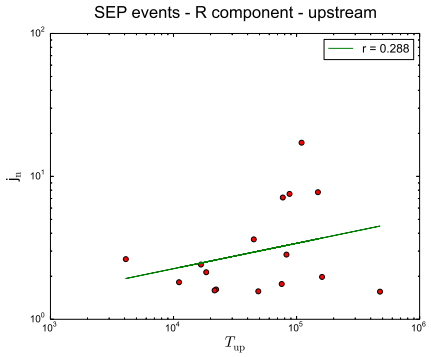

(a)

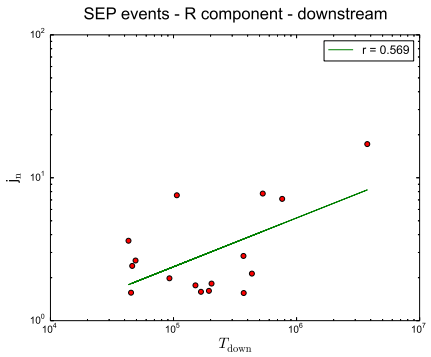

(b)

Figure 3.12: Proton flux enhancements in the $4-6$ MeV versus turbulence measure for the R component of the magnetic field for the shocks associated with SEP events. Panel (a) shows the correlation in the upstream region of the shock while panel (b) in the downstream region. r is the correlation coefficient of the linear fit indicated by the green line.

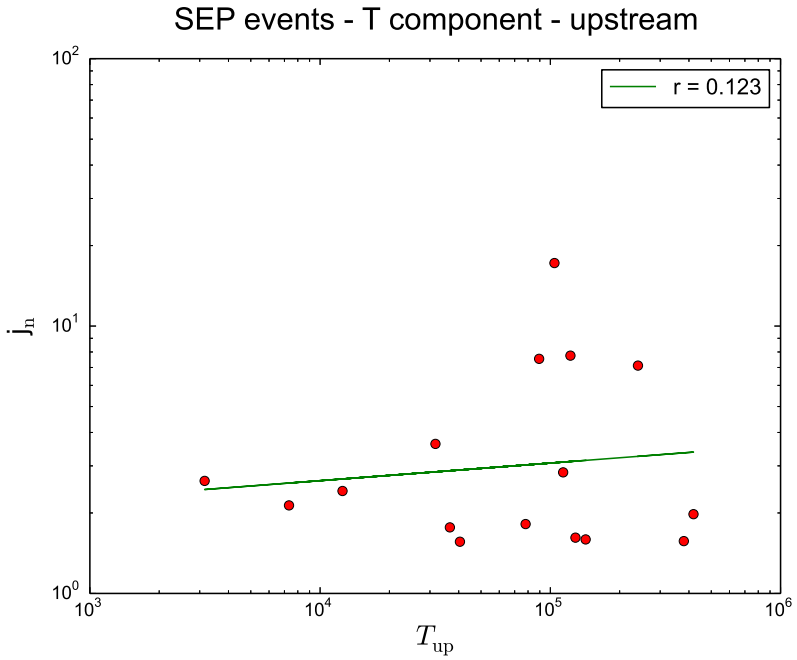

(a)

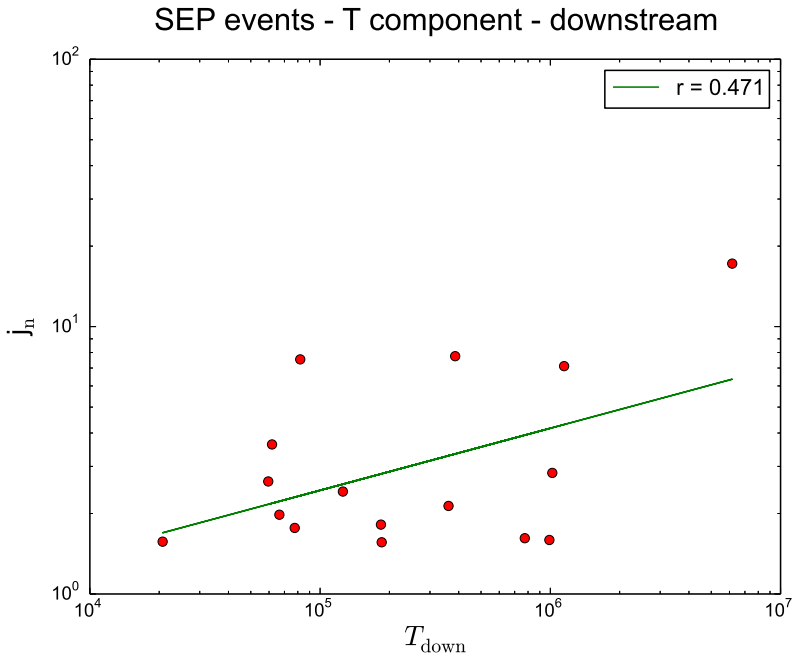

(b)

Figure 3.13: Proton flux enhancements in the $4-6$ MeV versus turbulence measure for the T component of the magnetic field for the shocks associated with SEP events. Panel (a) shows the correlation in the upstream region of the shock while panel (b) in the downstream region. r is the correlation coefficient of the linear fit indicated by the green line.

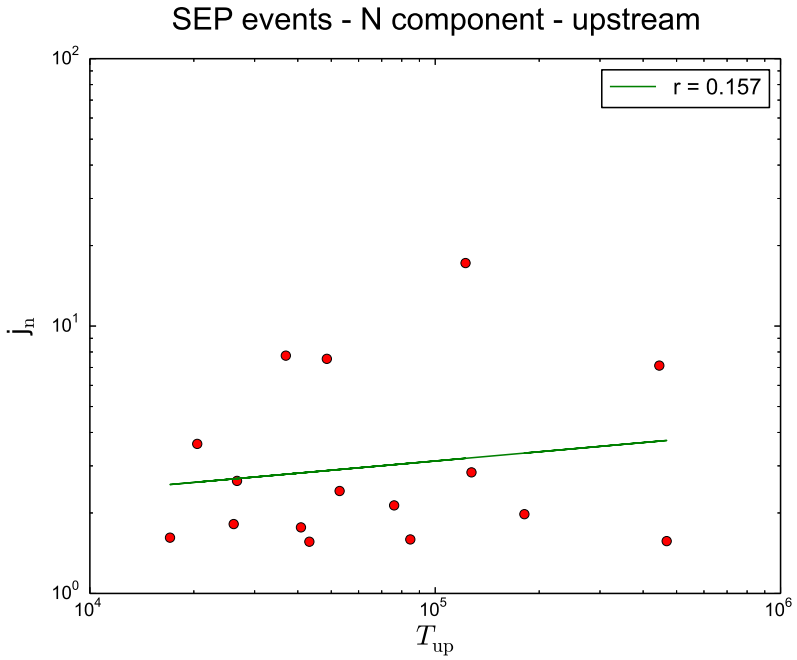

(a)

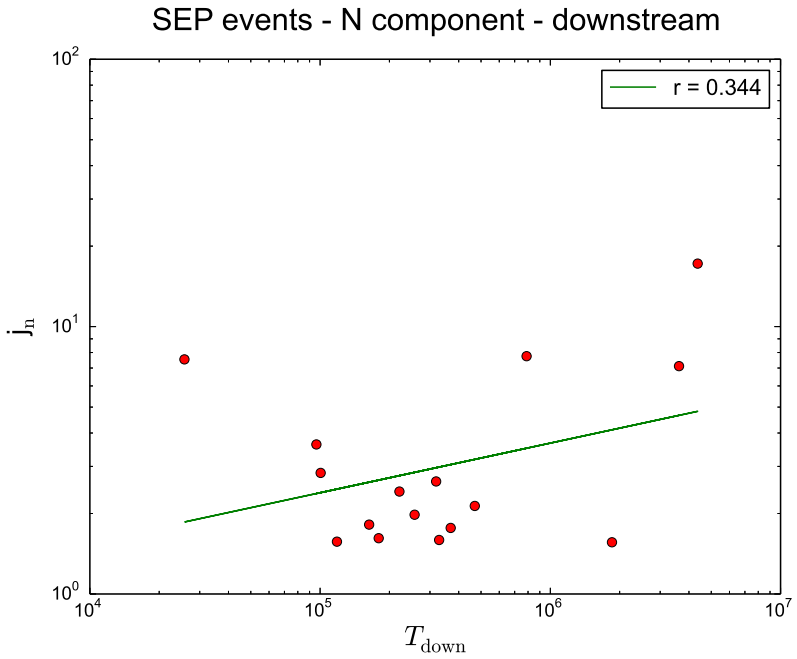

(b)

Figure 3.14: Proton flux enhancements in the $4-6$ MeV versus turbulence measure for the N component of the magnetic field for the shocks associated with SEP events. Panel (a) shows the correlation in the upstream region of the shock while panel (b) in the downstream region. r is the correlation coefficient of the linear fit indicated by the green line.

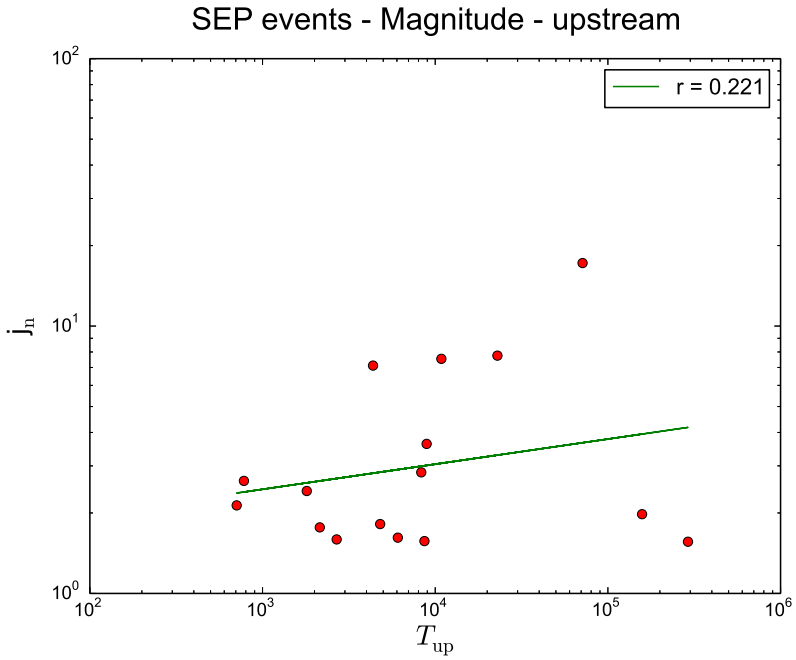

(a)

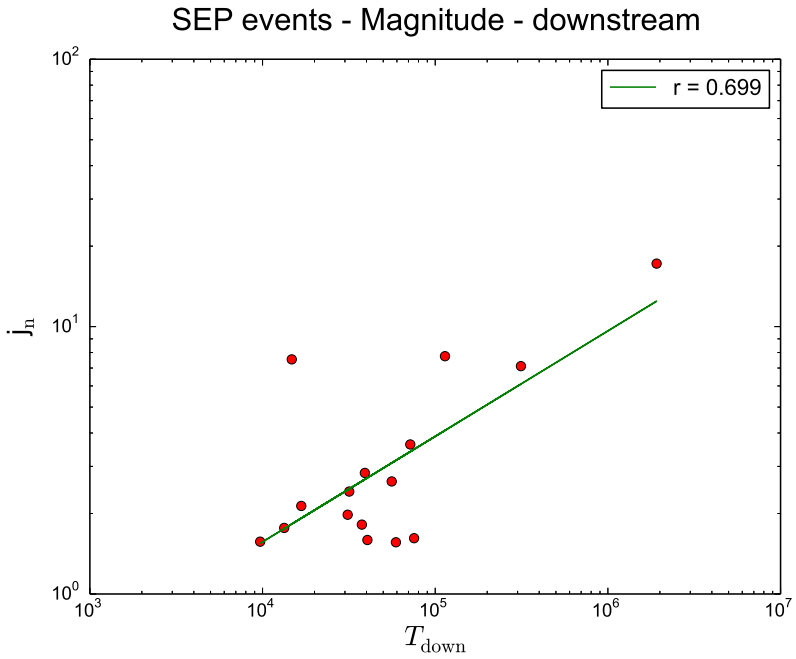

(b)

Figure 3.15: Proton flux enhancements in the $4-6$ MeV versus turbulence measure for the magnitude of the magnetic field for the shocks associated with SEP events. Panel (a) shows the correlation in the upstream region of the shock while panel (b) in the downstream region. r is the correlation coefficient of the linear fit indicated by the green line.

Results for List 1: NO SEP events

In the case of shocks that occur in absence of SEP events (NO SEP), we obtained the results shown below with the panel (a) relative to the correlation between the proton flux increases and the turbulence measure in the upstream region and the panel (b) related to the downstream region of the interplanetary shocks. Also in this case we have correlation coefficients greater than those obtained when all the events (SEP and NO SEP) are considered, even if we find clearly anti-correlation coefficients unlike the correlation values obtained in the case of shocks that occur on the wake of SEP events. In particular we got:

- anti-correlation for all the components and magnitude of the magnetic field downstream;
- higher coefficients in the downstream region than the upstream region;
- the only positive correlation is found fo the upstream T component.

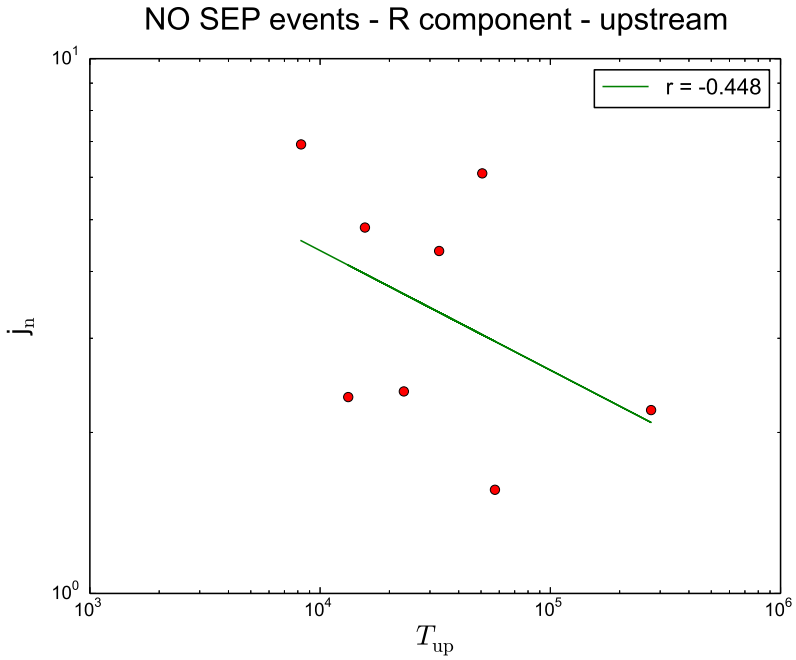

(a)

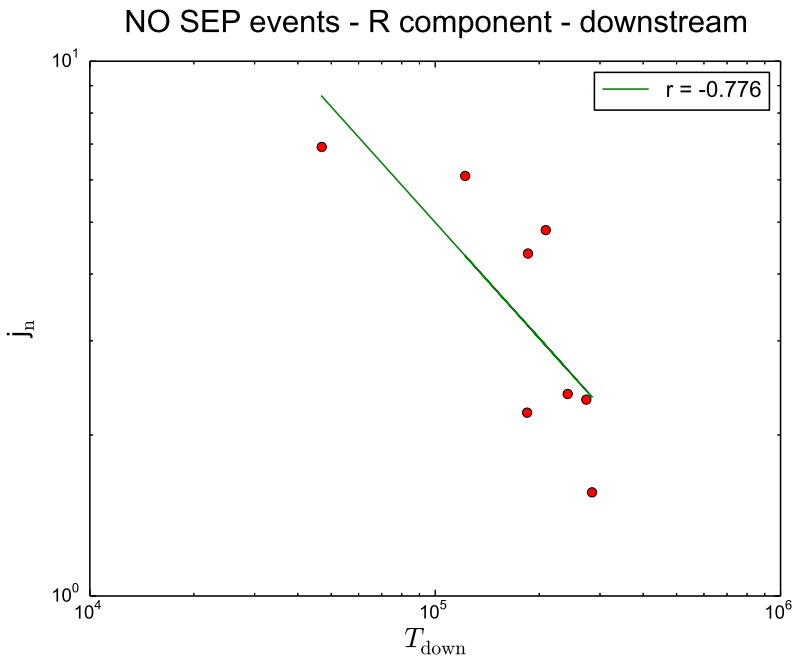

(b)

Figure 3.16: Proton flux enhancements in the $4-6$ MeV versus turbulence measure for the R component of the magnetic field for the shocks without the presence of a SEP event. Panel (a) shows the correlation in the upstream region of the shock while panel (b) in the downstream region. r is the correlation coefficient of the linear fit indicated by the green line.

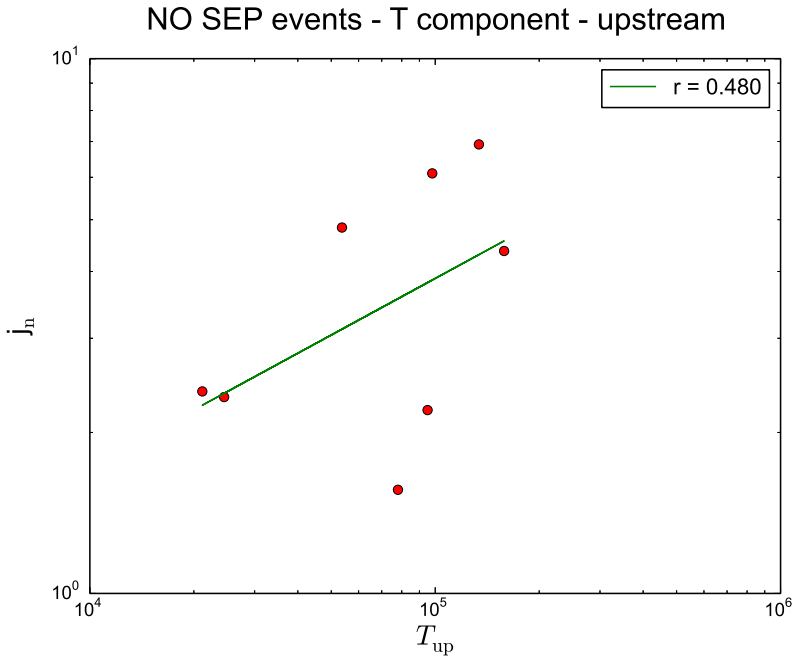

(a)

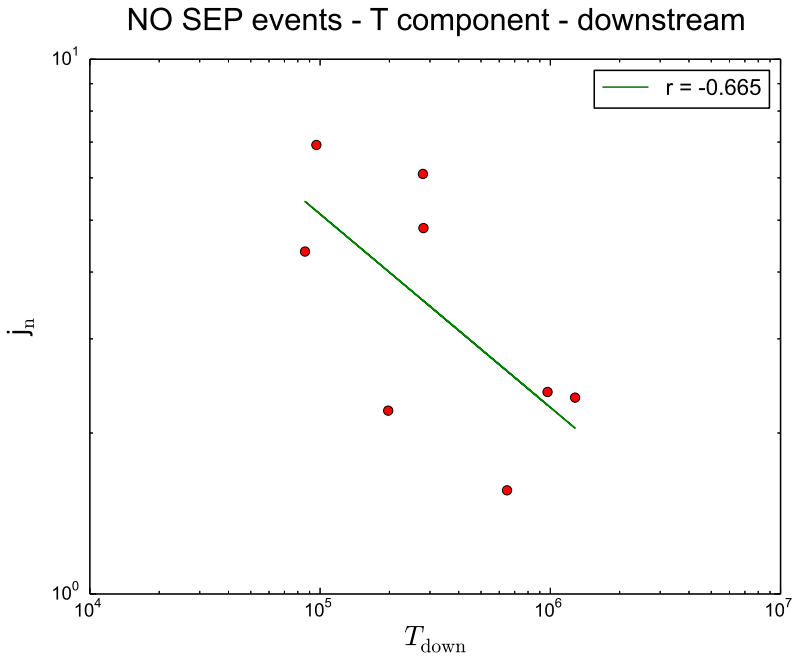

(b)

Figure 3.17: Proton flux enhancements in the $4-6$ MeV versus turbulence measure for the T component of the magnetic field for the shocks without the presence of a SEP event. Panel (a) shows the correlation in the upstream region of the shock while panel (b) in the downstream region. r is the correlation coefficient of the linear fit indicated by the green line.

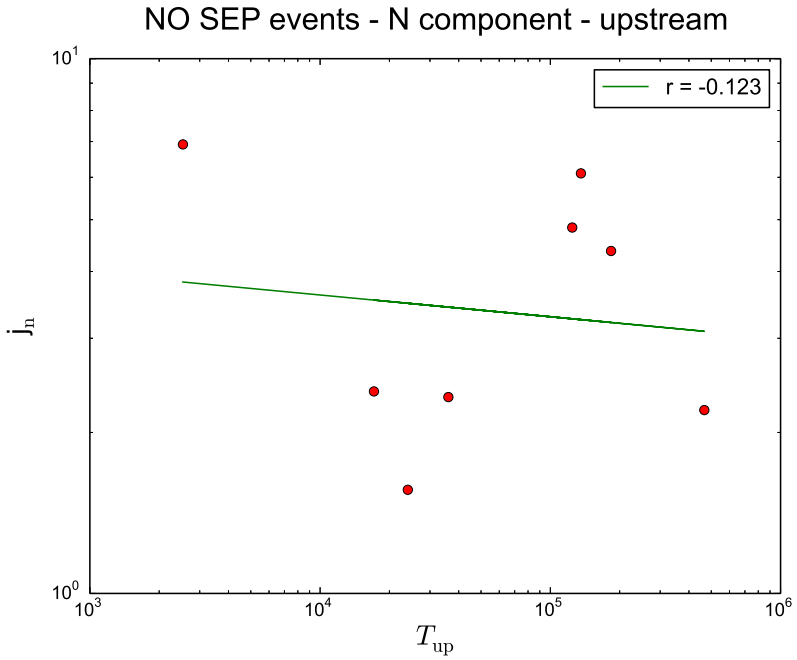

(a)

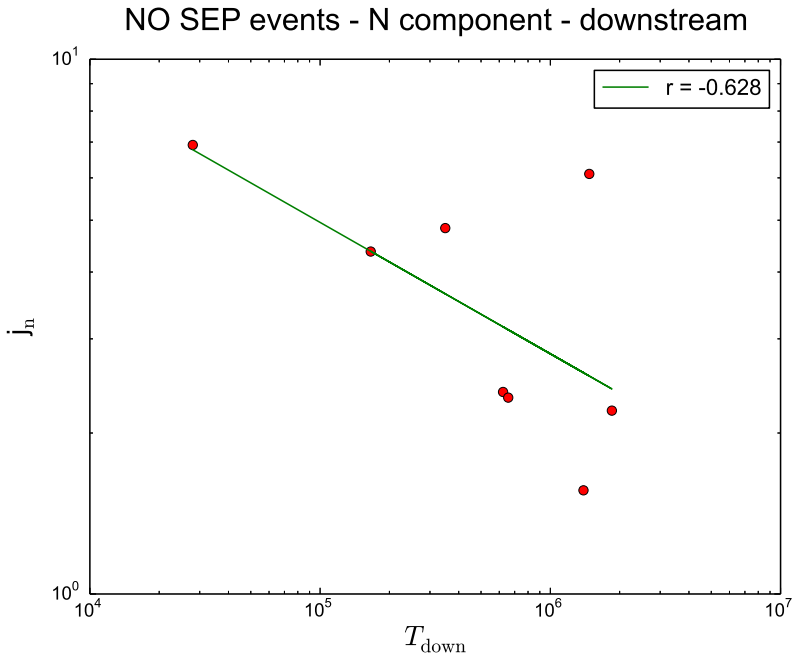

(b)

Figure 3.18: Proton flux enhancements in the $4-6$ MeV versus turbulence measure for the N component of the magnetic field for the shocks without the presence of a SEP event. Panel (a) shows the correlation in the upstream region of the shock while panel (b) in the downstream region. r is the correlation coefficient of the linear fit indicated by the green line.

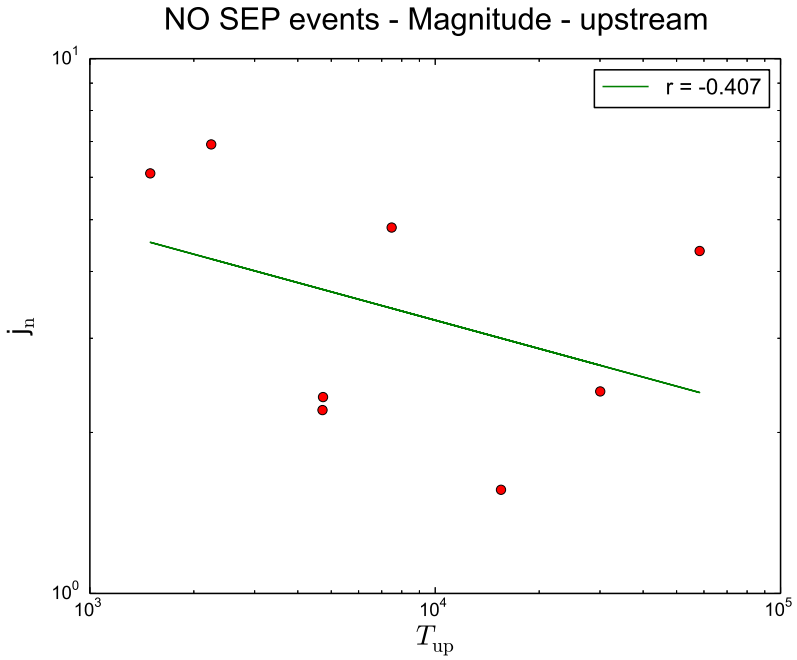

(a)

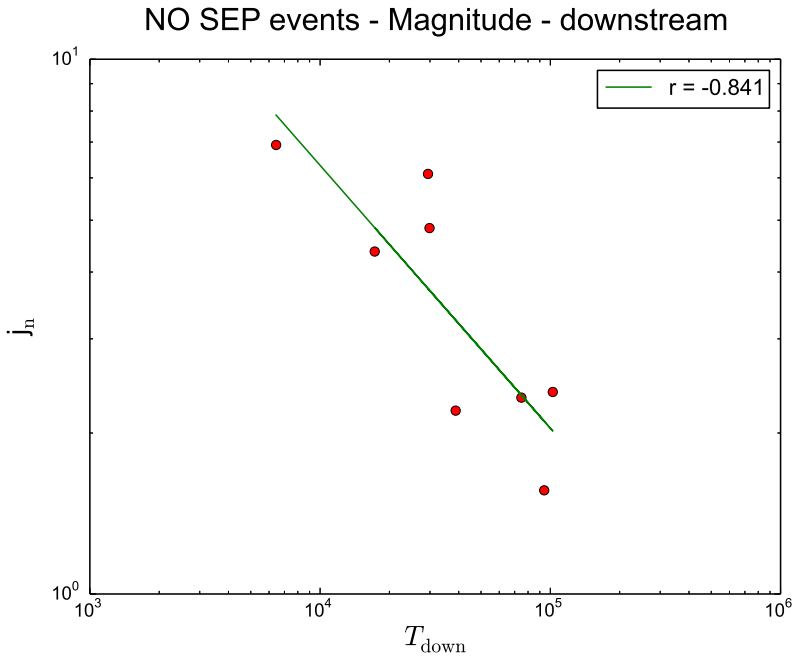

(b)

Figure 3.19: Proton flux enhancements in the $4-6$ MeV versus turbulence measure for the magnitude of the magnetic field for the shocks without the presence of a SEP event. Panel (a) shows the correlation in the upstream region of the shock while panel (b) in the downstream region. r is the correlation coefficient of the linear fit indicated by the green line.

Results for List 2

Then, we repeated the correlation analysis for the shocks belonging to List 2, which refers to the events that presented an increment in an interval greater than three hours before or after the shock passage time up to 15 hours. For each component and for the magnitude of the magnetic field the top plot shows the proton flux enhancements j_n as a function of the turbulence measure T in the upstream region while the plot below displays the same quantities in the downstream region of the shocks. Also for the second list we made a parametric and a nonparametric correlation analysis whose results are shown later. In the case of list 2, we do not consider an event that present an high value of j_n (shock #8 of the list 2) that is an outlier point. We find:

- poor correlation in the upstream and downstream regions of interplanetary shocks;
- for downstream region, coefficients slightly higher for the R and T components and magnitude of the magnetic field.

Therefore, due to the lower number of events compared to those of list 1, we will not divide the events in SEP and NO SEP.

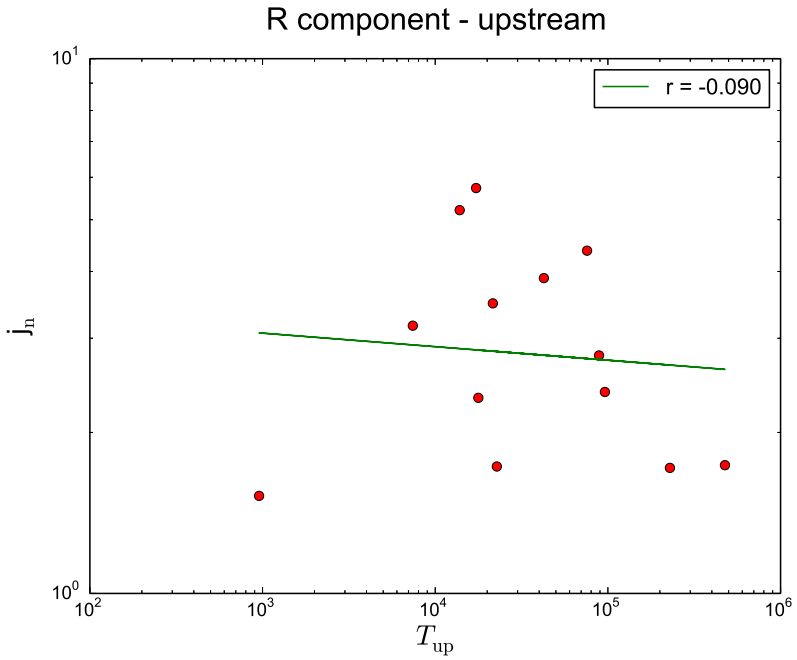

(a)

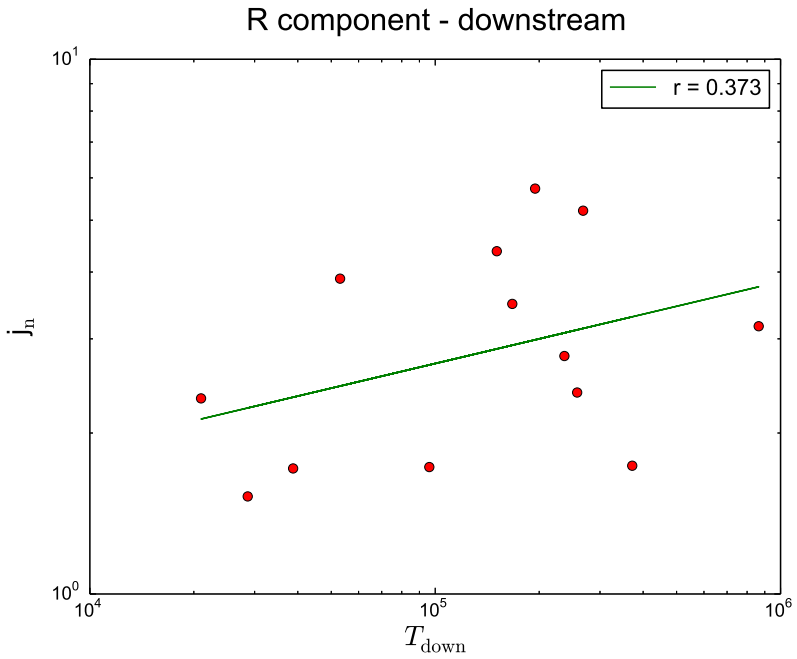

(b)

Figure 3.20: Proton flux enhancements in the $4-6$ MeV versus turbulence measure for the R component of the magnetic field for the shocks of the second list. Panel (a) shows the correlation in the upstream region of the shock while panel (b) in the downstream region. r is the correlation coefficient of the linear fit indicated by the green line.

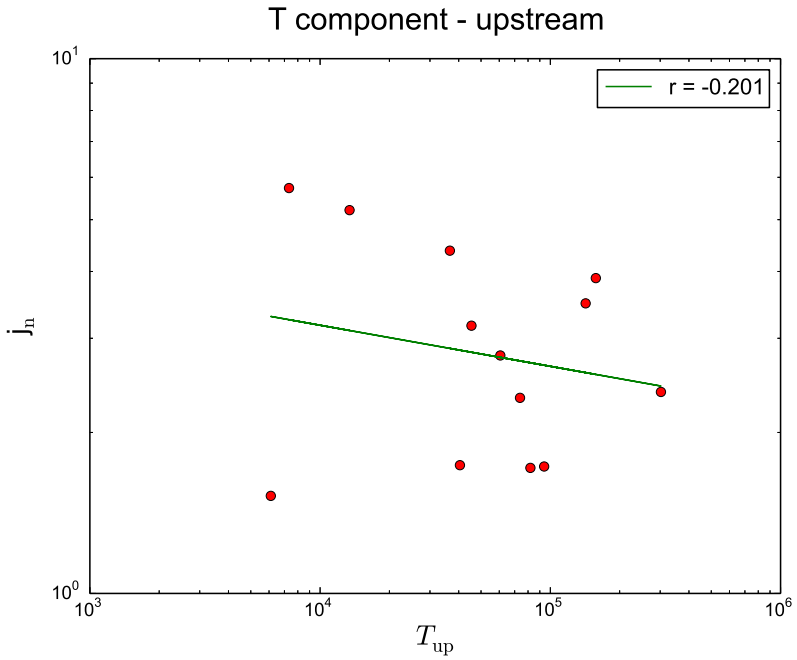

(a)

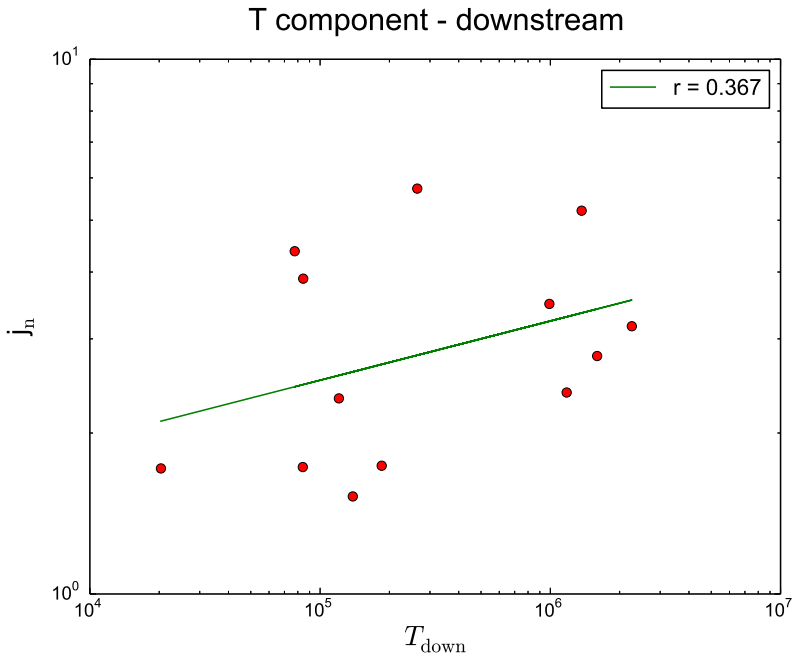

(b)

Figure 3.21: Proton flux enhancements in the $4-6$ MeV versus turbulence measure for the T component of the magnetic field for the shocks of the second list. Panel (a) shows the correlation in the upstream region of the shock while panel (b) in the downstream region. r is the correlation coefficient of the linear fit indicated by the green line.

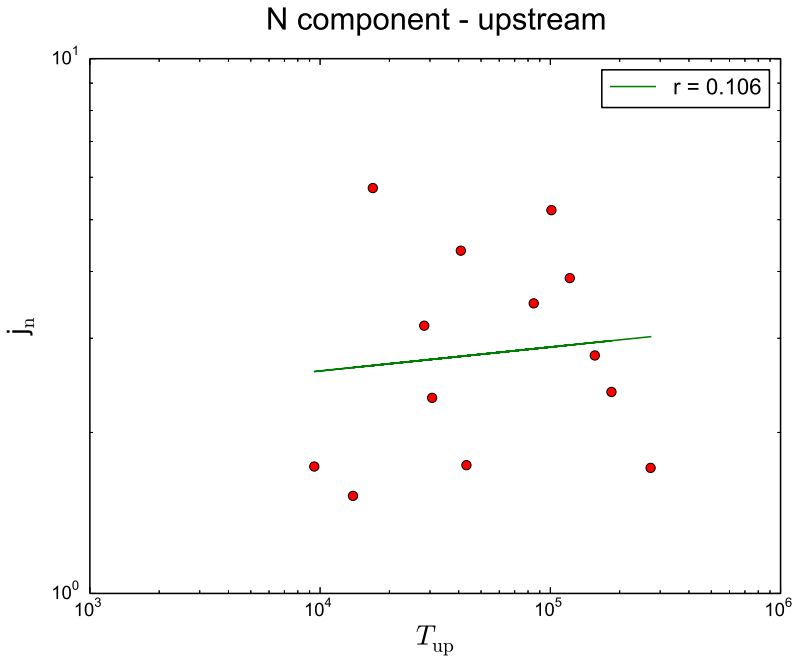

(a)

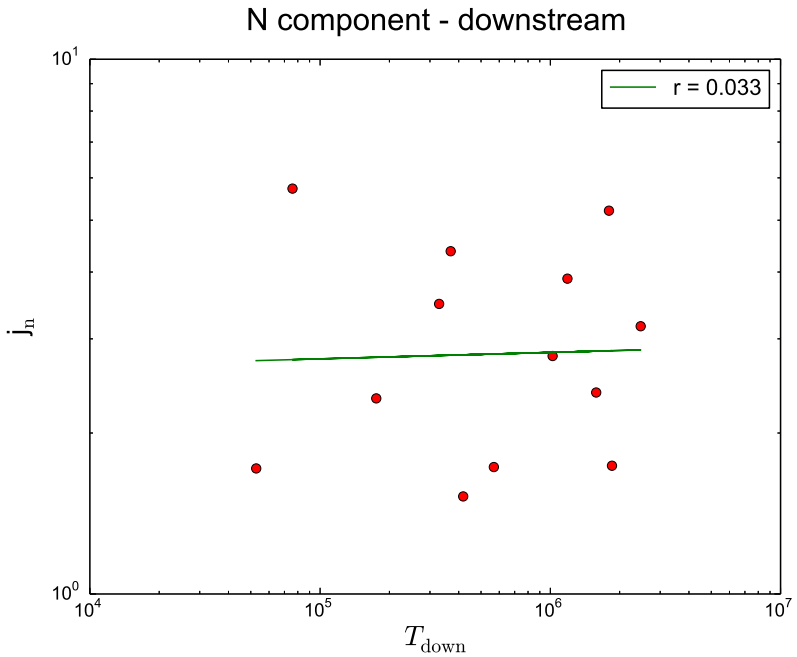

(b)

Figure 3.22: Proton flux enhancements in the $4-6$ MeV versus turbulence measure for the N component of the magnetic field for the shocks of the second list. Panel (a) shows the correlation in the upstream region of the shock while panel (b) in the downstream region. r is the correlation coefficient of the linear fit indicated by the green line.

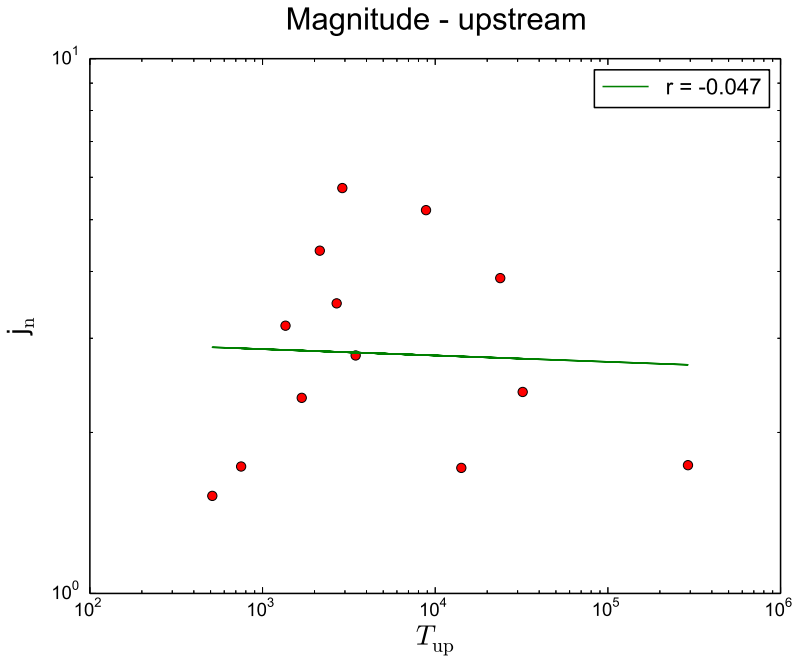

(a)

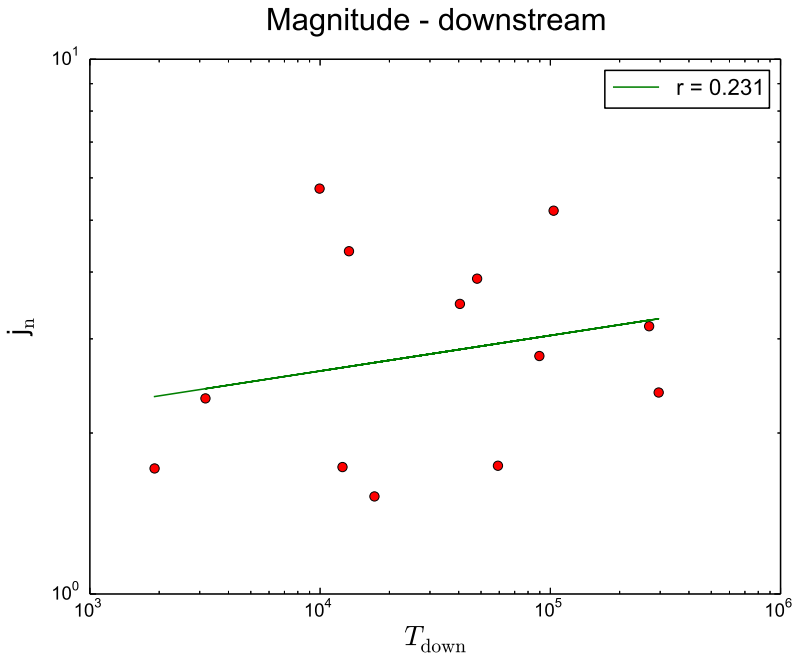

(b)

Figure 3.23: Proton flux enhancements in the $4-6$ MeV versus turbulence measure for the magnitude of the magnetic field for the shocks of the second list. Panel (a) shows the correlation in the upstream region of the shock while panel (b) in the downstream region. r is the correlation coefficient of the linear fit indicated by the green line.

3.3.2 Analysis of the correlation between proton flux enhancements and magnetic field fluctuations

In this section we analyze the correlation significance between the energetic proton flux enhancements and the magnetic field turbulence observed in the upstream and downstream regions of interplanetary shocks.
Table 3.3 shows the correlation coefficients (r) and the p-values (probability of occurrence by chance) for the shocks belonging to the List 1 while table 3.4 shows the same for List 2.

List 1 - Linear correlation

UP		DOWN	
r^R= 0.092	p^R= 0.669	r^R= 0.365	p^R= 0.079
r^T= 0.179	p^T= 0.402	r^T= 0.261	p^T= 0.217
r^N= 0.042	p^N= 0.845	r^N= 0.098	p^N= 0.648
r= 0.093	p= 0.665	r= 0.372	p= 0.073

(a) List 1

UP		DOWN	
r^R= 0.288	p^R= 0.279	r^R= 0.569	p^R= 0.021
r^T= 0.123	p^T= 0.650	r^T= 0.471	p^T= 0.066
r^N= 0.157	p^N= 0.562	r^N= 0.344	p^N= 0.192
r= 0.221	p= 0.410	r= 0.699	p= 0.003

(b) List 1: SEP

UP		DOWN	
r^R= −0.448	p^R= 0.266	r^R= −0.776	p^R= 0.024
r^T= 0.480	p^T= 0.229	r^T= −0.665	p^T= 0.072
r^N= −0.123	p^N= 0.771	r^N= −0.628	p^N= 0.095
r= −0.407	p= 0.317	r= −0.841	p= 0.009

(c) List 1: NO SEP

Table 3.3: Table (a) contains the correlation coefficients and the p-values related to the shocks reported in the List 1, in the upstream and downstream regions. Table (b) refers to the shocks associated with SEP events while table (c) to those that occur in the absence of SEP (NO SEP).

List 2 - Linear correlation

UP		DOWN	
$r^R = -0.090$	$p^R = 0.770$	$r^R = 0.373$	$p^R = 0.209$
$r^T = -0.201$	$p^T = 0.510$	$r^T = 0.367$	$p^T = 0.218$
$r^N = 0.106$	$p^N = 0.730$	$r^N = 0.033$	$p^N = 0.914$
$r = -0.047$	$p = 0.880$	$r = 0.231$	$p = 0.447$

Table 3.4: Correlation coefficients and the p-values related to the shocks reported in the List 2, in the upstream and downstream regions.

In addition to the parametric correlation analysis performed by calculating the linear correlation coefficient (r), we make a nonparametric correlation analysis, through the Spearman's correlation coefficient (ρ_s). It estimates how well the relationship between two variables, in our case the proton flux enhancement and the turbulence measure, can be described using a monotonic function. We performed this statistical analysis for the three components (R, T, N) and for the magnitude of the magnetic field relative to the events belonging to the list 1 (see table 3.5) and then, we repeated the analysis for the list 2 (see table 3.6). In each table, next to each Spearman's coefficient we reported the significance (p) of its deviation from zero. The significance is a value in the interval $[0.0, 1.0]$; a small value indicates a significant correlation.

List 1 - Spearman's correlation

UP		DOWN	
$\rho_s^R = 0.039$	$p^R = 0.856$	$\rho_s^R = 0.113$	$p^R = 0.599$
$\rho_s^T = 0.096$	$p^T = 0.657$	$\rho_s^T = 0.139$	$p^T = 0.517$
$\rho_s^N = 0.102$	$p^N = 0.636$	$\rho_s^N = -0.009$	$p^N = 0.968$
$\rho = 0.003$	$p = 0.987$	$\rho = 0.090$	$p = 0.674$

(a) List 1

UP		DOWN	
$\rho_s^R = 0.197$	$p^R = 0.464$	$\rho_s^R = 0.291$	$p^R = 0.274$
$\rho_s^T = -0.118$	$p^T = 0.664$	$\rho_s^T = 0.282$	$p^T = 0.289$
$\rho_s^N = 0.024$	$p^N = 0.931$	$\rho_s^N = 0.079$	$p^N = 0.770$
$\rho = 0.132$	$p = 0.625$	$\rho = 0.424$	$p = 0.102$

(b) List 1: SEP

UP		DOWN	
$\rho_s^R = -0.571$	$p^R = 0.139$	$\rho_s^R = -0.738$	$p^R = 0.037$
$\rho_s^T = 0.429$	$p^T = 0.289$	$\rho_s^T = -0.452$	$p^T = 0.260$
$\rho_s^N = -0.190$	$p^N = 0.651$	$\rho_s^N = -0.571$	$p^N = 0.139$
$\rho = -0.405$	$p = 0.320$	$\rho = -0.762$	$p = 0.028$

(c) List 1: NO SEP

Table 3.5: Table (a) contains the Spearman's coefficient correlation and its significance related to the shocks reported in the List 1, in the upstream and downstream regions. Table (b) refers to the shocks associated with SEP events while table (c) to those that occur in the absence of SEP (NO SEP).

List 2 - Spearman's correlation

UP		DOWN	
$\rho_s^R = -0.174$	$p^R = 0.553$	$\rho_s^R = 0.112$	$p^R = 0.703$
$\rho_s^T = 0.042$	$p^T = 0.887$	$\rho_s^T = 0.064$	$p^T = 0.829$
$\rho_s^N = 0.033$	$p^N = 0.911$	$\rho_s^N = -0.138$	$p^N = 0.637$
$\rho = 0.191$	$p = 0.513$	$\rho = -0.015$	$p = 0.958$

Table 3.6: Spearman's coefficient correlation and its significance related to the shocks reported in the List 2, in the upstream and downstream regions.

Overall, we have noticed that there is a good correlation between the measure of turbulence downstream and the flux of particles, and a poor correlation between upstream turbulence and particle fluxes (Claßen et al., 1999). At this point, if we choose as the threshold value 0.1 for the p-value in the case of the linear correlation and for the significance in the case of the nonparamet-

ric correlation through the Spearman's coefficient, we obtain a not significant correlation for all events in List 1.
To evaluate the level of correlation in the various cases of the List 1, we have separated the shocks that occur on the wake of a SEP event from those where a SEP is not present at the shock passage (NO SEP). In particular, as we can see from the table 3.3b, we found a not significant correlation between the upstream magnetic field turbulence and the particle fluxes, whereas a high correlation between these quantities in the downstream region, except for the N component that is not significant. In the case of Spearman's correlation (see table 3.5b) we obtain a not significant correlation coefficients upstream and downstream, but they become in agreement with those obtained from the parametric analysis if we increase the threshold value for the significance to 0.3. On the other hand, in absence of a solar energetic particle event in correspondence of the shock passage (see table 3.3c), we obtained a significant anticorrelation in the downstream region; also in this case if we consider a threshold of 0.3 for the significance the agreement with the linear correlation increases (see table 3.5c). We obtain a correlation for SEP events and an anticorrelation for NO SEP events, probably due to the influence of the streaming of solar energetic particles at the shock. On the contrary, for the shocks recorded in the List 2, we got a not significant correlation between the magnetic field turbulence and the particles fluxes in the upstream and downstream regions of interplanetary shock (see table 3.4 or 3.6).
We discuss the results obtained in this section in the frame of particle acceleration processes, focusing on the role played by the magnetic turbulence.

3.3.3 Analysis of the compressibility degree

We consider now also the degree of compressibility in the upstream and downstream regions of interplanetary shocks of the two lists of selected events (see tables 3.1 and 3.2).
In the interplanetary medium magnetic field and density show fluctuations over all scales and the compression depends on both the scale and the nature of the solar wind. In fact, slow wind is generally more compressive than fast wind. Bavassano et al. (1982) used a variance analysis of Helios-2 magnetic data to investigate statistical properties of incompressible fluctuations (eigenvalues and eigenvectors of the variance matrix of the fluctuating components) associated with the trailing edge of the high-speed streams. They found that the turbulence is not strictly incompressible and compressibility is relatively more important away from the Sun.

In order to study the degree of compressibility of the fluctuations associated with the proton flux enhancements, we used the quantity σ_B^2/B^2, where σ_B^2 is the variance in field magnitude and B is the average of the magnetic field magnitude.
In particular, we analyzed the degree of compressibility for all the ESP events of the first list, for the shocks that occur on the wake of an SEP event and in the case of NO SEP events. We report in figures 3.24, 3.25 and 3.26 the correlation analysis performed on the magnetic field magnitude that show a correlation coefficient in the downstream region of interplanetary shocks greater than the coefficient in the upstream region. We repeated this study also for the three components of the magnetic field and we obtained similar results in all cases (the correlation coefficients and the p-values are recorded in table 3.7). If we choose as the threshold value for the p-value 0.1, we obtain a not significant correlation for all events in List 1, except for the magnitude of the magnetic field in the downstream region in the case of SEP and NO SEP events, separately.
In addition to the parametric correlation analysis performed by calculating the linear correlation coefficient (r), we make a nonparametric correlation analysis, through the Spearman's correlation coefficient (ρ_s), whose results are reported in table 3.8. In the case of Spearman's coefficient, if we choose 0.1 as the threshold value for the significance, we only obtain a significant anti-correlation for the magnitude in the downstream region for NO SEP events.

List 1 - Linear correlation

UP		DOWN	
$r^R = 0.160$	$p^R = 0.455$	$r^R = 0.199$	$p^R = 0.351$
$r^T = 0.051$	$p^T = 0.813$	$r^T = 0.210$	$p^T = 0.324$
$r^N = 0.024$	$p^N = 0.911$	$r^N = -0.096$	$p^N = 0.657$
$r = 0.053$	$p = 0.806$	$r = 0.266$	$p = 0.209$

(a) List 1

UP		DOWN	
$r^R = 0.384$	$p^R = 0.142$	$r^R = 0.311$	$p^R = 0.241$
$r^T = -0.018$	$p^T = 0.949$	$r^T = 0.241$	$p^T = 0.368$
$r^N = 0.019$	$p^N = 0.944$	$r^N = 0.009$	$p^N = 0.974$
$r = 0.125$	$p = 0.644$	$r = 0.493$	$p = 0.052$

(b) List 1: SEP

UP		DOWN	
$r^R = -0.340$	$p^R = 0.327$	$r^R = -0.418$	$p^R = 0.302$
$r^T = 0.185$	$p^T = 0.660$	$r^T = 0.027$	$p^T = 0.949$
$r^N = 0.067$	$p^N = 0.875$	$r^N = -0.455$	$p^R = 0.257$
$r = -0.280$	$p = 0.502$	$r = -0.627$	$p = 0.096$

(c) List 1: NO SEP

Table 3.7: Table (a) contains the correlation coefficients and the p-values related to the shocks reported in the List 1 between the proton flux enhancements and the degree of compressibility in the upstream and downstream regions. Table (b) refers to the shocks associated with SEP events while table (c) to those that occur in the absence of SEP (NO SEP).

List 1 - Spearman's correlation

UP		DOWN	
$\rho_s^R = -0.080$	$p^R = 0.710$	$\rho_s^R = 0.021$	$p^R = 0.923$
$\rho_s^T = -0.126$	$p^T = 0.557$	$\rho_s^T = 0.178$	$p^T = 0.405$
$\rho_s^N = 0.119$	$p^N = 0.579$	$\rho_s^N = -0.223$	$p^N = 0.296$
$\rho = -0.095$	$p = 0.659$	$\rho = 0.123$	$p = 0.565$

(a) List 1

UP		DOWN	
$\rho_s^R = 0.000$	$p^R = 1.000$	$\rho_s^R = 0.159$	$p^R = 0.557$
$\rho_s^T = -0.165$	$p^T = 0.542$	$\rho_s^T = 0.191$	$p^T = 0.478$
$\rho_s^N = 0.100$	$p^N = 0.713$	$\rho_s^N = -0.241$	$p^N = 0.368$
$\rho = -0.109$	$p = 0.688$	$\rho = 0.329$	$p = 0.213$

(b) List 1: SEP

UP		DOWN	
$\rho_s^R = -0.574$	$p^R = 0.183$	$\rho_s^R = -0.381$	$p^R = 0.352$
$\rho_s^T = 0.095$	$p^T = 0.823$	$\rho_s^T = 0.190$	$p^T = 0.651$
$\rho_s^N = -0.048$	$p^N = 0.911$	$\rho_s^N = -0.452$	$p^N = 0.260$
$\rho = -0.238$	$p = 0.570$	$\rho = -0.762$	$p = 0.028$

(c) List 1: NO SEP

Table 3.8: Table (a) contains the Spearman's coefficient correlation and its significance related to the shocks reported in the List 1, in the upstream and downstream regions. Table (b) refers to the shocks associated with SEP events while table (c) to those that occur in the absence of SEP (NO SEP).

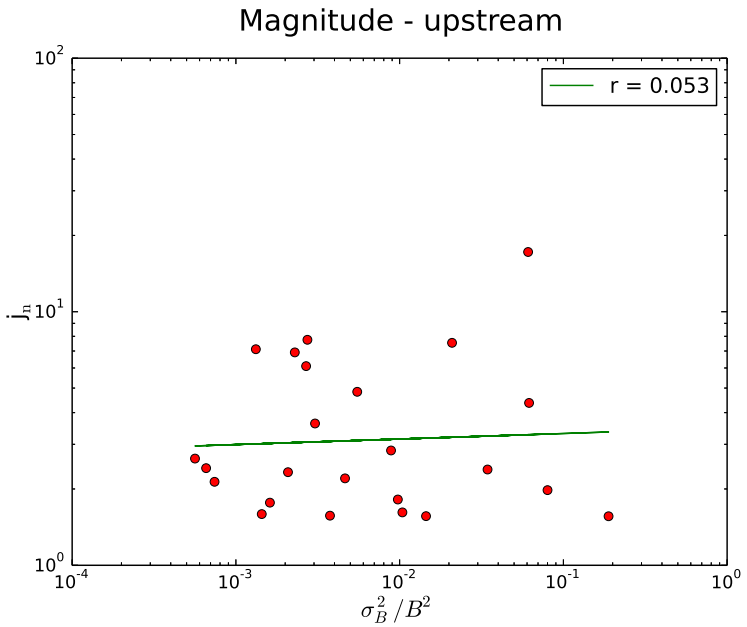

(a)

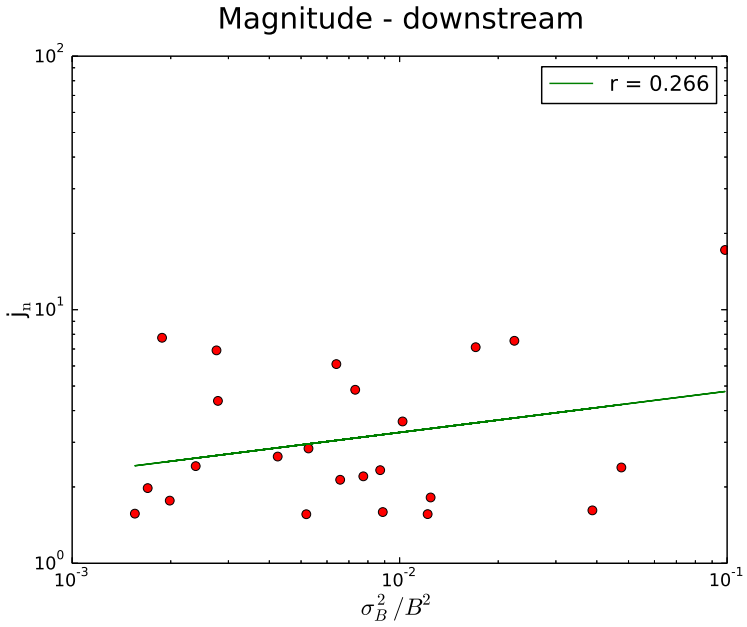

(b)

Figure 3.24: Proton flux enhancements versus degree of compressibility for the magnitude of the magnetic field for all the events of List 1. Panel (a) shows the correlation in the upstream region of the shock while panel (b) in the downstream region. r is the correlation coefficient of the linear fit indicated by the green line.

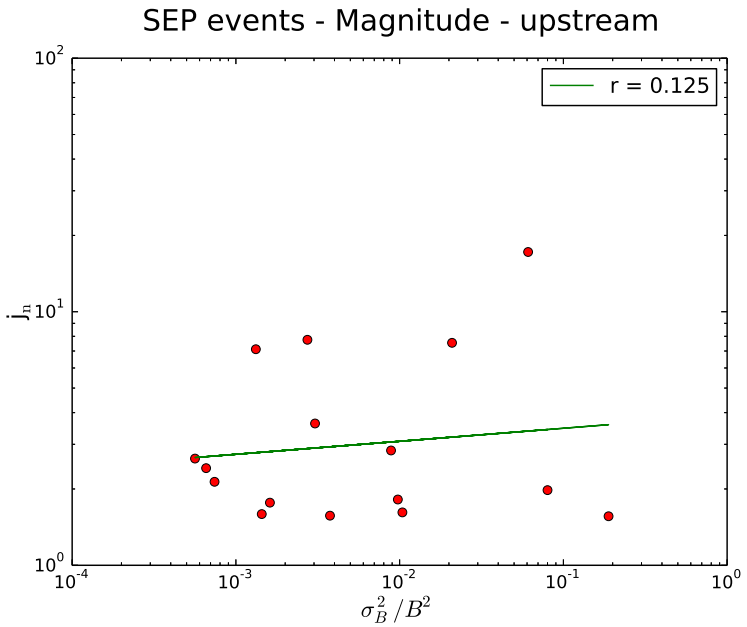

(a)

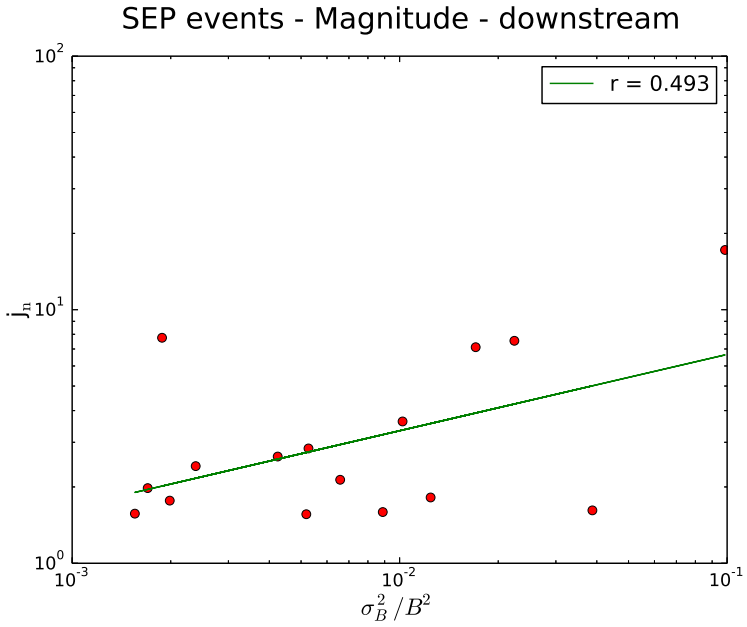

(b)

Figure 3.25: Proton flux enhancements versus degree of compressibility for the magnitude of the magnetic field for the shocks associated with SEP events. Panel (a) shows the correlation in the upstream region of the shock while panel (b) in the downstream region. r is the correlation coefficient of the linear fit indicated by the green line.

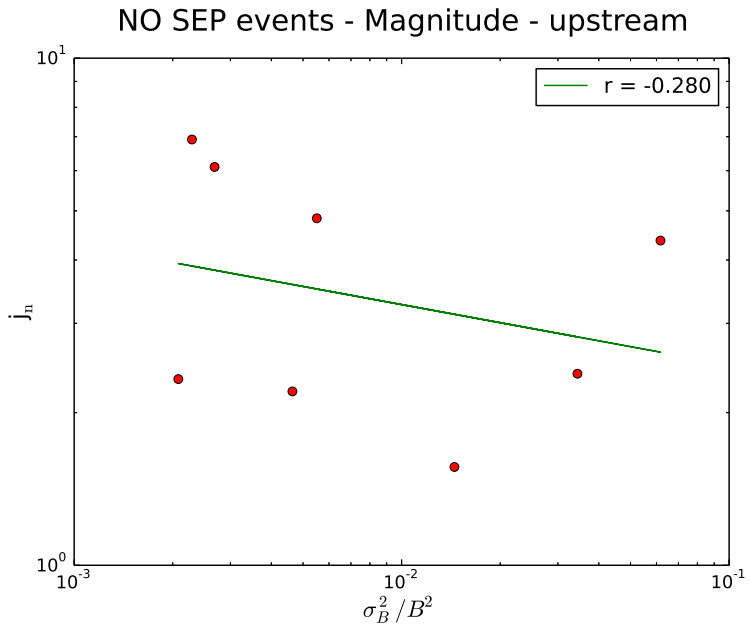

(a)

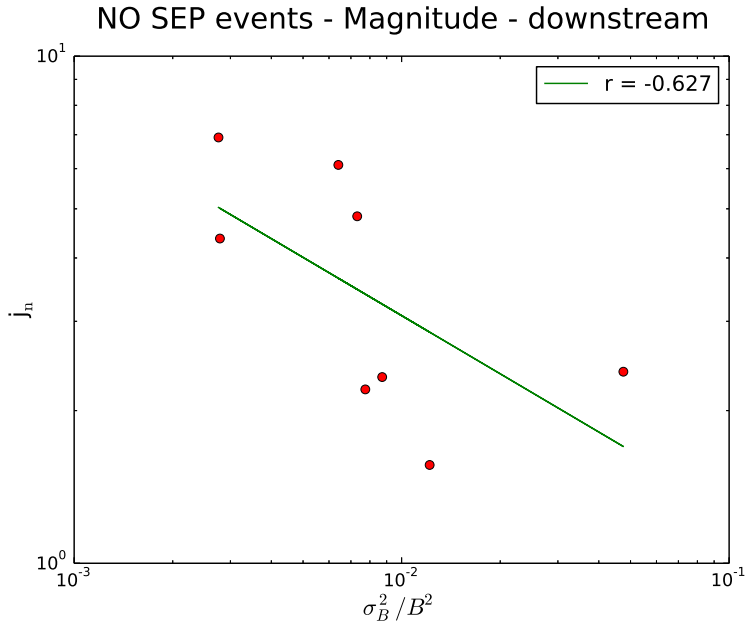

(b)

Figure 3.26: Proton flux enhancements versus degree of compressibility for the magnitude of the magnetic field for the shocks without the presence of a SEP event. Panel (a) shows the correlation in the upstream region of the shock while panel (b) in the downstream region. r is the correlation coefficient of the linear fit indicated by the green line.

Therefore, we applied the same analysis described above on the degree of compressibility to the shocks belonging to the second list (with the increment of the proton flux in an interval greater than three hours before or after the shock passage). Also in this case we show in figure 3.27 the correlation related to the magnitude of the magnetic field, even if all the components present such behavior. However, the results obtained with the parametric and non-parametric analysis (see tables 3.9 and 3.10), show not significant correlations in the upstream and downstream regions.

List 2 - Linear correlation

UP		DOWN	
$r^R = -0.090$	$p^R = 0.770$	$r^R = 0.373$	$p^R = 0.209$
$r^T = -0.201$	$p^T = 0.510$	$r^T = 0.367$	$p^T = 0.218$
$r^N = 0.106$	$p^N = 0.730$	$r^N = 0.033$	$p^N = 0.914$
$r = -0.047$	$p = 0.880$	$r = 0.231$	$p = 0.447$

Table 3.9: Correlation coefficients and the p-values between the proton flux enhancements and the degree of compressibility in the upstream and downstream regions related to the shocks reported in the List 2.

List 2 - Spearman's correlation

UP		DOWN	
$r^R = -0.090$	$p^R = 0.770$	$r^R = 0.373$	$p^R = 0.209$
$r^T = -0.201$	$p^T = 0.510$	$r^T = 0.367$	$p^T = 0.218$
$r^N = 0.106$	$p^N = 0.730$	$r^N = 0.033$	$p^N = 0.914$
$r = -0.047$	$p = 0.880$	$r = 0.231$	$p = 0.447$

Table 3.10: Spearman's coefficient correlation and its significance between the proton flux enhancements and the degree of compressibility related to the shocks reported in the List 2, in the upstream and downstream regions.

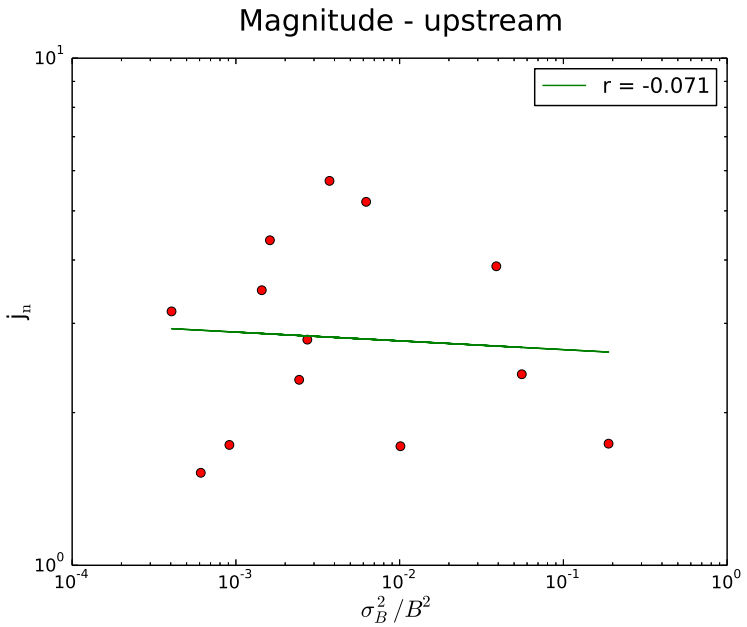

(a)

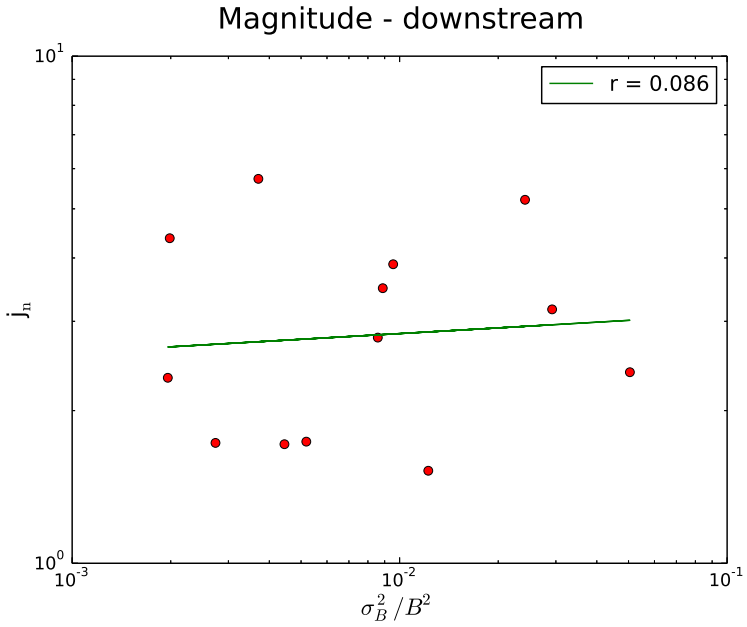

(b)

Figure 3.27: Proton flux enhancements versus degree of compressibility for the magnitude of the magnetic field for all the events of List 2. Panel (a) shows the correlation in the upstream region of the shock while panel (b) in the downstream region. r is the correlation coefficient of the linear fit indicated by the green line.

3.4 Relation with the magnetosonic Mach number

At this point it is interesting to study also the relation between the the turbulence measure and the proton flux enhanncements and the magnetosonic mach number M_{ms} that gives information about the strength of interplanetary shocks.
In the case of the shocks of the List 1 (table 3.1) associated with the SEP events, if we consider the turbulence measure T and the magnetosonic Mach number M_{ms}, we note that the turbulence measure in the downstream region increases as the number of Mach increases, especially for quasi-perpendicular shocks (see figure 3.29).

We performed a nonparametric correlation analysis (Spearman's correlation) between the turbulence measure and the magnetosonic Mach number and the results are listed in table 3.11. From these values we can see a higher correlation downstream compared to the upstream region of interplanetary shocks, as shown in figures 3.28 and 3.29 related to the magnitude of the magnetic field, even if the correlation coefficients are not very significant except the magnitude in the downstream region.

Spearman's correlation

UP		DOWN	
$\rho_s^R = 0.300$	$p^R = 0.259$	$\rho_s^R = 0.328$	$p^R = 0.215$
$\rho_s^T = -0.071$	$p^T = 0.795$	$\rho_s^T = 0.418$	$p^T = 0.107$
$\rho_s^N = 0.040$	$p^N = 0.884$	$\rho_s^N = 0.325$	$p^N = 0.219$
$\rho = 0.153$	$p = 0.571$	$\rho = 0.645$	$p = 0.007$

Table 3.11: Spearman's coefficient correlation between the turbulence measure and the magnetosonic Mach number related to the shocks reported in the List 1 that occur on the wake of a SEP event, in the upstream and downstream regions.

Then we plot the proton flux enhancements j_n in the $4-6$ MeV as a function of the magnetosonic Mach number M_{ms} for interplanetary quasi-perpendicular shocks. From the figure 3.30 we can note a high level of correlation between the two quantities ($r_1 = 0.80$) and this value increases above a value of 1.6 ($r_2 = 0.86$).
A good correlation is found between j_n and the product between the shock-normal angle θ_{Bn} and the magnetosonic Mach number M_{ms}. In fact in this case (figure 3.31) we see that above the threshold the correlation between proton flux enhancements j_n and this quantity increases from $r_1 = 0.66$ to $r_2 = 0.84$. Hence, both θ_{Bn} and M_{ms} seem to be critical parameters for the shock acceleration efficiency at high energies (at least in the $4-6$ MeV range).

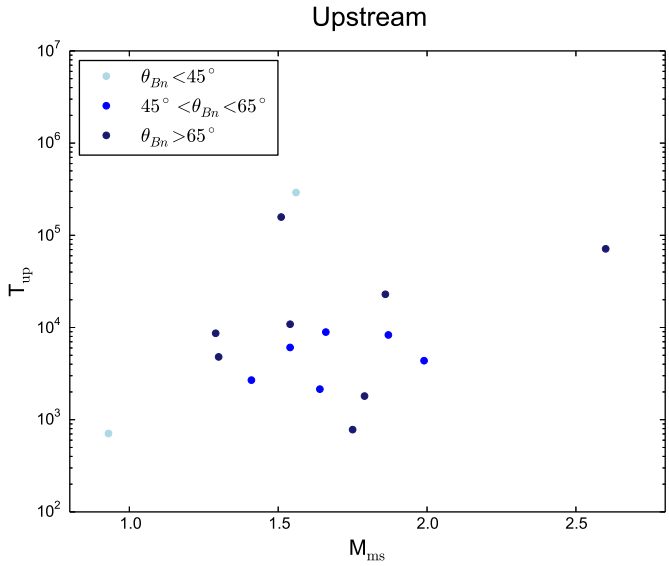

Figure 3.28: Turbulence measure T versus magnetosonic Mach number M_{ms} for the magnitude of the magnetic field in the upstream region of interplanetary shocks that occur on the wake of a SEP event. The values with a $\theta_{Bn} < 45°$, $45° < \theta_{Bn} < 65°$ and $\theta_{Bn} > 65°$ are indicated in light blue, blue and dark blue, respectively.

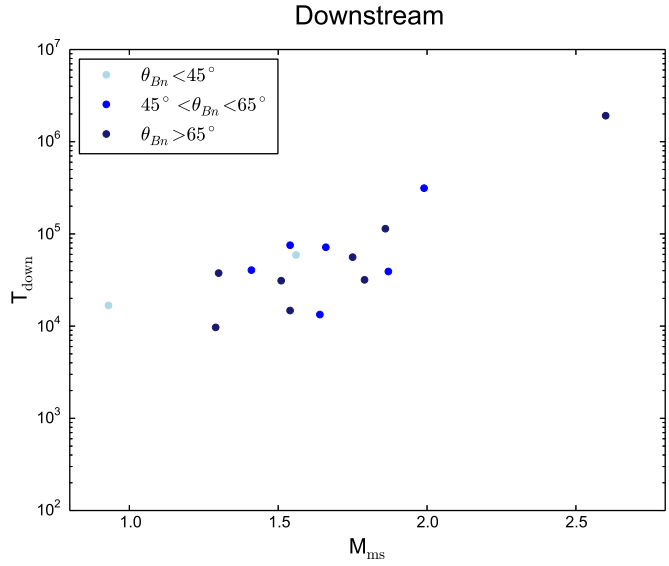

Figure 3.29: Turbulence measure T versus magnetosonic Mach number M_{ms} for the magnitude of the magnetic field in the downstream region of interplanetary shocks that occur on the wake of a SEP event. The values with a $\theta_{Bn} < 45°$, $45° < \theta_{Bn} < 65°$ and $\theta_{Bn} > 65°$ are indicated in light blue, blue and dark blue, respectively.

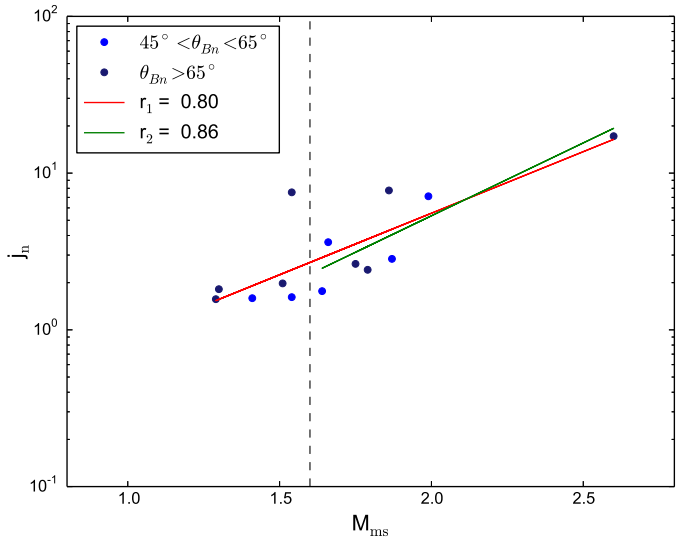

Figure 3.30: Proton flux enhancements j_n versus magnetosonic Mach number M_{ms} for interplanetary quasi-perpendicular shocks ($45° < \theta_{Bn} < 65°$ and $\theta_{Bn} > 65°$ are indicated blue and dark blue, respectively) that occur on the wake of a SEP event. The dotted line indicates a critical value above which the correlation between the two plotted quantities increases ($r_2 > r_1$).

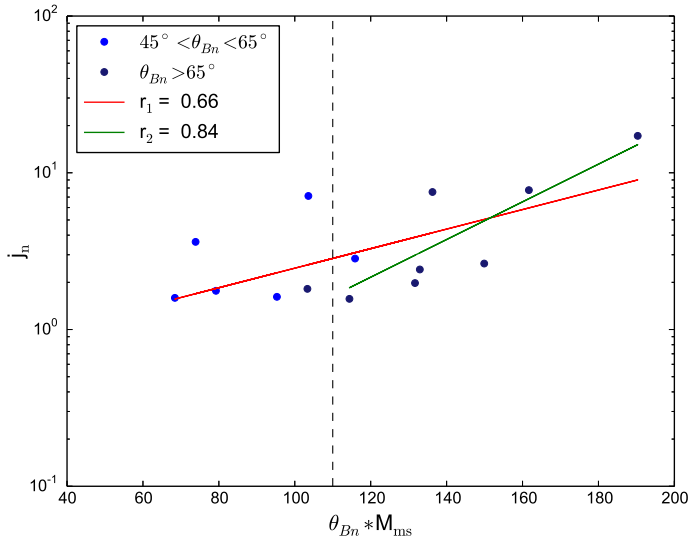

Figure 3.31: Proton flux enhancements j_n versus the product between the shock-normal angle θ_{Bn} and the magnetosonic Mach number M_{ms} for interplanetary quasi-perpendicular shocks ($45° < \theta_{Bn} < 65°$ and $\theta_{Bn} > 65°$ are indicated blue and dark blue, respectively) that occur on the wake of a SEP event. The dotted line indicates a critical value above which the correlation between the two plotted quantities increases ($r_2 > r_1$).

3.5 Kinetic energy spectra

In the second part of this chapter we focus the attention on the study of the evolution of the kinetic energy spectra of the shocks associated with SEP events. The results obtained are, then, discussed in the general framework of acceleration mechanisms to shed light on the nature of particle acceleration involved in this type of events.
In this section we performed the analysis of kinetic energy spectra of ESPs associated with the SEP events of the List 1 (see table 3.1). The data used to study these events are 1-minute averaged proton fluxes measured by the three instruments (SEPT, LET and HET) aboard STEREO A spacecraft in 39 energy channels from 84.1 keV to 100 MeV.
The average differential flux (dJ/dE) was calculated over three hour intervals around the shock. A calibration procedure was applied to compare the energy channels of the three instruments. In particular, we compared the last channel of SEPT ($2.2 - 6.5$ MeV) with the first one of LET ($4.0 - 4.5$ MeV) because they have a comparable geometric mean energy, equal to 3.8 MeV and 4.2 MeV respectively. The second calibration was performed between the last channel of LET ($10.0 - 12.0$ MeV) and the first of HET ($13.6 - 15.1$ MeV) with a geometric mean energy of 11.0 MeV and 14.0 MeV, respectively. Then, the LET and HET fluxes were rescaled by a factor obtained by performing a linear regression between data from the first two channels and from the last two channels, respectively (Laurenza et al., 2015).

3.5.1 Model fit for SEP events

These energy spectra can be fitted with the Weibull functional form (Laurenza et al., 2013), also known as the two-parameter stretched exponential (Frisch and Sornette, 1997), defined as

$$N(E) = k \left(\frac{E}{E_\tau}\right)^{\gamma-1} e^{-\left(\frac{E}{E_\tau}\right)^{\gamma}} . \tag{3.7}$$

Therefore, we take into account the conversion from the particle spectrum to the differential flux, namely

$$\frac{dJ}{dE} = A \times N(E) \times E^{1/2}$$

and we obtain the following distribution

$$\frac{dJ}{dE} = C \left(\frac{E}{E_\tau}\right)^{\gamma-1} E^{1/2}\, e^{-\left(\frac{E}{E_\tau}\right)^{\gamma}} , \tag{3.8}$$

where C, E_τ and γ are the free parameters of the fit.

The Weibull function (Weibull, 1951) is a distribution that has application in many fields of research. In this case, the derivation of the Weibull spectrum of energetic particles is based on truncated stochastic processes exhibiting a power law growth in time. In the framework of particle acceleration, two processes can be related to the Weibull spectra, shock surfing and stochastic acceleration.

Weibull spectrum of energetic particles is essentially based on the connection between the Weibull distribution and the "killed" processes exhibiting a power law growth in time. We consider the simple case of a deterministic process $X(t) = t^\nu$ truncated ("killed") at a random time T which is exponentially distributed as $f(T) = e^{-T}$. The distribution of the killed state $X(T) = T^\nu$ is a Weibull's one $g(X)$, as result of equating the probabilities $g(X)dX = f(T)dT$ with parameter $1/\nu$. In the shock surfing acceleration (SSA) mechanism, at a quasi-perprendicular shocks, the particle energy augments as the power law $E(t) \sim t^2$ (see section 3.1.2) and the acceleration efficiency decreasing with the shock angle θ_{Bn}. Consequently, from SSA mechanism the expected particle spectrum is a Weibull distribution with parameter $\gamma = 1/2$.

An alternative interpretation is provided by stochastic acceleration. In fact, Pallocchia et al. (2017), in order to derive the Weibull spectrum, assume that a set of noninteracting particles is accelerated by a stochastic process.Starting from the classical Fermi's model, they consider particles stochastically accelerated by interactions with magnetic irregularities or turbulent fluctuations, and they assume that the scattering gives to the particles an isotropic distribution. The spatial region where the interactions occur is homogeneous and, therefore, spatial diffusion is not considered. Then, the diffusion equation, that describes the conservation of the number of particles in energy space in the range between E and $E + \Delta E$, is written as

$$\frac{\partial N}{\partial t} = \frac{\partial [b(E)N]}{\partial E} + \frac{1}{2}\frac{\partial^2 [f(E)N]}{\partial E^2} - \frac{N}{\tau} + q_{\rm in}\delta(E)\,, \tag{3.9}$$

where $b(E) = -\frac{d\langle E\rangle}{dt}$ is the mean acceleration rate, $f(E) = \frac{d\langle(\Delta E)^2\rangle}{dt}$, $q_{\rm in}$ is the rate of injection of particles with energy $E_{\rm in}$ in the acceleration process. The first and the second term on the right-hand side of the equation are related to the stochastic nature of the process, the third is connected with the particle leakage from the acceleration region in a characteristic time τ and the last term describes the source of praticle injection in the process. If the increase of the particle energy in time is a power law as in the hypothesis of anomalous diffusion in velocity (Bouchet et al., 2004) the ratio of the second over the first

term tends to zero in the asymptotic limit ($E \to \infty$). Then, equation (3.9) becomes

$$N = -\frac{E_\tau^\gamma}{\gamma} \frac{\partial(E^{1-\gamma} - N)}{\partial E} \tag{3.10}$$

in the case of a stationary state and its integration yields the Weibull spectrum (see equation (3.7)), that represents an exact equilibrium solution to the diffusion-loss equation.

Another functional form can be used to fit the ESP spectra, i.e. the double power law proposed by Band et al. (1993) which is commonly used to fit particle spectra in SEP events (Mewaldt et al. (2012); Desai and Giacalone (2016)). The equation for this spectral shape is given by

$$\begin{aligned} \frac{dJ}{dE} &= C\, E^{-\gamma_a} e^{-\left(\frac{E}{E_0}\right)} \quad \text{for } E \leq (\gamma_b - \gamma_a)E_0 \\ \frac{dJ}{dE} &= C\, E^{-\gamma_b} \left\{ [(\gamma_b - \gamma_a)E_0]^{(\gamma_b - \gamma_a)}\, e^{(\gamma_a - \gamma_b)} \right\} \quad \text{for } E \geq (\gamma_b - \gamma_a)E_0 \end{aligned} \tag{3.11}$$

where γ_a is the low energy power law slope and γ_b is the high energy power law slope. The function is equal to the Ellison-Ramaty form (Ellison and Ramaty, 1985) below the transition energy, $(\gamma_b - \gamma_a)E_0$. At higher energies, the double power law makes a smooth transition to a second power law.

Energy spectra for SEP events in List 1

In figure from 3.32 to 3.45 we report the energy spectra and the best fit of the ESP events (superposed on a SEP event) of the List 1 at quasi-perpendicular shocks; in particular for 6 over the 14 ESP events (see figures from 3.32 to 3.37) we obtain a Weibull functional form, while for 8 over the 14 ESP events in the wake of SEPs (see figures from 3.38 to 3.45) the Weibull like shape fits only the high energy tail.
On the contrary, the two quasi-parallel shocks of the List 1 show a double power law trend as we can see from figures 3.46 and 3.47.

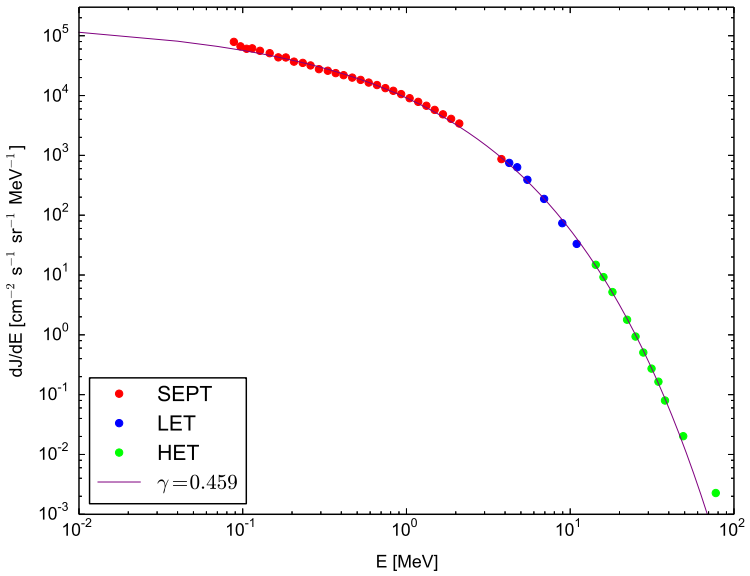

Figure 3.32: Time averaged differential fluxes of energetic particles calculated around the shock arrival on 2011 March 22 SEP event (#3 of the List 1). The data from SEPT, LET and HET are indicated in red, blue and light green, respectively. The solid curve is the Weibull function used to fit the spectra. Data errors are within the marker size.

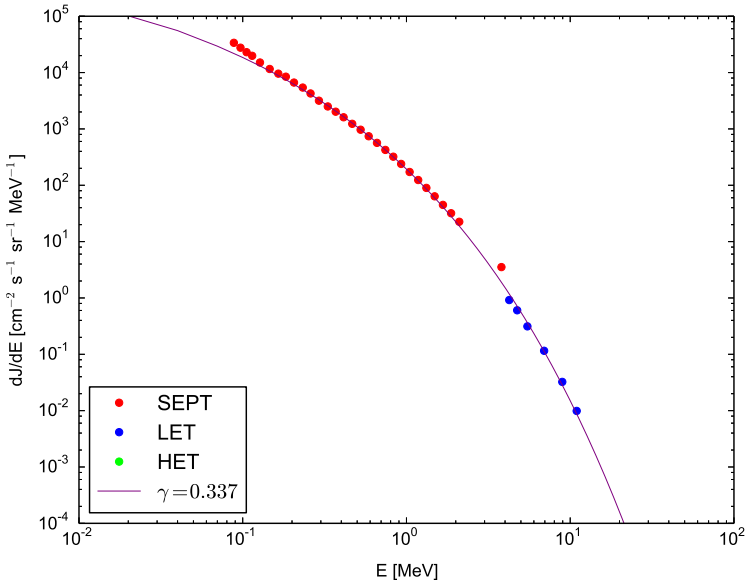

Figure 3.33: Time averaged differential fluxes of energetic particles calculated around the shock arrival on 2011 September 11 SEP event (#4 of the List 1). The data from SEPT, LET and HET are indicated in red, blue and light green, respectively (no data for HET). The solid curve is the Weibull function used to fit the spectra. Data errors are within the marker size.

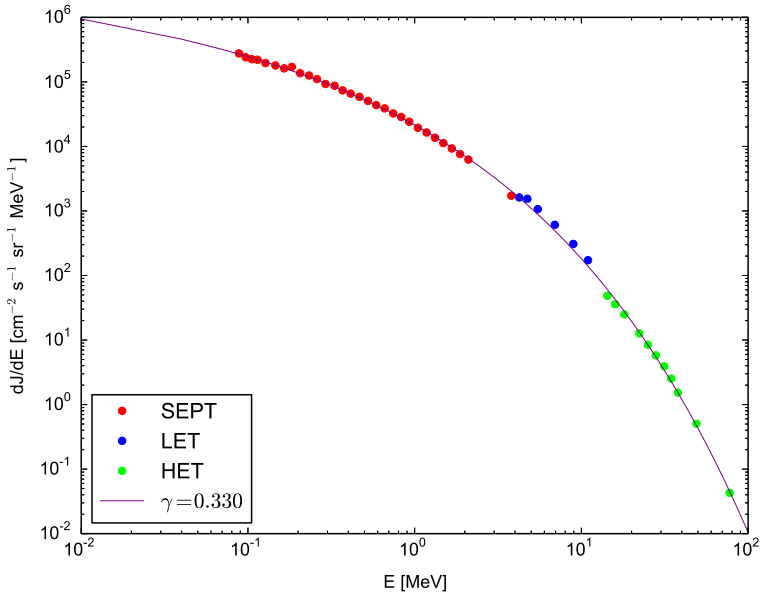

Figure 3.34: Time averaged differential fluxes of energetic particles calculated around the shock arrival on 2012 January 29 SEP event (#7 of the List 1). The data from SEPT, LET and HET are indicated in red, blue and light green, respectively. The solid curve is the Weibull function used to fit the spectra. Data errors are within the marker size.

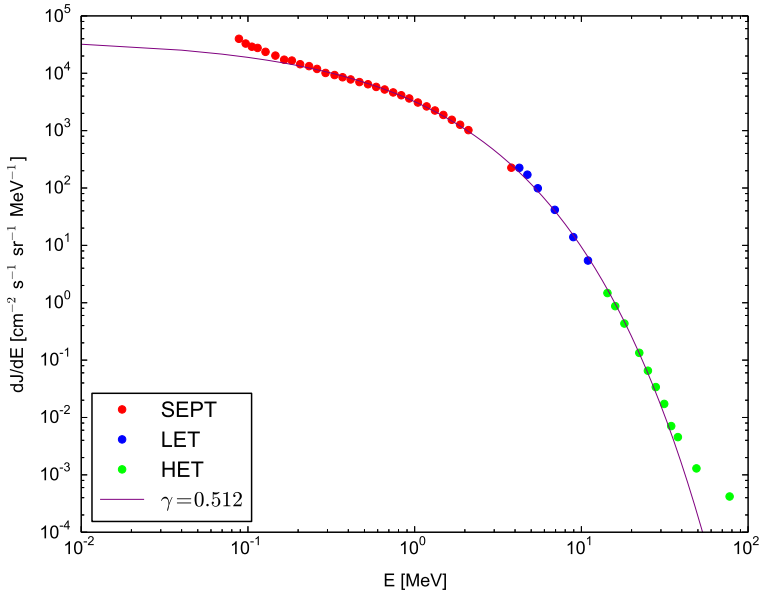

Figure 3.35: Time averaged differential fluxes of energetic particles calculated around the shock arrival on 2012 March 19 SEP event (#9 of the List 1). The data from SEPT, LET and HET are indicated in red, blue and light green, respectively. The solid curve is the Weibull function used to fit the spectra. Data errors are within the marker size.

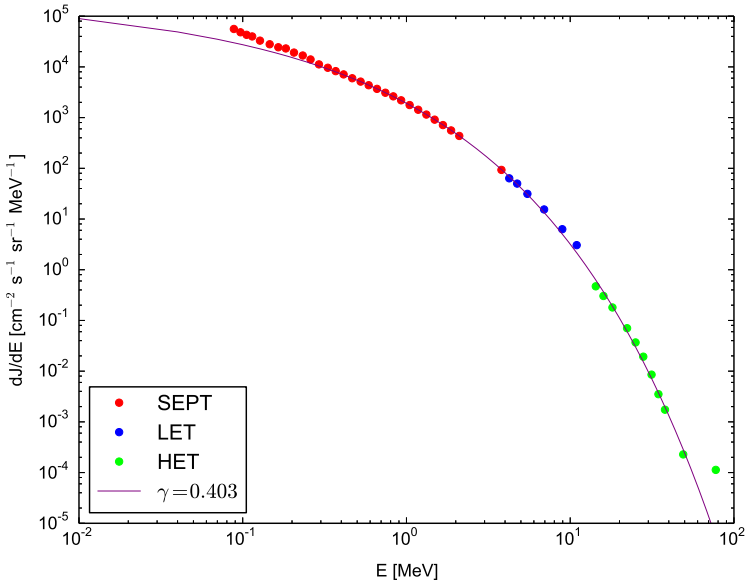

Figure 3.36: Time averaged differential fluxes of energetic particles calculated around the shock arrival on 2013 December 1 SEP event (#16 of the List 1). The data from SEPT, LET and HET are indicated in red, blue and light green, respectively. The solid curve is the Weibull function used to fit the spectra. Data errors are within the marker size.

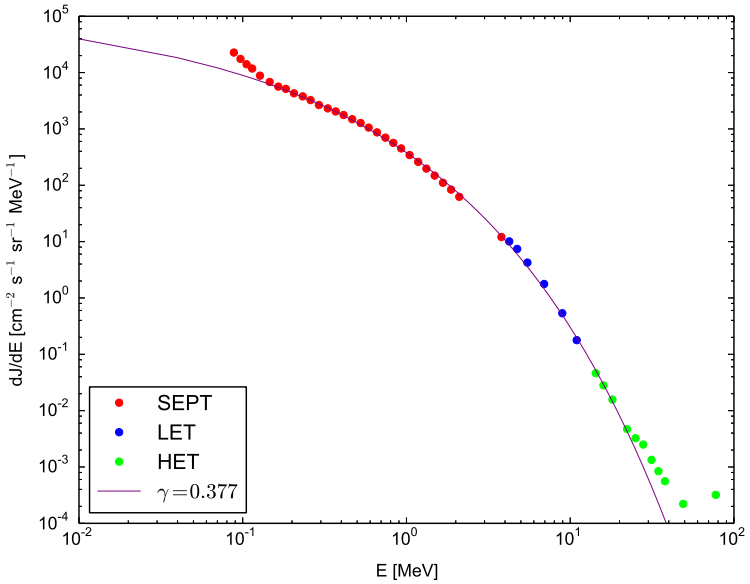

Figure 3.37: Time averaged differential fluxes of energetic particles calculated around the shock arrival on 2014 February 22 (at 23 : 06 UT) SEP event (#19 of the List 1). The data from SEPT, LET and HET are indicated in red, blue and light green, respectively. The solid curve is the Weibull function used to fit the spectra. Data errors are within the marker size.

The following 8 plots show the spectra that are fitted by the Weibull distribution only at high energy, while at low energy we obtain a power law.

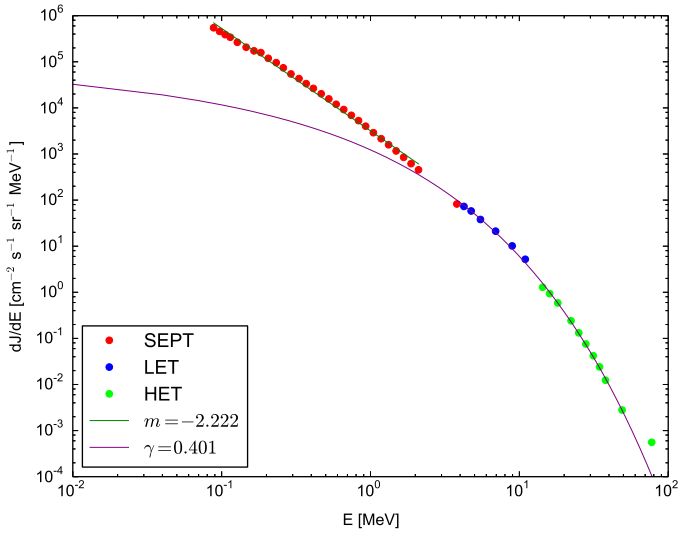

Figure 3.38: Time averaged differential fluxes of energetic particles calculated around the shock arrival on 2011 March 9 SEP event (#2 of the List 1). The data from SEPT, LET and HET are indicated in red, blue and light green, respectively. The solid curves are the power law (green) and the Weibull function (purple) used to fit the spectra. Data errors are within the marker size.

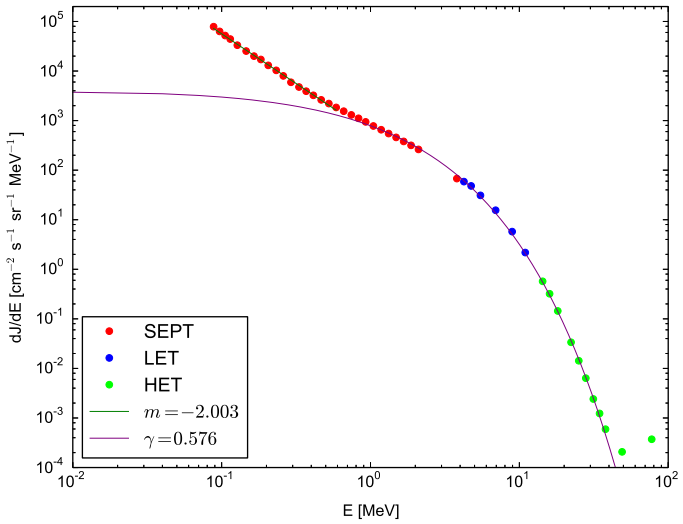

Figure 3.39: Time averaged differential fluxes of energetic particles calculated around the shock arrival on 2011 November 28 SEP event (#5 of the List 1). The data from SEPT, LET and HET are indicated in red, blue and light green, respectively. The solid curves are the power law (green) and the Weibull function (purple) used to fit the spectra. Data errors are within the marker size.

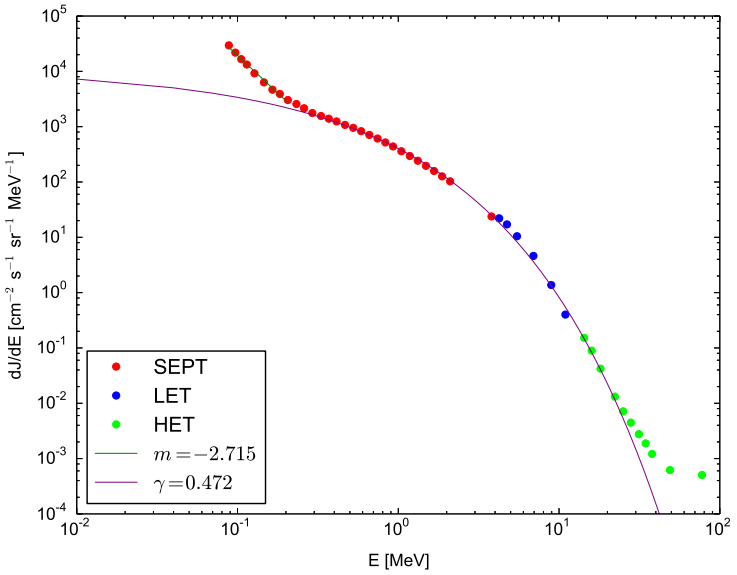

Figure 3.40: Time averaged differential fluxes of energetic particles calculated around the shock arrival on 2012 March 18 SEP event (#8 of the List 1). The data from SEPT, LET and HET are indicated in red, blue and light green, respectively. The solid curves are the power law (green) and the Weibull function (purple) used to fit the spectra. Data errors are within the marker size.

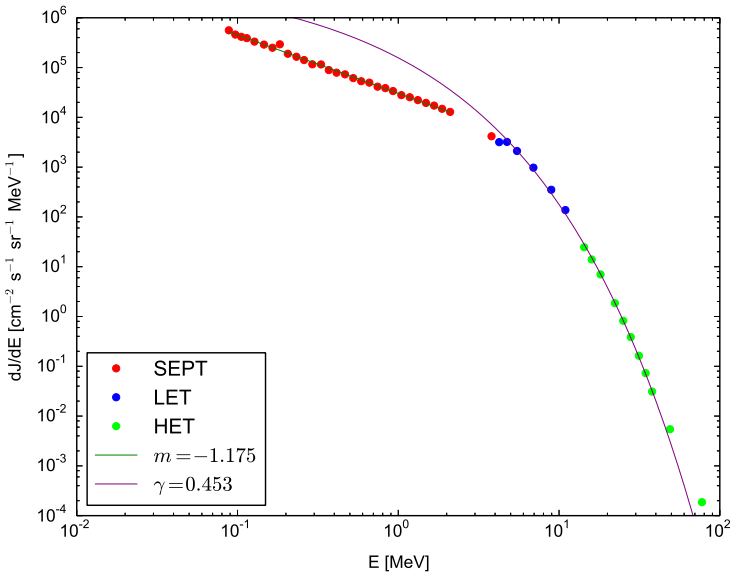

Figure 3.41: Time averaged differential fluxes of energetic particles calculated around the shock arrival on 2012 May 28 SEP event (#10 of the List 1). The data from SEPT, LET and HET are indicated in red, blue and light green, respectively. The solid curves are the power law (green) and the Weibull function (purple) used to fit the spectra. Data errors are within the marker size.

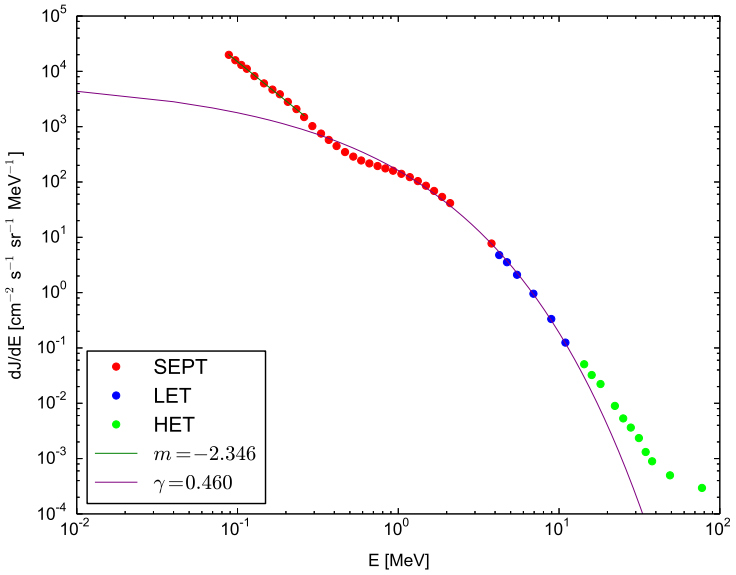

Figure 3.42: Time averaged differential fluxes of energetic particles calculated around the shock arrival on 2014 February 22 (at 08 : 00 UT) SEP event (#18 of the List 1). The data from SEPT, LET and HET are indicated in red, blue and light green, respectively. The solid curves are the power law (green) and the Weibull function (purple) used to fit the spectra. Data errors are within the marker size.

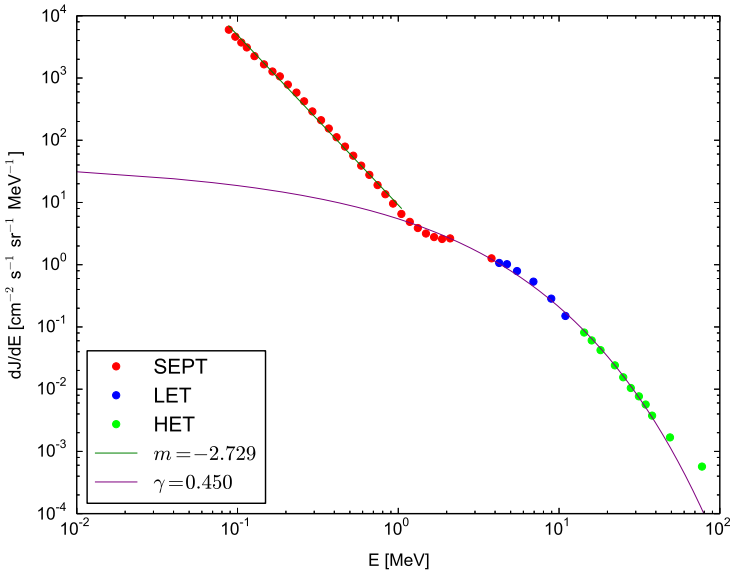

Figure 3.43: Time averaged differential fluxes of energetic particles calculated around the shock arrival on 2014 June 11 SEP event (#20 of the List 1). The data from SEPT, LET and HET are indicated in red, blue and light green, respectively. The solid curves are the power law (green) and the Weibull function (purple) used to fit the spectra. Data errors are within the marker size.

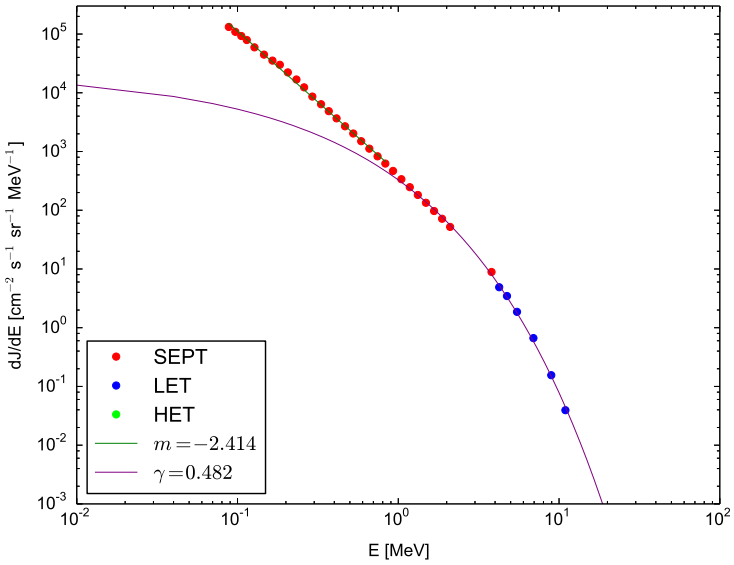

Figure 3.44: Time averaged differential fluxes of energetic particles calculated around the shock arrival on 2014 July 12 SEP event (#21 of the List 1). The data from SEPT, LET and HET are indicated in red, blue and light green, respectively (no data for HET). The solid curves are the power law (green) and the Weibull function (purple) used to fit the spectra. Data errors are within the marker size.

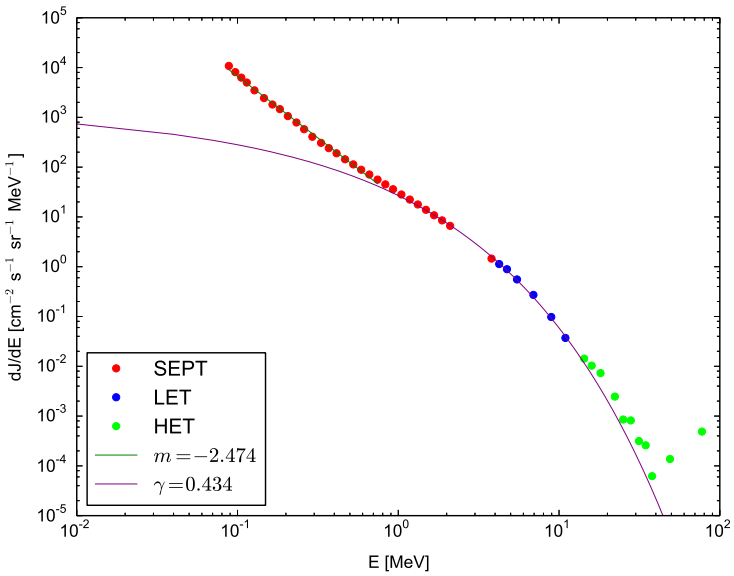

Figure 3.45: Time averaged differential fluxes of energetic particles calculated around the shock arrival on 2016 January 9 SEP event (#23 of the List 1). The data from SEPT, LET and HET are indicated in red, blue and light green, respectively. The solid curves are the power law (green) and the Weibull function (purple) used to fit the spectra. Data errors are within the marker size.

As mentioned above, the spectra relating to quasi-parallel shocks, #6 and #12 of the List 1 (see table 3.1), are described well at low energy by a power law with an exponential cutoff and by a steeper power law at high energy (double power law). Figures 3.46 and 3.47 show the spectra of these two events.

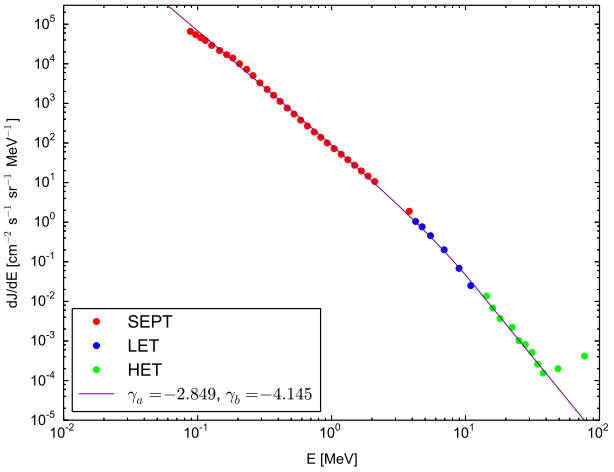

Figure 3.46: Time averaged differential fluxes of energetic particles calculated around the shock arrival on 2012 January 04 SEP event embedded with a SIR (#6 of the List 1). The data from SEPT, LET and HET are indicated in red, blue and light green, respectively. The solid curve is the double power law shape used to fit the spectra. Data errors are within the marker size.

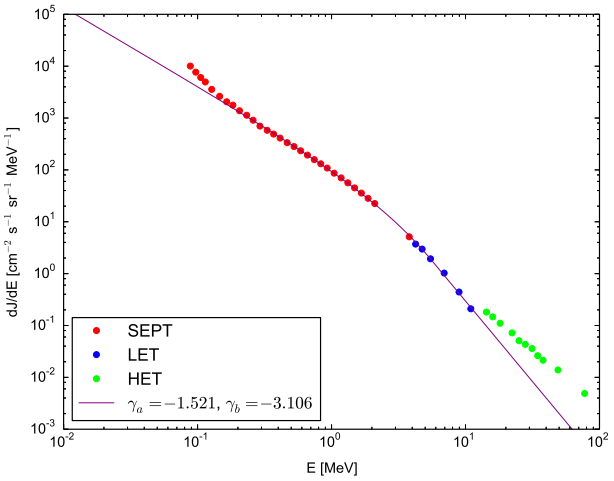

Figure 3.47: Time averaged differential fluxes of energetic particles calculated around the shock arrival on 2012 July 09 SEP event embedded with a SIR (#12 of the List 1). The data from SEPT, LET and HET are indicated in red, blue and light green, respectively. The solid curve is the double power law shape used to fit the spectra. Data errors are within the marker size.

Energy spectra without the background for SEP events in List 1

Then, we performed the energy spectra of the ESPs associated with SEP events of the List 1 after subtracting the background. We obtain similar results as in the previous section: a Weibull functional form for 6 ESP events (see figures from 3.48 to 3.53) and for 8 ESP events (see figures from 3.54 to 3.61) we get the power law at low energy and the Weibull at high energy, except for the events #18 and #19 (2014 February 22 at 08 : 00 UT and 23 : 06 UT, respectively), that show a different behavior.
The two quasi-parallel shocks of the List 1 show also a double power law trend when we subtract the background, as we can see from figures 3.62 and 3.63.

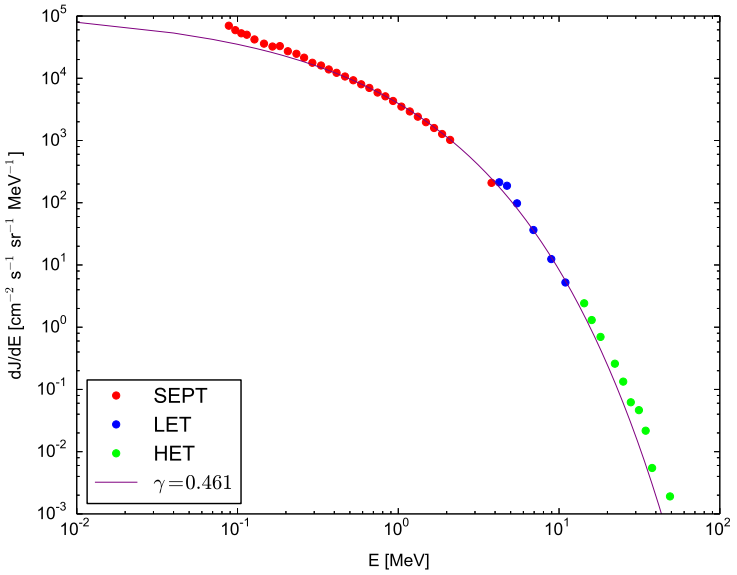

Figure 3.48: Time averaged differential fluxes of energetic particles calculated around the shock arrival on 2011 March 22 SEP event (#3 of the List 1) without the background. The data from SEPT, LET and HET are indicated in red, blue and light green, respectively. The solid curve is the Weibull function used to fit the spectra. Data errors are within the marker size.

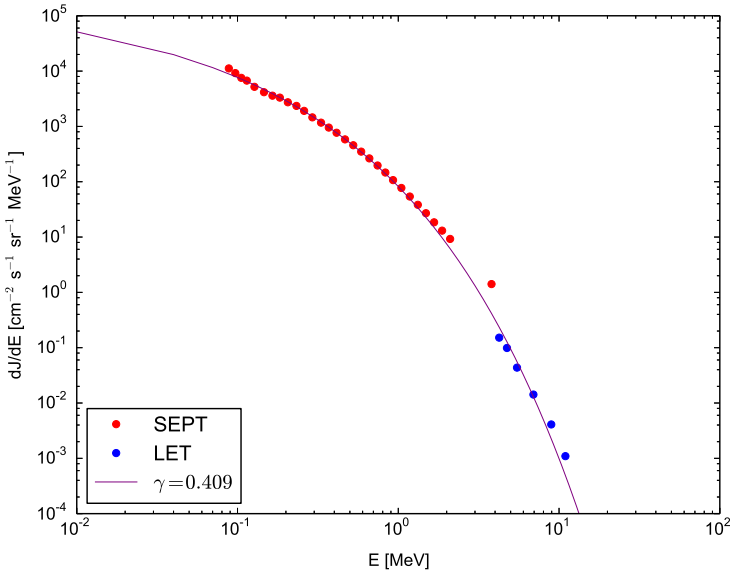

Figure 3.49: Time averaged differential fluxes of energetic particles calculated around the shock arrival on 2011 September 11 SEP event (#4 of the List 1) without the background. The data from SEPT, LET and HET are indicated in red, blue and light green, respectively (no data for HET). The solid curve is the Weibull function used to fit the spectra. Data errors are within the marker size.

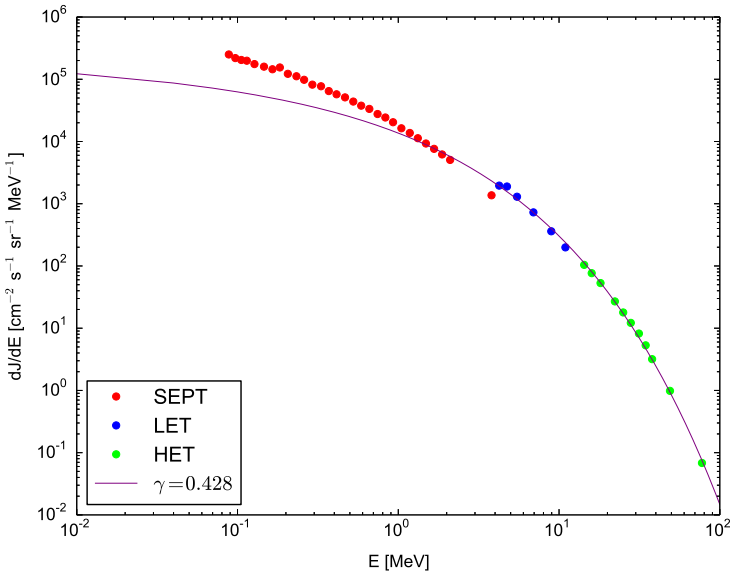

Figure 3.50: Time averaged differential fluxes of energetic particles calculated around the shock arrival on 2012 January 29 SEP event (#7 of the List 1) without the background. The data from SEPT, LET and HET are indicated in red, blue and light green, respectively. The solid curve is the Weibull function used to fit the spectra. Data errors are within the marker size.

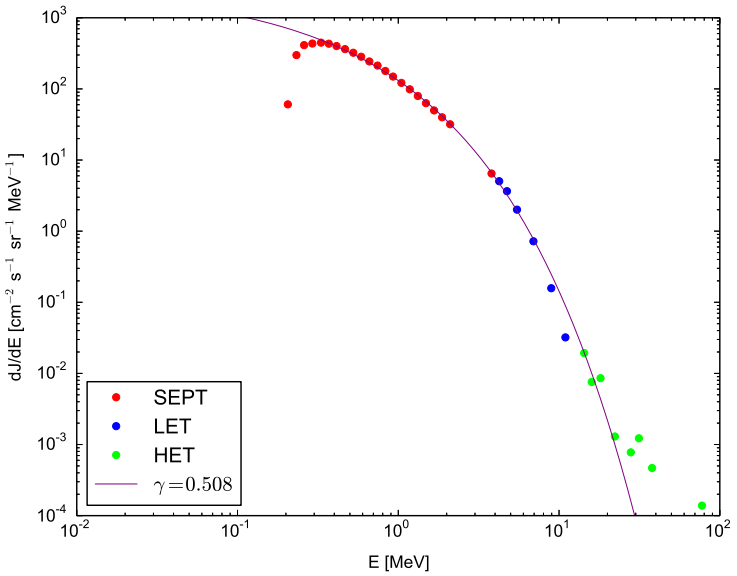

Figure 3.51: Time averaged differential fluxes of energetic particles calculated around the shock arrival on 2012 March 18 SEP event (#8 of the List 1) without the background. The data from SEPT, LET and HET are indicated in red, blue and light green, respectively. The solid curve is the Weibull function used to fit the spectra. Data errors are within the marker size.

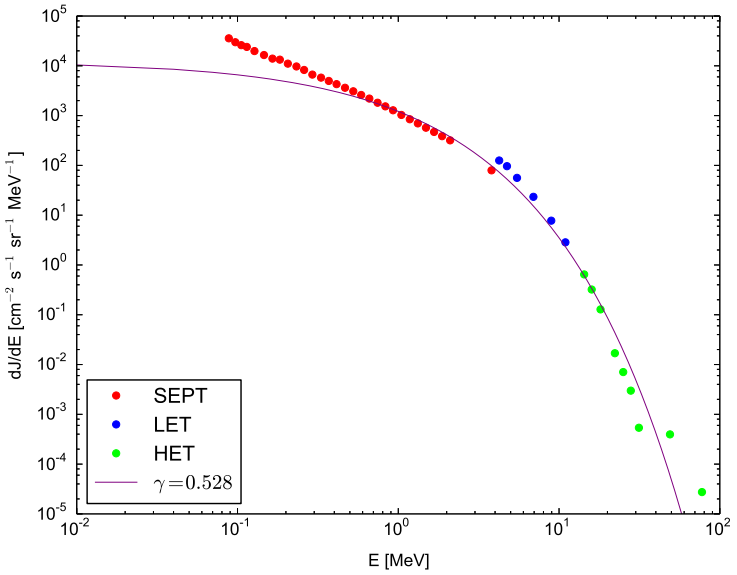

Figure 3.52: Time averaged differential fluxes of energetic particles calculated around the shock arrival on 2012 March 19 SEP event (#9 of the List 1) without the background. The data from SEPT, LET and HET are indicated in red, blue and light green, respectively. The solid curve is the Weibull function used to fit the spectra. Data errors are within the marker size.

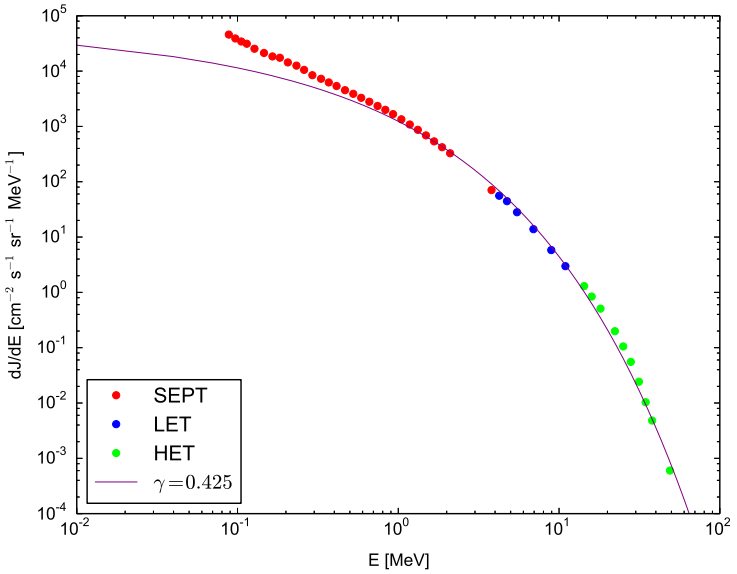

Figure 3.53: Time averaged differential fluxes of energetic particles calculated around the shock arrival on 2013 December 1 SEP event (#16 of the List 1) without the background. The data from SEPT, LET and HET are indicated in red, blue and light green, respectively. The solid curve is the Weibull function used to fit the spectra. Data errors are within the marker size.

Below we report figures from 3.54 to 3.61 that show a power law trend in the range at low energy.

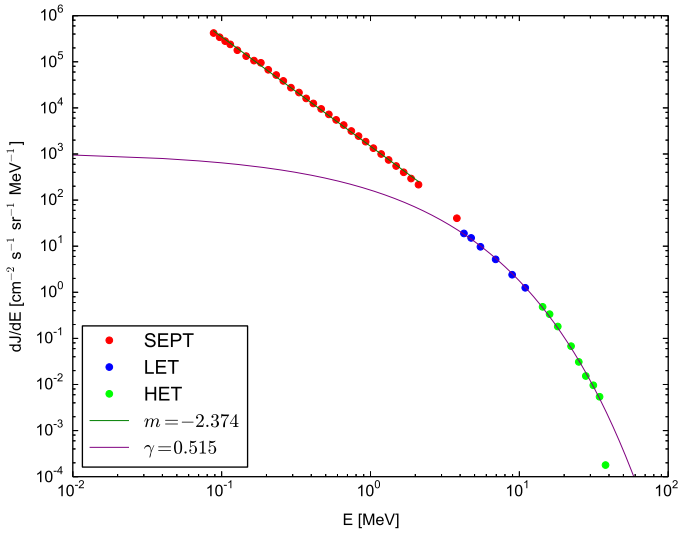

Figure 3.54: Time averaged differential fluxes of energetic particles calculated around the shock arrival on 2011 March 9 SEP event (#2 of the List 1) without the background. The data from SEPT, LET and HET are indicated in red, blue and light green, respectively. The solid curve is the Weibull function used to fit the spectra. Data errors are within the marker size.

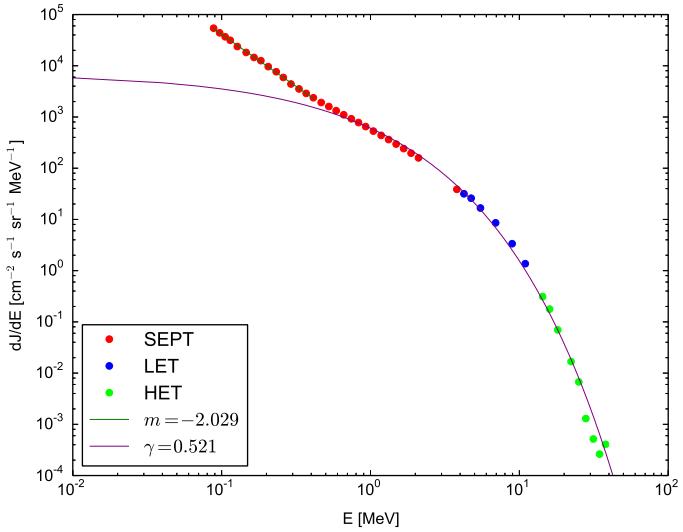

Figure 3.55: Time averaged differential fluxes of energetic particles calculated around the shock arrival on 2011 November 28 SEP event (#5 of the List 1) without the background. The data from SEPT, LET and HET are indicated in red, blue and light green, respectively. The solid curve is the Weibull function used to fit the spectra. Data errors are within the marker size.

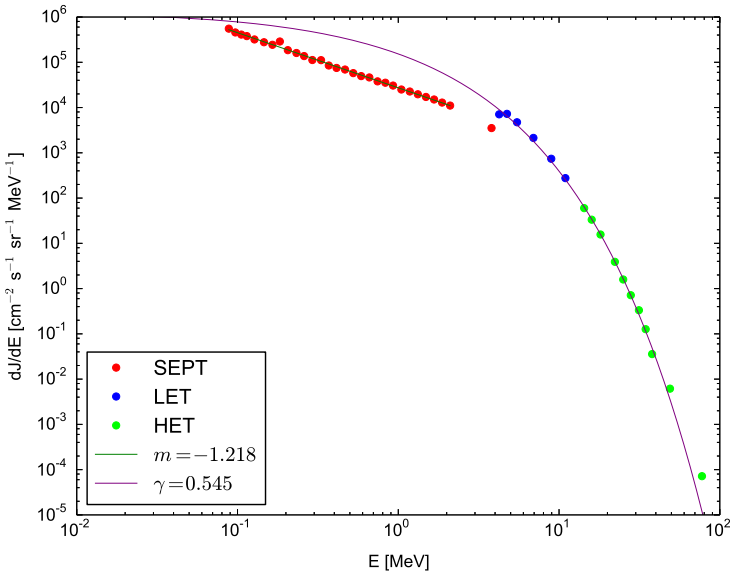

Figure 3.56: Time averaged differential fluxes of energetic particles calculated around the shock arrival on 2012 May 28 SEP event (#10 of the List 1) without the background. The data from SEPT, LET and HET are indicated in red, blue and light green, respectively. The solid curve is the Weibull function used to fit the spectra. Data errors are within the marker size.

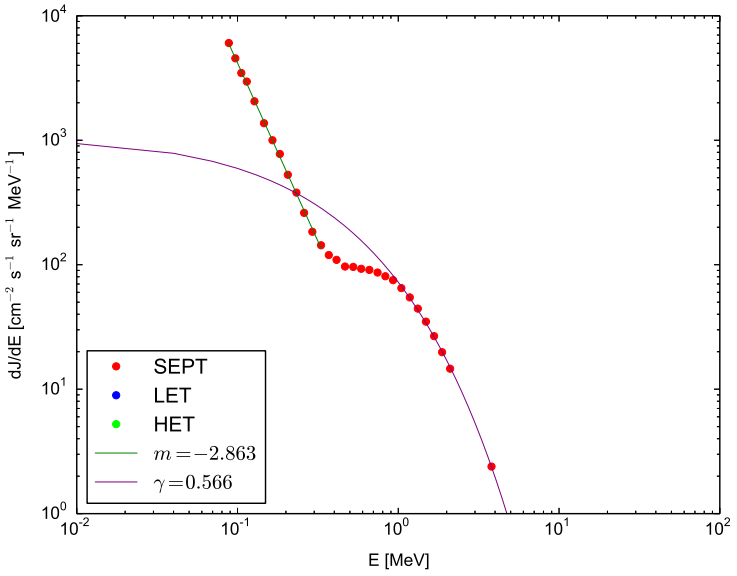

Figure 3.57: Time averaged differential fluxes of energetic particles calculated around the shock arrival on 2014 February 22 (at 08 : 00 UT) SEP event (#18 of the List 1) without the background. The data from SEPT, LET and HET are indicated in red, blue and light green, respectively (no data for LET and HET). The solid curve is the Weibull function used to fit the spectra. Data errors are within the marker size.

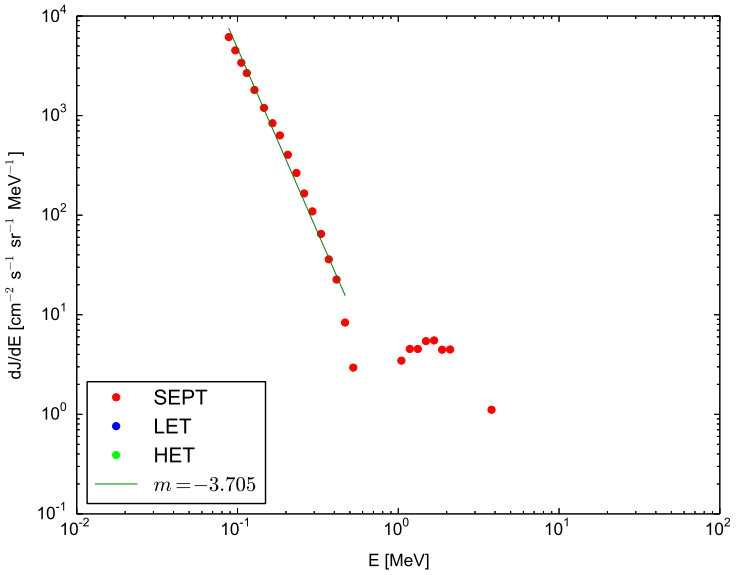

Figure 3.58: Time averaged differential fluxes of energetic particles calculated around the shock arrival on 2014 February 22 (at 23 : 06 UT) SEP event (#19 of the List 1) without the background. The data from SEPT, LET and HET are indicated in red, blue and light green, respectively (no data for LET and HET). The solid curve is the Weibull function used to fit the spectra. Data errors are within the marker size.

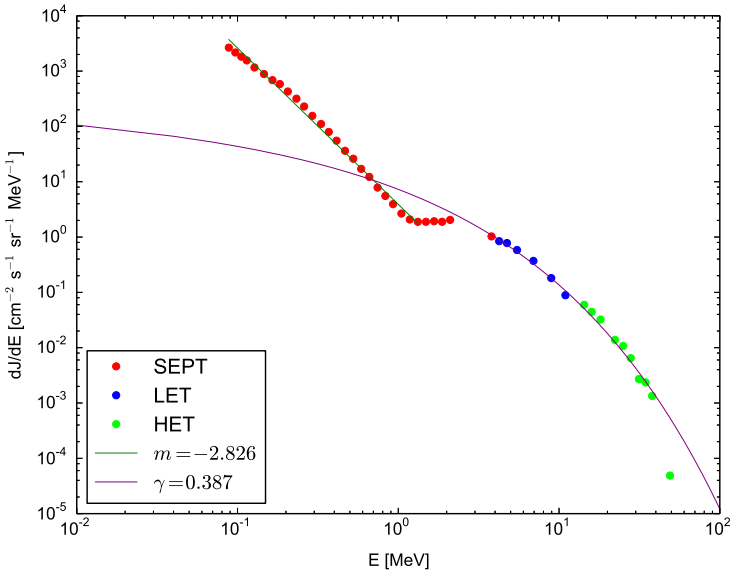

Figure 3.59: Time averaged differential fluxes of energetic particles calculated around the shock arrival on 2014 June 11 SEP event (#20 of the List 1) without the background. The data from SEPT, LET and HET are indicated in red, blue and light green, respectively. The solid curve is the Weibull function used to fit the spectra. Data errors are within the marker size.

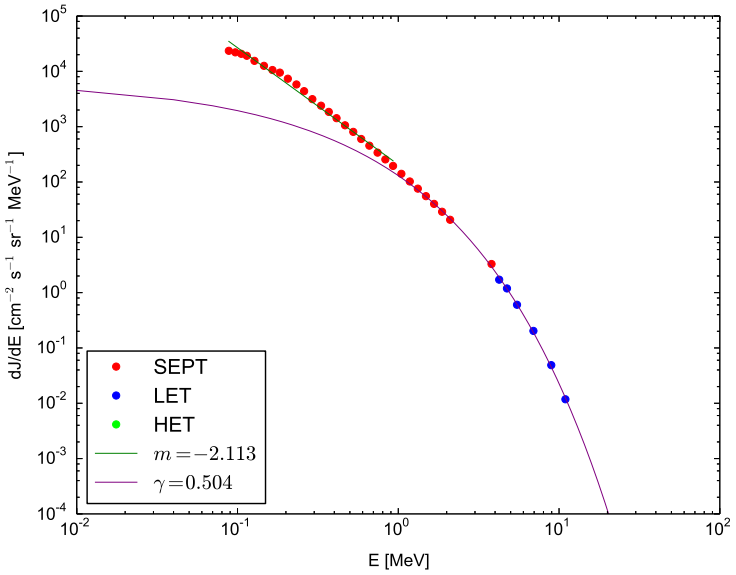

Figure 3.60: Time averaged differential fluxes of energetic particles calculated around the shock arrival on 2014 July 12 SEP event (#21 of the List 1) without the background. The data from SEPT, LET and HET are indicated in red, blue and light green, respectively (no data for HET). The solid curve is the Weibull function used to fit the spectra. Data errors are within the marker size.

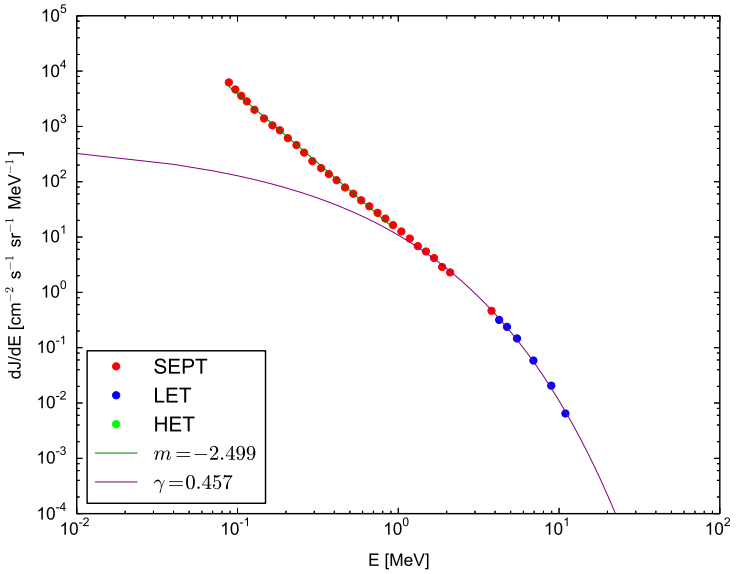

Figure 3.61: Time averaged differential fluxes of energetic particles calculated around the shock arrival on 2016 January 9 SEP event (#23 of the List 1) without the background. The data from SEPT, LET and HET are indicated in red, blue and light green, respectively (no data for HET). The solid curve is the Weibull function used to fit the spectra. Data errors are within the marker size.

The spectra relating to quasi-parallel shocks, #6 and #12 of the List 1 (see table 3.1), are described well by a double power law even when we subtract the background value. Figures 3.62 and 3.63 show the spectra of these two events.

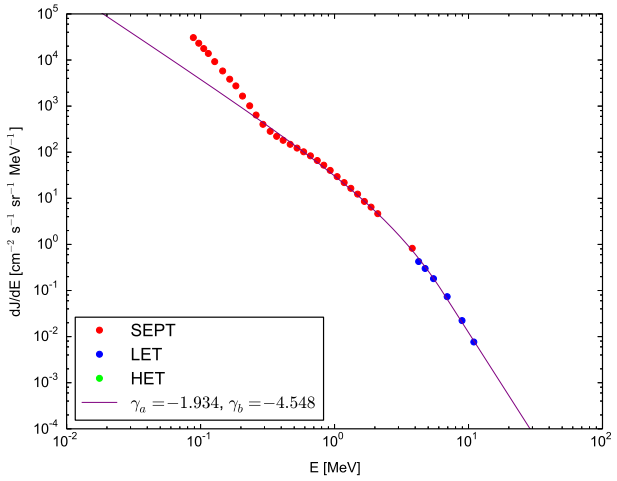

Figure 3.62: Time averaged differential fluxes of energetic particles calculated around the shock arrival on 2012 January 04 SEP event embedded with a SIR (#6 of the List 1) without the background. The data from SEPT, LET and HET are indicated in red, blue and light green, respectively (no data for HET). The solid curve is the double power law shape used to fit the spectra. Data errors are within the marker size.

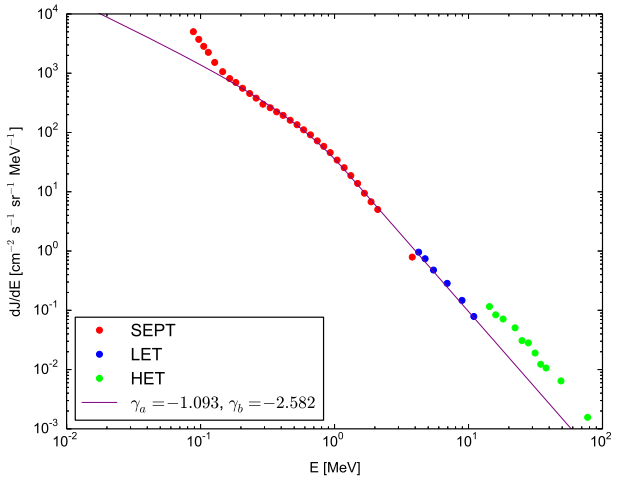

Figure 3.63: Time averaged differential fluxes of energetic particles calculated around the shock arrival on 2012 July 09 SEP event embedded with a SIR (#12 of the List 1) without the background. The data from SEPT, LET and HET are indicated in red, blue and light green, respectively. The solid curve is the double power law shape used to fit the spectra. Data errors are within the marker size.

3.5.2 Discussion

In this section we summarize the results obtained for the kinetic energy spectra three hours around the shock arrival for SEP events. In the case of quasi-perpendicular shocks, the Weibull shape was the best fit, while in the case of quasi-parallel shocks (2 events) with a SIR (Stream Interaction Region) a double power law form. In table 3.12 we report the parameters resulting from the first kind of fit for quasi-perpendicular, where C is a normalization factor, γ is the exponent and E_τ is a characteristic energy. The values of the parameters derived in the background subtracted spectrum are listed in table 3.14. For quasi-parallel shocks, tables 3.13 and 3.15 report the parameters of the double power law for the spectrum and the background subtracted spectrum, respectively. The parameters are a normalization factor (C), the low energy power law slope (γ_a), the high energy power law slope (γ_b) and the energy break (E_0).

As we found that the Weibull function reproduce well the observed energy spectra for the quasi-perpendicular interplanetary shocks at least at high energies, we can possibly test the SSA vs the SA mechanisms by evaluating

Table 3.12: Fit parameters, by using the Weibull functional form, for the quasi-perpedicular shocks associated with SEP events of the List 1.

#	DATE	C ($\times 10^5 \mathrm{cm}^{-2}\mathrm{s}^{-1}\mathrm{sr}^{-1}\mathrm{MeV}^{-1}$)	γ	E_τ(MeV)
2	09/03/2011	2.1 ± 1.9	0.40 ± 0.02	0.05 ± 0.02
3	22/03/2011	4.1 ± 0.4	0.460 ± 0.005	0.119 ± 0.008
4	11/09/2011	257.1 ± 239.5	0.34 ± 0.02	0.002 ± 0.001
5	28/11/2011	0.10 ± 0.01	0.576 ± 0.008	0.29 ± 0.02
7	29/01/2012	153.5 ± 21.9	0.330 ± 0.004	0.017 ± 0.002
8	18/03/2012	0.32 ± 0.08	0.47 ± 0.01	0.090 ± 0.002
9	19/03/2012	1.1 ± 0.1	0.511 ± 0.008	0.15 ± 0.01
10	28/05/2012	277.5 ± 253.5	0.45 ± 0.02	0.06 ± 0.02
16	01/12/2013	8.5 ± 2.3	0.403 ± 0.008	0.032 ± 0.005
18	22/02/2014 at 08 : 00 : 03 UT	0.2 ± 0.2	0.46 ± 0.03	0.06 ± 0.02
19	22/02/2014 at 23 : 06 : 24 UT	7.6 ± 1.8	0.377 ± 0.007	0.014 ± 0.002
20	11/06/2014	0.0006 ± 0.0003	0.45 ± 0.03	0.30 ± 0.09
21	12/07/2014	0.9 ± 0.4	0.48 ± 0.02	0.05 ± 0.01
23	09/01/2016	0.04 ± 0.03	0.43 ± 0.03	0.06 ± 0.02

Table 3.13: Fit parameters, by using the double power law spectrum, for the parallel shocks associated with SEP events of the List 1.

#	DATE	C ($\mathrm{cm}^{-2}\mathrm{s}^{-1}\mathrm{sr}^{-1}\mathrm{MeV}^{-1}$)	γ_a	γ_b	E_0(MeV)
6	04/01/2012	98.4 ± 3.9	-2.85 ± 0.04	-4.15 ± 0.09	9.1 ± 1.1
12	09/07/2012	124.2 ± 3.1	-1.52 ± 0.02	-3.11 ± 0.07	3.5 ± 0.2

the γ exponents. According to the shock surfing acceleration, the energy of particles augments as the power law $E(t) \sim t^2$ (Ohsawa (1987), Lee et al. (1996)). Consequently, we expect a particle spectrum of Weibull type with $\gamma = 1/2$, that is in quite good agreement with the values obtained from the fit procedure performed on the SEP events taken into consideration, as they are close to 0.5, especially in the background subtracted spectrum which directly related to the acceleration at the shock passage. These results confirm that shock acceleration can be associated with this kind of distribution, as proposed by Laurenza et al. (2013). In particular, 6 spectra of ESP events on the wake of SEPs (associated with shocks #3, #4, #7, #9, #16 and #19 of the List 1) can be fitted by the Weibull distribution at low and high energies, whereas, for 8 quasi-perpendicular shocks (#2, #5, #8, #10, #18, #20, #21 and #23) this function fits only the high energy tail. This last type of ESP spectrum suggests that two acceleration mechanisms are at work in different energy ranges, one of which seems to be the DSA at low energies and the

Without background

Table 3.14: Fit parameters, by using the Weibull functional form, for the quasi-perpedicular shocks associated with SEP events of the List 1, after subtracting the background.

#	DATE	C ($\times 10^5 \mathrm{cm}^{-2}\mathrm{s}^{-1}\mathrm{sr}^{-1}\mathrm{MeV}^{-1}$)	γ	E_τ(MeV)
2	09/03/2011	0.02 ± 0.02	0.52 ± 0.03	0.26 ± 0.09
3	22/03/2011	3.8 ± 1.1	0.46 ± 0.02	0.08 ± 0.02
4	11/09/2011	16.8 ± 11.6	0.41 ± 0.02	0.008 ± 0.003
5	28/11/2011	0.19 ± 0.05	0.52 ± 0.02	0.16 ± 0.03
7	29/01/2012	3.3 ± 1.9	0.43 ± 0.02	0.16 ± 0.05
8	18/03/2012	8.4 ± 0.01	0.51 ± 0.01	0.11 ± 0.01
9	19/03/2012	3.3 ± 0.2	0.53 ± 0.03	0.18 ± 0.06
10	28/05/2012	36.1 ± 32.5	0.54 ± 0.03	0.20 ± 0.07
16	01/12/2013	1.7 ± 1.0	0.42 ± 0.02	0.06 ± 0.02
18	22/02/2014 at 08 : 00 : 03 UT	0.04 ± 0.02	0.57 ± 0.04	0.14 ± 0.04
19	22/02/2014 at 23 : 06 : 24 UT	/	/	/
20	11/06/2014	0.004 ± 0.03	0.4 ± 0.3	0.1 ± 0.4
21	12/07/2014	0.3 ± 0.1	0.50 ± 0.02	0.07 ± 0.02
23	09/01/2016	0.02 ± 0.01	0.46 ± 0.03	0.06 ± 0.02

Without background

Table 3.15: Fit parameters, by using the double power law spectrum, for the parallel shocks associated with SEP events of the List 1, after subtracting the background.

#	DATE	C ($\mathrm{cm}^{-2}\mathrm{s}^{-1}\mathrm{sr}^{-1}\mathrm{MeV}^{-1}$)	γ_a	γ_b	E_0(MeV)
6	04/01/2012	45.9 ± 3.9	-1.93 ± 0.08	-4.5 ± 0.3	2.5 ± 0.3
12	09/07/2012	126.4 ± 37.5	-1.1 ± 0.2	-2.58 ± 0.04	0.8 ± 0.2

other is possibly acting as a re-acceleration process as it seems to contribute at high energies. This process could resonably be the SSA, although stochastic acceleration cannot be excluded.
In the case of quasi-parallel shocks (#4 and #12 of the List 1) the diffusive shock acceleration seems to be at work, but modified at high energy by the stochastic re-acceleration as proposed by Afanasiev et al. (2014),that generates the broken (double) power law, instead of simply a power law attributed to the DSA mechanism.

These considerations still hold if we consider the spectra after subtracting the background: they are still well reproduced by the Weibull distribution, at least in the high energy range, except shocks #18 and #19, for which remain only SEPT energy channels. These last two ESP events are fitted by a power law and a Weibull for #18 and by a power law for #19. In this case it is reasonable to assure that only DSA accelerates particles, without any re-acceleration at high energies. Since the particle spectra of the ESPs associated with the SEP events continue to be well described by the Weibull functional form at quasi-perpendicular shocks and by the double power law

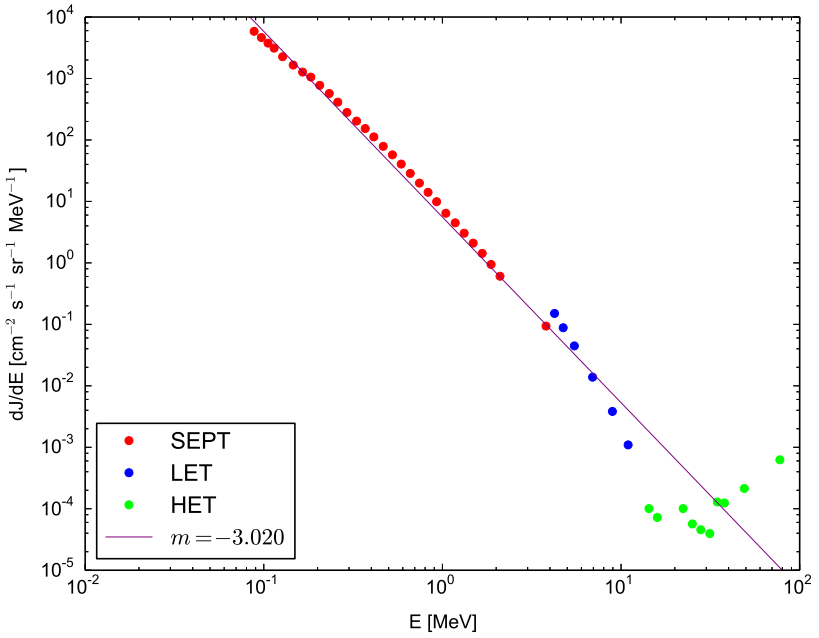

Figure 3.64: Time averaged differential fluxes of energetic particles calculated around the shock arrival on 2010 February 15 in absence of SEP event. The data from SEPT, LET and HET are indicated in red, blue and light green, respectively. The solid curve is the power law with a slope of $m = (-3.02 \pm 0.03)$ used to fit the spectra. Data errors are within the marker size.

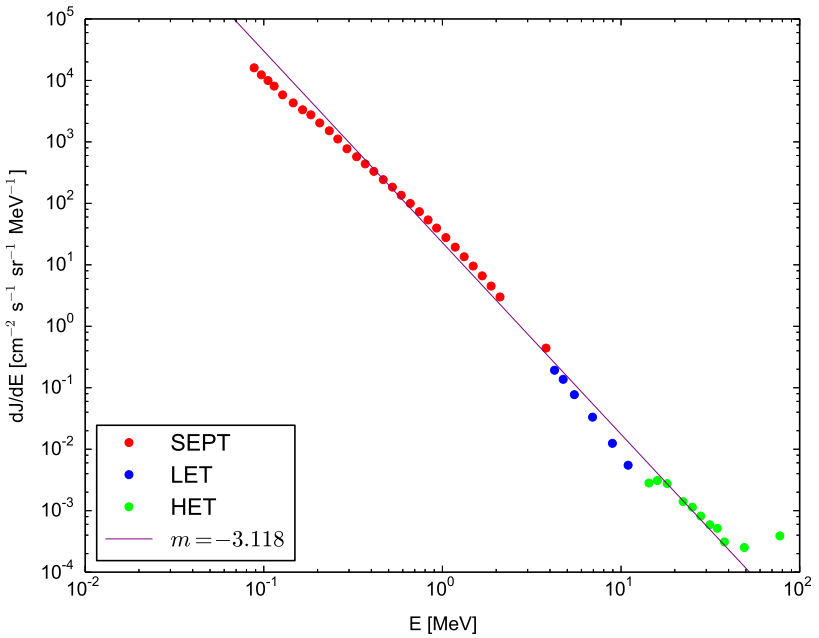

Figure 3.65: Time averaged differential fluxes of energetic particles calculated around the shock arrival on 2013 November 01 in absence of SEP event. The data from SEPT, LET and HET are indicated in red, blue and light green, respectively. The solid curve is the power law with a slope of $m = (-3.12 \pm 0.03)$ used to fit the spectra. Data errors are within the marker size.

at quasi-parallel shocks even when subtracting the background, this suggests that the observed distributions are directly due to shock passage.

The Weibull form has not to be confused with a limited power law as we got for the shocks at which SEP events was not in progress. Two examples of which are shown in figures 3.64 and 3.65. From the linear fit we obtain slopes of $m = (-3.02 \pm 0.03)$ and $m = (-3.12 \pm 0.03)$, respectively. We found this same trend in all the spectra related to the shocks of the first list which occur in absence of SEP event. A pure power law is the typical shape of the classical diffusive shock acceleration, so in the case of interplanetary shock waves without solar energetic particles this seems to be the mechanism of acceleration at work. This result suggest that in order to have a second mechanism at work (e.g. the SSA), as in the case of ESP associated with SEP events, a high background of high energy particles should be present.

3.6 Conclusions

From the study of the magnetic field turbulence in section 3.3, it is evident that, at shock waves a substantial level of turbulent fluctuations is found. Turbulent fluctuations are generally greater by one order of magnitude in the downstream region compared to those in the upstream region. The proton flux enhancements are more intense close to the shock region (List 1) as expected. Indeed, in the case of List 2 there is not a clear increase in the proton flux since the upstream and downstream intervals are more distant from the shock than those considered for the List 1.

We can summarize the results obtained from the correlation study between ESPs and turbulence level as follows.

- For all events of the List 1:
  - not significant correlation between proton flux enhancements (j_n) and turbulence upstream (T_{up}) and downstream (T_{down}) for separated magnetic field components and its magnitude.
- For SEP associated events of the List 1:
  - not significant correlation between j_n and T_{up} for the three components and the magnitude of the magnetic field;
  - significant correlation between the particle flux and T_{down} for R and T components (i.e., those in the equatorial plane of the Sun) and the magnitude.
- NO SEP associated events of the List 1:
  - not significant anticorrelation between j_n and T_{up} for all the components and for the magnitude of the magnetic field;
  - significant anticorrelation between the proton flux and the downstream magnetic field turbulence.
- For all events of the List 2:
  - not significant correlation between the proton flux enhancements and the turbulence upstream and downstream for all the components and the magnitude.

Results for SEP associated events of List 1 could suggest that downstream turbulence plays a direct role in the acceleration process. Nevertheless, this is not supported by results in case of NO SEP events. The above correlation

could be the effect of the SEP streaming, increasing the turbulence level in the shock region.

From the study of energy spectra, we found evidence that different mechanisms could account for the acceleration of the particles in the energy range from few tens of keV up to hundreds of MeV. First of all, it should be noted that in the case of spectra relating to the shocks in which the solar energetic particles are absent (NO SEP events), a pure power law is obtained, typical of the classical diffusive shock acceleration, but with low intensity at energies $\gtrsim 1$ MeV.

Instead, when we consider ESPs associated with SEP events, the shape of the spectra is different. In fact, in the case of the two parallel shocks that occur also in correspondence with a stream interaction region (SIR), the best fit is a double power law, which indicates that the DSA is at work, but potentially modified by SA (stochastic acceleration) at higher energies.

The results obtained for quasi-perpendicular shocks show that the particle spectra associated with shock acceleration are well reproduced by the Weibull functional form, at least in the high energy range (even when the background is subtracted). Hence, high energy seed particles seem to enter into an additional acceleration mechanism producing the Weibull distribution.

According to the shock surfing acceleration (SSA), the expected particle spectrum is a Weibull one with $\gamma = 1/2$, that is in quite good agreement with the values (between 0.41 and 0.57 in the background subtracted case) obtained from the fit procedure performed on the SEP events taken into consideration.

Moreover, in section 3.4 we studied the relation between the proton flux enhancements in the intermediate energy range $4-6$ MeV and the magnetosonic Mach number and between the proton flux enhancements and the product of the magnetosonic Mach number with the shock-normal angle. We analyzed the correlations with these two parameters because M_{ms} and θ_{Bn} are critical parameters in the SSA mechanism and we found a good correlation of these two with the increases of energetic particles. Therefore, SSA seem to be a viable re-acceleration mechanism to explain the high energy tail of the particle spectra at interplanetary quasi-perpendicular shocks connected with shock-spike events (SSEs). Nevertheless, the SA mechanism cannot be excluded, given the positive correlation of both the particle increase and the M_{ms} number with the downstream turbulence.

Further studies about the microphysics and turbulence around the shock front and how it can affect the trapping and acceleration of energetic particles are needed.

Chapter 4

On the origin of high frequency magnetic fluctuations in the interplanetary space

The description of the turbulent spectrum of magnetic field fluctuations in the solar wind in the range of kinetic scales is not yet fully established. While when we consider the spectrum at low frequencies, we can say that some form of dissipation must exist at small scales, the almost collisionless character of the solar wind cannot be avoided when we are dealing with small scales.
The full understanding of the physical mechanisms that allow the dissipation of energy in the absence of collisional viscosity and the knowledge of the dispersive properties would be crucial steps in the problem of high-frequency turbulence in space plasmas.

In homogeneous, neutral and isotropic fluids the turbulent magnetic fluctuations are unpredictable, but their statistics are universal; in fact, the spectral energy density follows (assuming that the Taylor hypothesis is valid) the power law $E(\omega) \sim \omega^{-5/3}$, explained by Kolmogorov assuming the self-similarity of the fluctuations between the energy injection scale and the dissipation one. Since the first measurements of magnetic fluctuations in the interplanetary space (Coleman, 1968), it has been known that also the solar wind magnetic energy density decays as $E(\omega) \sim \omega^{-5/3}$, confirming the validity of the turbulence framework (Bruno and Carbone, 2016). This approach has been also successfully applied to interpret anomalous scalings due to intermittency of fluctuations through multifractal models (Burlaga (1991); Carbone (1993)), and the nonlinear energy cascade, described by a Yaglom relation for the mixed third-order moment of fluctuations (Sorriso-Valvo et al., 2007). In a magnetized plasma, it is complicated to imagine self-similarity over all the

scales where turbulent fluctuations are observed; in fact, the Kolmogorov behavior breaks down at a frequency $f_{\rm i}$, which corresponds approximately to ~ 0.5 Hz (Leamon et al., 1998), comparable with the ion-cyclotron frequency, where fluid and MHD regimes are no longer valid. Beyond the spectral break, a steeper power spectrum is observed. In this region the magnetic energy density decays as $E(\omega) \sim \omega^{-\alpha}$, where the slope is strongly dependent on the analyzed sample. From a statistical study of the energy spectra in the frequency range $[1, 180]$ Hz, Sahraoui et al. (2013) found that 75% of the analyzed spectra exhibit spectral slopes between 2.5 and 3.1 with a peak at about $\alpha \simeq 2.8$.
The presence of fluctuations at high frequencies has been attributed to dispersive phenomena generated by velocity-space effects and electron dynamics (Marsch, 2006) and interpreted in terms of a further turbulent energy cascade driven by wave-wave coupling, as for example a quasi two-dimensional cascade of Kinetic Alfvén Waves (KAWs) (Sahraoui et al., 2009) for which $E(\omega) \sim \omega^{-7/3}$. However, a clear detection of single wave modes in the frequency-wavenumber diagram is difficult due to the presence of large scattering, sideband modes, sporadic wave-trains as envelope solitons, and zero-frequency modes (Narita et al. (2011), Perschke et al. (2016)). Moreover, the situation is complicated by the failure of the Taylor hypothesis, implying that measurements in the time domain cannot be simply translated into the wave-vector domain (Narita, 2018). Another breakpoint in the magnetic energy power spectrum has been observed in Cluster spacecraft data at higher frequencies, of the order of few tens of Hz, roughly corresponding to the electron gyro-frequency $f_{\rm e}$. This second breakpoint has been attributed to the dissipation of KAWs.

Unlike low frequency fluctuations, succesfully described in the nonlinear energy cascade framework, the interpretation of the high frequency spectrum is less clear. The power spectrum for $\omega > \omega_{\rm i}$ has been fitted either through a function made by a combination of $\omega^{-8/3}$ decay and an exponential decay, compatible with the proton Landau damping of magnetic fluctuations (Alexandrova et al., 2012), or by a combination of two power laws (Sahraoui et al. (2009), Sahraoui et al. (2013)), with the slopes of the secondary power law, at $\omega > \omega_{\rm e}$, in the range $\alpha \in [3.5; 5.5]$ with a peak at about $\alpha \simeq 4$.

4.1 Small-scale Turbulence scenarios

As it is known from basic plasma physics, the linear theory for collisionless plasmas yields three types of modes at and below the proton cyclotron

frequency $\Omega_{\rm p}$. When $\Omega_{\rm p} > \omega_r$ (with ω_r the real part of the frequency fluctuations) and the wavevectors are transverse to the background magnetic field, two modes are present, a left-hand polarized Alfvén cyclotron mode and a right-hand polarized magnetosonic mode. The third mode is the ion-acoustic one, that is damped except when $T_{\rm e} \gg T_{\rm i}$, a condition which is rare in the turbulence of the solar wind. At quasi-perpendicular propagation the alfvénic modes evolves into Kinetic Alfvén Waves (KAW), while the magnetosonic branch may propagate at $\Omega_{\rm p} \ll \omega_r$ as whistler modes. There is a debate about the fact that turbulence follows the whistler mode or the KAW branch, before it is dissipated at small scales.

The scenario of whistler modes involves a two-mode cascade process, both alfvénic and magnetosonic modes, which are only weakly damped when $\beta \leq 1$, transfer energy to transverse propagating wavevectors. The KAW are damped by Landau damping which is proportional to $k_\perp^2$, so that they do not contribute to the formation of the dispersive region, except for the fluctuations that propagate in the perpendicular direction. Quasi-parallel magnetosonic modes are not damped, then the right-hand polarized fluctuations can generate a dispersive region of whistler modes.
On the other hand, alfvénic turbulence at long wavelength transfer energy to quasi-perpendicular propagation up to the thermal proton gyroradius where fluctuations are subject to the proton Landau damping. The fluctuations continue the cascade to small scales as KAW at quasi-perpendicular propagation (Sahraoui et al., 2009).

4.2 High frequency Magnetic energy spectra in Solar Wind turbulence

The main question is not which mode is present, but rather what are the conditions that favor one mode over the others in the high-frequency part of the magnetic energy spectrum. Observations of small-scale turbulence show that the electric field is strongly enhanced after the spectral break (Bale et al., 2005). Consequently, the turbulence at these scales is essentially electrostatic in nature, even if there are weak magnetic fluctuations. The increase of the electrostatic part strongly indicates the presence of KAW, as shown by the gyrokinetic simulations (Howes et al., 2008). However, this behavior can be well reproduced by Hall-MHD turbulence, without the presence of KAW modes (Matthaeus et al., 2008). In particular, in the absence of viscous and dissipative terms the statistical equilibrium ensemble of the Hall-MHD equations in the wave-vectors space is produced with an increase of the electric

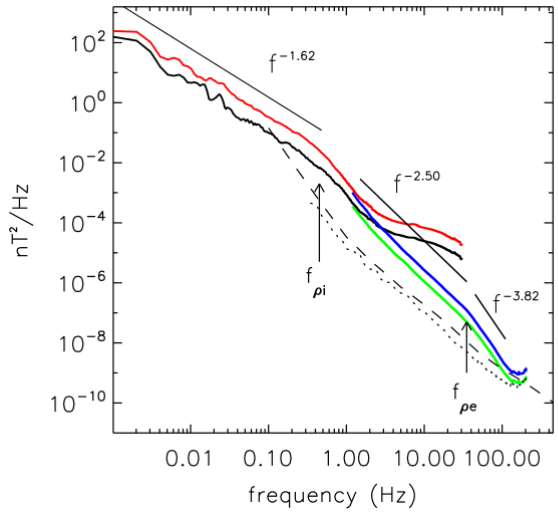

Figure 4.1: Merging of the parallel and perpendicular magnetic spectra of FGM data (plotted with black and red lines) with those of STAFF-SC data (green and blue lines). The dashed and dotted lines indicate the STAFF-SC noise level measured in laboratory and in-flight. The straight black lines are the power law fits of the magnetic spectra and the arrows indicate frequencies of the breakpoints (image credit: Sahraoui et al. (2009)).

field at large wavevectors and this results to be a statistical property of the inviscid Hall-MHD (Servidio et al., 2008). Consequently, it is not certain that the increase in the electrostatic part of the fluctuations is due to the presence of the KAW in the dispersive region.

Apart for the break identified by Leamon et al. (1998) in the magnetic spectrum, a new breakpoint is found in the solar wind turbulence using high-frequencies (up to 100 Hz) data from Cluster spacecraft with the advantage of high resolution (Sahraoui et al., 2009). These authors made a good matching between the FGM (Flux Gate Magnetometer) data covering the frequency spectrum up to 33 Hz and the STAFF-SC (Search Coil) data in the range $1.5 < f < 225$ Hz. Figure 4.1 shows two distinct spectral breaks at $f_\mathrm{i} \sim 0.4$ Hz and $f_\mathrm{e} \sim 35$ Hz, which correspond, respectively to the proton and electron gyroscales ($\rho_\mathrm{i,e} = v_\mathrm{th_{i,e}}/\omega_\mathrm{ci,e}$). Using the Taylor frozen-in flow hypotesis ($\omega \sim kv$), these scales are Doppler-shifted; in particular, the ratio of the two frequencies $\omega_\mathrm{e}/\omega_\mathrm{i} \sim 35/0.4 \sim 90$ is very close to the ratio $\rho_\mathrm{i}/\rho_\mathrm{e} = \sqrt{m_\mathrm{i}T_\mathrm{i}/m_\mathrm{e}T_\mathrm{e}} \sim 95$.
Below f_i, the spectrum follows a Kolmogorov scaling $f^{-1.62}$ while above this characteristic frequency the scaling becomes $f^{-2.5}$, explained by dispersive effects. Above the electron gyrofrequency, they found for the first time that the spectrum has a steeper power law f^{-4}, even if the fit is not very accu-

rate because it extends over less than a decade due to the noise level of the instrument. This description of dispersive cascade and dissipation at electron scales appears consistent with KAW turbulence, as predicted by Howes et al. (2008). Kinetic Alfvèn Waves turbulence has been observed by Bale et al. (2005) only at large proton scales, while Sahraoui et al. (2009) have observed this behavior down to electron scales where dissipation becomes evident.

It is interesting to note that the power spectrum at frequencies greater than f_i can be fitted through several functions: a double power law as emphasized by Sahraoui et al. (2009), an exponential decay, an hybrid function made by a combination of $\omega^{-8/3}$ and an exponential function, compatible with the proton Landau damping of magnetic fluctuations (Alexandrova et al., 2012) and an asymptotic double power law (Sahraoui et al., 2013). These last authors performed a statistical study of the magnetic energy spectra in the frequency range $[1, 180]$ Hz and they showed that the exponential model does not provide a good fit to the data as the others.
In particular, Sahraoui et al. (2013) (Figure 4.2) made a comparison of the analyzed magnetic energy spectra with the fitting models discussed above and they show that the double power law model fits the data better since it captures the observed spectral break.

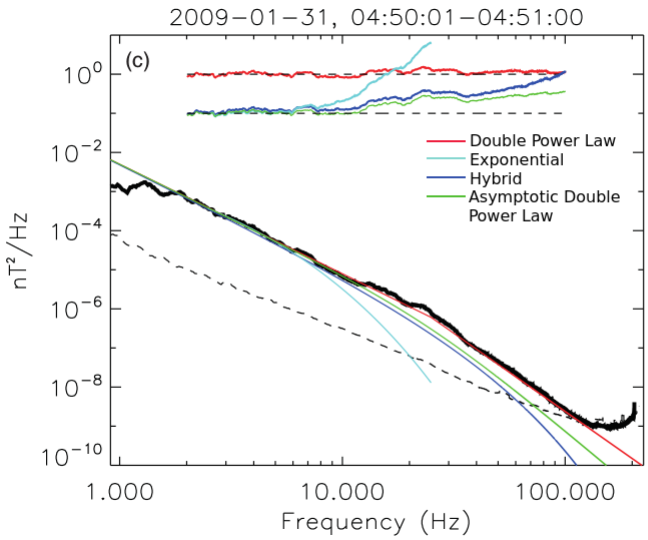

Figure 4.2: Typical example of energy spectrum of the magnetic field measured in the solar wind by the STAFF-SC instrument aboard Cluster 2 (black line); the dashed line refers the estimated (in flight) sensitivity floor of the instrument. The fitting models are plotted for comparison: the double power law (red), the exponential (cyan), the hybrid function (blue) and the asymptotic double power law (green). The horizontal curver are the compensated spectra $B^2(f)/P(f)$ with $P(f)$ the corresponding fitting function (image credit: Sahraoui et al. (2013)).

In fact, they have found that among the total of 610 spectra, 461 (75%) show the break at electron scales with the slopes (α) of the secondary power law, above the elctron gyrofrequency, in the range between 3.5 and 5.5 with a peak at about 4. The remaining 25% of the analyzed spectra do not exhibit clear breaks, due to the fast solar wind where the breakpoints would be shifted to frequencies greater than those taken into account ($\gtrsim$ 180 Hz) or that show bumps at electron scales.

4.3 A Brownian-like approach

The understanding of the small-scale termination of the cascade of turbulent energy in plasmas without collisions is today one of the unsolved problem in space plasma physics. In absence of viscosity and resistivity, the dynamics of small scales is of kinetic nature, and so it must be described by the kinetic theory of plasma. Then, we focused the attention on the problem of the origin of high frequency fluctuations in the interplanetary medium, by studying whether the whole spectrum, for frequencies greater than the ion frequency, can be predicted by a single model. In this way, we try to identify the physical mechanism that establishes a link between the macroscopic and the microscopic scales.

At small scales, of the order of the ion or electron gyro-radii or inertial lengths, the dynamics of the plasma in the interplanetary space is very complex. In fact, the linear mode waves become kinetic, exhibiting simultaneously a dispersive and dissipative character due to the interactions between wave and particles such as coherent scattering processes or incoherent processes.
The nonlinear energy cascade is definitely active at the largest scales and transfers energy beyond the ion-cyclotron frequency, exciting electric fluctuations while in the magnetic fluctuations the energy content is lower (Bale et al., 2005). At the same time, the fluctuations provide a mechanism for heating in the collisionless plasma, because they are damped by plasma kinetic effects. The wave-particle mechanism involved in the dissipation acts as a feedback for fluctuations, since it generates beams of particles which, in turn, are able to excite further fluctuations.
The complex plasma dynamics at small scales, well documented in literature but far from being explained within a unique framework, involves a medium where random fluctuations and dissipation compete in generating magnetic fluctuations. In a range of scales where collisionless dissipation and plasma heating could take place and the presence of characteristic frequencies breaks

the scale-free behavior, the role of dispersion and dissipation is still poorly understood, and the origin of fluctuations is far from being clearly established. This framework is clearly far from the "classical" turbulent dynamics where the nonlinear cascade operates within a scale-free range which is well separated from the smallest scales where dissipation occurs.

4.3.1 Model

To provide a more suitable description of the high-frequency dynamics of magnetic fluctuations, a novel scenario, based on a stochastic Brownian approach, is introduced. This approach allows an interpretation of the observed high frequency magnetic spectra with no assumptions about dispersion relations from plasma turbulence theory. Based on the above considerations, we consider a simple framework where magnetic fluctuations $b(t)$ at small scales can be roughly described by a Itô stochastic differential equation

$$db(t) = \Gamma[b(t), t]\, dt + \Psi[b(t), t]\, dW(t)\,. \tag{4.1}$$

The model can be generalized to three-dimensional fluctuations, even if in this discussion we consider only the time evolution of a single component of the fluctuations, without loss of generality. In the simplest case, we assume that the dynamics of the fluctuations is described through the two terms on the right hand side of equation (4.1) that represent two different contributions. The first term is due to the collisionless dissipative processes, which we parametrize with a linear damping term $\Gamma[b(t), t] \simeq -\gamma b(t)$, where γ is the constant damping rate. The second contribution, instead, simulates all the complex wave dynamics, described by the Wiener process $dW(t)$. $\Psi[b(t), t]$ is assumed to be equal to the root mean square (r.m.s.) of the fluctuations, $F_0 = \langle b^2 \rangle^{1/2}$.
The random forcing is expressed as $dW(t) = \xi(t)dt$, in which we assume that $\xi(t)$ is a real noise, possibly different from a white noise, with finite correlation times, and that $\xi(t)$ is uncorrelated with the initial values of magnetic fluctuations $b(0)$, that is $\langle \xi(t) b(0) \rangle = 0$. Then, with these hypotheses, the equation (4.1) takes the form

$$db(t) = -\gamma b(t) dt + F_0 \xi(t) dt\,. \tag{4.2}$$

Under the above assumptions, the Itô equation can be solved with the Fourier transforms. This provides a relation between the correlations of the Fourier

modes of the forcing ξ_ω and the power spectrum of magnetic energy modes b_ω

$$\langle b_\omega b_\omega^\star \rangle = \frac{F_0^2 \langle \xi_\omega \xi_\omega^\star \rangle}{(\gamma - i\omega)(\gamma + i\omega)} \,, \tag{4.3}$$

where the angular brackets indicate time averaging and $\star$ stands for the complex conjugate. Using the property of homogeneity, we can write the spectral correlations of the forcing term as

$$\langle \xi_\omega \xi_\omega^\star \rangle = 2\pi G(\omega)\delta(\omega + \omega') \,. \tag{4.4}$$

Consequently, we can write again equation (4.3) in terms of the power spectra

$$E(\omega) = F_0^2 \left[\frac{G(\omega)}{\omega^2 + \gamma^2} \right] \,, \tag{4.5}$$

which can be compared to observations in the solar wind plasmas. Therefore, the spectral energy is related to the spectral shape $G(\omega)$ of the external forcing.
In the simple case in which the magnetic fluctuations are generated by completely uncorrelated stochastic wave trains

$$\langle \xi_\omega \xi_{\omega'} \rangle = 2\pi\delta(\omega + \omega') \,,$$

the magnetic energy spectrum (4.5) becomes

$$E(\omega) \simeq \frac{F_0^2}{\omega^2 + \gamma^2} \,.$$

This Lorentzian function, of course, does not describe the magnetic energy density spectrum observed in the solar wind plasma at high frequencies.

At this point, we consider the case in which, close to the ion breakpoint, a variety of waves takes part in the process through wave-wave couplings, wave-particles interactions and dispersive effects. In this situation we can expect that the two-point correlations of the stochastic forcing term decay exponentially in time

$$\langle \xi(t')\xi(t) \rangle \sim \exp[-\lambda_0(t' - t)] \,, \tag{4.6}$$

where λ_0^{-1} is the correlation time. As a consequence, $\xi(t)$ can be considered, in a rough approximation, as a Brownian noise. From equation (4.6), using

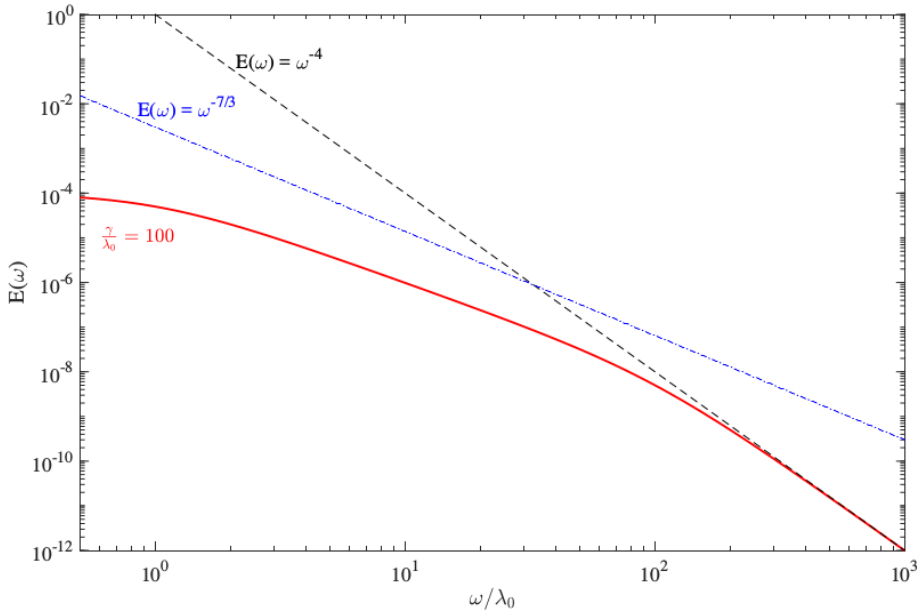

Figure 4.3: Magnetic power energy spectrum in function of ω/λ_0 for $\gamma/\lambda_0 = 100$ (red line). The blue dash-dotted line and the black dashed line indicate $E(\omega) \sim \omega^{-7/3}$ and $E(\omega) \sim \omega^{-4}$, respectively.

the inverse Fourier transform, we obtain

$$G(\omega) \simeq \frac{\lambda_0}{\omega^2 + \lambda_0^2} \,.$$

Substituting this functional shape in equation (4.5), through simple calculations, we have, for the magnetic energy power spectrum

$$E(\omega) \simeq \frac{\lambda_0 F_0^2}{(\omega^2 + \lambda_0^2)(\omega^2 + \gamma^2)} \,. \tag{4.7}$$

The correlation time λ_0^{-1} and the dissipation rate γ correspond to the low-frequency and high-frequency breakpoints, respectively, that is $\lambda_0 \approx \omega_\mathrm{i}$ and $\gamma \approx \omega_\mathrm{e}$. Equation (4.7) nicely reproduces the spectral properties observed in the interplanetary space at high frequencies ($\omega > \omega_\mathrm{i}$).

The power spectrum is shown in figure 4.3 as a function of ω/λ_0. We chose $\gamma/\lambda_0 = 100$ as this represents a typical value of the ratio of the two frequencies $\omega_\mathrm{e}/\omega_\mathrm{i}$ found in observations (Sahraoui et al., 2009).

It is important to note that equation (4.7), although it is not just a combination of two power laws, gives rise to two power law ranges compatible with those reported in observations by Sahraoui et al. (2009, 2013). The first one is obtained for frequencies $\lambda_0 \leq \omega \leq \gamma$, with a spectral slope close to $\alpha \simeq 7/3$,

while the second power law, with a slope of $\alpha \simeq 4$, for frequencies $\omega \geq \gamma$. Furthermore, the separation between the two spectral breakpoints is fixed by the ratio between the two frequencies but the slopes of the two power law ranges are independent of the parameters of the model.

We now consider the existence of a continuos distribution of relaxation rates λ, described by a probability of occurrence $dP(\lambda) \sim \lambda^{-\mu} d\lambda$. In this case, more realistic than the previous one, the power spectrum of the external forcing is calculated from the superposition of all the rates λ, leading to

$$G(\omega) = \int_{\lambda_0}^{\gamma} \frac{\lambda^{-\mu} d\lambda}{\omega^2 + \lambda^2} \simeq \frac{1}{\omega^{(1+\mu)}} \int_0^{\infty} \frac{x^{-\mu} dx}{1 + x^2} \simeq A\omega^{-(1+\mu)} \tag{4.8}$$

for $\gamma \gg \omega \gg \lambda_0$. The magnetic energy spectrum becomes

$$E(\omega) \sim AF_0^2 \left[\frac{\omega^{-(1+\mu)}}{\omega^2 + \gamma^2} \right] . \tag{4.9}$$

The same functional form was used by Sahraoui et al. (2013) to fit the magnetic energy spectra in the solar wind measured by Cluster, well reproducing the overall shape of the spectrum. Our model provides a physical interpretation of equation (4.9) as the result of a whole class of flicker noises $\xi(t)$, compatible with the excitation of sporadic wave trains.

When comparing the power spectra obtained from solar wind observations to those given by theoretical models, it is necessary, in general, to take into account that measurements are obtained in the spacecraft reference frame, which is in relative motion with respect to the plasma frame of the solar wind. According to the Doppler shift formula, the measured frequency in the spacecraft frame ω_{sc}, of a Fourier mode of wavevector $\mathbf{k}$ and frequency ω, is given by $\omega_{sc} = \omega + \mathbf{k} \cdot \mathbf{v}_{\rm SW}$, where $\mathbf{v}_{\rm SW}$ is the solar wind velocity. In the high frequency range two relevant situations can occur, depending on the ratio between the two terms at the right hand side. When the solar wind speed is slow enough, $|\omega| \gtrsim |\mathbf{k} \cdot \mathbf{v}_{\rm SW}|$ and this leads to a constant shift of the frequency spectrum to higher frequency, in the spacecraft frame, without changes in the scaling of the spectrum (Klein et al., 2014). Therefore, the scaling predictions of our model are still valid in this situation and the only change would be a shift of both low and high frequency breakpoints by a constant value Ω_0, namely $\omega_{\rm i} \approx \lambda_0 + \Omega_0$ and $\omega_{\rm e} \approx \gamma + \Omega_0$. The other significant case is the dispersive regime, when the plasma-frame frequency increases more rapidly than linearly and ω_{sc} is eventually dominated by the plasma-frequency term ($\omega_{sc} \approx \omega$). Also in this case, since $\omega_{sc} \approx \omega$, the spectra of our model can be directly compared to

those measured by spacecraft.
Problems would arise only if we wanted to map frequency spectra to wavenumber spectra, but this is not a aim of our work, as the nature of the model proposed here is such that high frequency magnetic fluctuations are described in the time/frequency domains and the spectra given by the model are frequency spectra. In other words, in our Brownian framework observations are not interpreted in terms of turbulence and no assumptions about dispersion relations, from plasma turbulence theory, are needed.

4.3.2 Fluctuation-Dissipation Theorem

The statistical properties of the fluctuations can be connected to the global properties of dissipation. In fact, from the Itô equation (4.1) we can derive a relation for the average energy of magnetic fluctuations, $\epsilon(t) = \langle b^2 \rangle$,

$$\frac{1}{2}\frac{d\epsilon}{dt} + \gamma\epsilon = F_0 \langle b(t)\xi(t) \rangle \,. \tag{4.10}$$

The relation, that connects the magnetic fluctuations with the random forcing term, can be obtained from equation (4.1) in the following way

$$b(t) = F_0 \int_0^t dt' \xi(t') \exp[\gamma(t'-t)] \,, \tag{4.11}$$

where we set $b(0) = 0$ for simplicity. Using relation (4.11) in equation (4.10), we obtain

$$\frac{d\epsilon}{dt} = -2\gamma\epsilon + 2F_0^2 G(t) \,, \tag{4.12}$$

where

$$G(t) = \int_0^t \langle \xi(s)\xi(t) \rangle e^{\gamma(s-t)} ds \,. \tag{4.13}$$

If $G(t \to \infty) \to G_0$ constant, there is a quasi-stationary solution $\epsilon_{\rm stat}$ for the magnetic energy and it is finite. In this case we have $\epsilon_{\rm stat} \simeq F_0^2 g(\gamma, \lambda)$, where the unknown function involves the dissipation rate and the correlation rates of the external forcing term.
We suppose that the stochastic medium is in a statistically stationary situation and consider a kind of statistical equilibrium at a temperature T corresponding to the second moment of the velocity distribution function measured by spacecraft. Then, we obtain

$$2F_0^2 g(\gamma, \lambda) \simeq \frac{1}{2} \int_{-\infty}^{\infty} v^2 f(v) dv \,. \tag{4.14}$$

From the definition of the magnetic energy power spectrum, using equation (4.5), we have

$$\langle b_\omega b_\omega^\star \rangle = \frac{F_0^2 G(\omega)}{\omega^2 + \gamma^2} = \int_0^\infty dt \langle b(t) b(0) \rangle \cos \omega t \,. \tag{4.15}$$

At equilibrium $\omega \simeq 0$ and $G(\omega) \simeq 1$, so that using relation (4.14) for F_0^2 in equation (4.15), we can write

$$2g(\gamma, \lambda)\gamma^2 \int_0^\infty dt \langle b(t) b(0) \rangle \simeq \frac{1}{2} \int_{-\infty}^\infty v^2 f(v) dv \,, \tag{4.16}$$

which represents a kind of Fluctuation-Dissipation Theorem (FDT) (Gardiner, 1997). According to this theorem, a spontaneous variation or fluctuation of a thermodynamic system is dissipated when the system returns to equilibrium, that is the response to small perturbations is linear. This relation is based on the hypothesis that the response of a system in thermodynamic equilibrium to a small applied force is the same as its response to a spontaneous fluctuation. Often the linear response takes the form of one or more exponential decays.
The implications of the FDT become more evident by remembering the definition of the β plasma parameter as the ratio between kinetic and magnetic pressure, so that

$$g(\gamma, \lambda)\gamma^2 \simeq F(\beta) \tag{4.17}$$

where $F(\beta)$ is an increasing function of β. In this study we consider a statistical equilibrium situation just to underline some consequences of the Fluctuation-Dissipation Theorem. A statistical equilibrium involving a maximal entropy is not strictly required from a mathematical point of view, because a kind of FDT, based on the response theory (Ruelle, 1998), can be found also in a stationary chaotic system with a given statistical distribution of orbits in the phase space, thus obtaining information on the fine structure of the attractor in the finite phase space (Lucarini, 2012).
The FDT relates the magnetic fluctuations, globally described here by the function $F(\beta)$, to the dissipative properties of the interplanetary medium at small scales, related to the function $g(\gamma, \lambda)$. The role of β in establishing the properties of the region of high-frequency region of fluctuations has been underlined in previous works (Leamon et al., 1999), and a relationship between the plasma β and dissipative properties is certainly plausible, as for example for Landau damping. In fact, the plasma β is proportional to the square of the thermal velocity and the maximum damping happens for particles which travel at the phase speed. As a consequence, the particles' bulk is more in-

volved in the wave-particle interactions the closer the phase speed is to the thermal speed.

In the case of correlated fluctuations, the Fluctuation-Dissipation Theorem relation can be expressed as

$$\gamma^2 \int_{\lambda_0}^{\gamma} g(\gamma, \lambda) \lambda^{-\mu} d\lambda \simeq F(\beta) \,. \tag{4.18}$$

When we consider a single correlation rate $\lambda = \lambda_0$, the relation (4.18) becomes

$$\frac{\gamma}{(\gamma - \lambda_0)} \simeq F(\beta) \,, \tag{4.19}$$

where, keeping γ fixed, since $F(\beta)$ increases with β, the difference between γ and λ_0 decreases as β increases. Sahraoui et al. (2013) found a double power law for low values of β plasmas. In our model this occurs when $F(\beta)$ is small and, therefore, the difference between the two breakpoints is large, giving rise to a clear double power law behavior.

Equation (4.19) indicates that for low-β plasmas the λ_0 break shifts towards lower frequencies, while the case of high values of the β parameter corresponds to a shift towards higher frequencies. This behavior has been observed in solar wind (Chen et al., 2014).
On the other side, the position of the high-frequency spectral breakpoint shifts towards higher frequencies, for high values of γ. This is counter-intuitive with respect to the interpretation of the steepening of the spectrum as due to a dissipative region in which small-scale fluctuations are generated through some turbulent cascade. In a turbulent environment, described by fluid equations, the fluctuations are produced by the cascade process and the inertial range breakpoint is defined by the dissipative cutoff, fixed by the local Reynolds number. In fact, the smaller the dissipative term in the Navier-Stokes or MHD equations, the higher the frequency of the cutoff. In this case we have an reversed situation, since the spectral properties of high-frequency fluctuations can be considered as a consequence of the FDT, which governes both fluctuations and dissipation, that are two ingredients of the same physical process.

4.3.3 Discussion

In this study we introduced a new framework to describe the dynamics at high frequency of magnetic fluctuations in the interplanetary space. Our model is rather different from the nonlinear energy cascade approach, used to describe the fluctuations at low frequency. The same type of phenomenology

was used by Kraichnan (1959) to explain the susceptivity of the fluctuations under the action of random forcing, within the Direct Interaction Approximation of the complex nonlinear mode couplings generated by the fluid turbulent cascade.
Our approach does not exclude all the complex dynamics deriving from plasma physics. In fact, kinetic plasma physics describes all the microscopic characteristics involved in the dynamics of fluctuations, that are the birth of the many modes involved, their nonlinear coupling, their dispersive properties, and the collisionless dissipative processes which lead to anomalous plasma-heating. Consequently, the absence of a universal structure makes the description of the fluctuations at small scale dependent on the specific microscopic case, often with contrasting consequences in discriminating or excluding different interpretations of the same observation.

In this work the high-frequency fluctuations occurring in the interplanetary space are described through a Brownian-like approach, thus providing a unifying framework which, independently of the specific microscopic plasma dynamics, can account for the gross features of the up-to-date observations of spectral properties of high-frequency fluctuations in the interplanetary space.

Conclusions

The main topic of this thesis is the study of energetic protons at interplanetary shocks. We investigated the possible connection between energetic particle fluxes and magnetic turbulence around the shocks, and analyzed the particle energy spectra to the aim of establishing which are the most probable acceleration mechanisms at work for different shock configurations. This study was carried on by using Stereo A data over the period $2009 - 2016$.
We selected only shocks at which an effective enhancement in proton flux is observed at energies $4 - 6$ MeV and divided them into two lists according to whether the peak is near (List 1) or distant from the shock (List 2).
From the correlation analysis (parametric and nonparametric) between the particle flux enhancements and the magnetic field turbulence in the upstream and downstream regions of interplanetary shocks, it is evident that the increases are more pronounced for the events of the List 1 (near the shock region).
In particular, when a SEP is in progress at the shock arrival, we obtain high correlation for R and T components (those in the equatorial plane of the Sun) and for magnitude of the magnetic field in the downstream region; whereas, in the cases of NO SEP events, we get a significant anticorrelation downstream of the shock.

The study of energy spectra indicates that different mechanisms could account for the acceleration of the particles in the energy range from few tens of keV up to hundreds of MeV.
In the case of spectra relating to the ESP events in which the solar energetic particles are not present at the shock passage (NO SEP), we obtain a power law, typical of the classical diffusive shock acceleration.
Instead, when we consider ESPs associated with SEP events, the shape of the spectra is different depending on the shock angle. In fact, for the two parallel shocks in our dataset, the best fit is a double power law, which indicates that the DSA is at work, but potentially modified by SA (stochastic acceleration) at higher energies. For quasi-perpendicular shocks the results show that the

particle spectra associated with shock acceleration are well reproduced by the Weibull functional form, at least in the high energy range. The particle spectra obtained from the fit procedure are Weibull distributions with γ values that are in agreement with those expected ($\gamma = 1/2$).
SSA (shock surfing acceleration) seem to be a viable mechanism to explain the high energy tail of the particle spectra at interplanetary quasi-perpendicular shocks. Moreover, we found a good correlation in the intermediate energy range $4-6$ MeV between the proton flux enhancements and the magnetosonic Mach number ($\mathrm{M_{ms}}$) and the shock angle (θ_{Bn}), that are two critical parameters in the SSA mechanism.
Nevertheless, a possible role of the stochastic acceleration at shock waves in case of momentum anomalous diffusion cannot be excluded.
Further efforts are needed to better understand the details of the microphysics and turbulence around the shock front and how it can affect the trapping and acceleration of energetic particles.

Finally, concerning the dynamics at high frequency of magnetic fluctuations in the interplanetary space we introduced a Brownian-like approach, that is different from the nonlinear energy cascade approach, used to describe the fluctuations at low frequency. Our model provides a unifying framework which, independently of the specific microscopic plasma dynamics, can account for the gross features of the up-to-date observations of spectral properties of high-frequency fluctuations in the interplanetary space. In fact, it does not exclude all the complex dynamics deriving from plasma physics, that is the origin of the many modes involved, their nonlinear coupling, their dispersive properties, and the collisionless dissipative processes which lead to anomalous plasma-heating.

Bibliography

Afanasiev, A., Vainio, R., and Kocharov, L. (2014). "The effect of stochastic re-acceleration on the energy spectrum of shock-accelerated protons". In: *Astrophysical Journal* 790, p. 36.

Alexandrova, O., Lacombe, C., Mangeney, A., Grappin, R., and Maksimovic, M. (2012). "Solar wind turbulent spectrum at plasma kinetic scales". In: *Astrophysical Journal* 760, p. 121.

Bale, S.D., Kellogg, P.J., Mozer, F.S., Horbury, T.S., and Reme, H. (2005). "Measurement of the Electric Fluctuation Spectrum of Magnetohydrodynamic Turbulence". In: *Physical Review Letters* 94, p. 215002.

Band, D., Matteson, J., Ford, L., Schaefer, B., Palmer, D., Teegarden, B., Cline, T., Briggs, M., Paciesas, W., Pendleton, G., Fishman, G., Kouveliotou, C., Meegan, C., Wilson, R., and Lestrade, P. (1993). "BATSE observations of gamma-ray burst spectra. I. Spectral diversity". In: *Astrophysical Journal* 413, p. 281.

Bavassano, B., Dobrowolny, M., Fanfoni, G., Mariani, F., and Ness, N.F. (1982). "Statistical properties of MHD fluctuations associated with high-speed streams from Helios-2 observations". In: *Solar Physics* 78, p. 373.

Biskamp, D. (2003). *Magnetohydrodynamic turbulence*. Cmabridge University Press.

Blandford, R. and D. Eichler (1987). "Particle acceleration at astrophysical shocks: A theory of cosmic ray origin". In: *Physical Reports* 154, p. 1.

Bouchet, F., Cecconi, F., and Vulpiani, A. (2004). "Minimal Stochastic Model for Fermi's Acceleration". In: *Physical Review Letters* 92 (4), p. 040601.

Bruno, R. and V. Carbone (2013). "The Solar Wind as a Turbulence Laboratory". In: *Living Reviews of Solar Physics* 10.

Bruno, R. and V. Carbone (2016). *Turbulence in the Solar wind*. Lecture Notes in Physics. Springer-Verlag.

Bruno, R., Carbone, V., Vörös, Z., D'Amicis, R., Bavassano, B., Cattaneo, M.B., Mura, A., Milillo, A., Orsini, S., Veltri, P., Sorriso-Valvo, L., Zhang, T., Biernat, H., Rucker, H., Baumjohann, W., Jankovičová, D., and Kovács,

P. (2009). "Coordinated Study on Solar Wind Turbulence During the Venus-Express, ACE and Ulysses Alignment of August 2007". In: *Earth Moon Planets* 104, p. 101.

Burlaga, L.F. (1991). "Multifractal structure of speed fluctuations in recurrent streams". In: *Geophysical Research Letters* 18 (69), p. 1651.

Burlaga, L.F. (1995). *Interplanetary Magnetohydrodynamics*. Oxford University Press.

Carbone, V. (1993). "Cascade model for intermittency in fully developed magnetohydrodynamic turbulence". In: *Physical Review Letters* 71, p. 1546.

Chapman, S. and V.C.A. Ferraro (1931). "A new theory of magnetic storms". In: *Terrestrial Magnetism and Atmospheric Electricity* 36, p. 171.

Chen, C.H.K., Leung, L., Boldyrev, S., Maruca, B.A., and Bale, S.D. (2014). "Ion-scale spectral break of solar wind turbulence at high and low beta". In: *Geophysical Research Letters* 41, p. 8081.

Claßen, H.-T., Mann, G., Forsyth, R.J., and Keppler, E. (1999). "Low frequency plasma turbulence and high energy particles at CIR-related shock waves". In: *Astronomy and Astrophysics* 347, p. 313.

Coleman, P.J. Jr. (1968). "Turbulence, viscosity, and dissipation in the solar-wind plasma". In: *Astrophysical Journal* 153, p. 361.

Davis, T.N. and M. Sugiura (1966). "Auroral electrojet activity index AE and its universal time variations". In: *Journal of Geophysical Research* 71 (3), p. 785.

Decker, R.B. (1988). "Computer modelling of test particle acceleration at oblique shocks". In: *Space Science Review* 48, p. 195.

Desai, M. and J. Giacalone (2016). "Large gradual solar energetic particle events". In: *Living Reviews of Solar Physics* 13.

Dobrowolny, M., Mangeney, A., and Veltri, P. (1980). "Properties of magnetohydrodynamic turbulence in the solar wind". In: *Astronomy and Astrophysics* 83, p. 26.

Dresing, N., Theesen, S., Klassen, A., and Heber, B. (2016). "Efficiency of particle acceleration at interplanetary shocks: Statistical study of STEREO observations". In: *Astronomy and Astrophysics* 588, A17.

Dröge, W. (2000). In: *ASP Conf. Series*. Ed. by Ramaty, R. and Mandzhavidze, N. Vol. 206, p. 191.

Ellison, D.C. and R. Ramaty (1985). "Shock acceleration of electrons and ions in solar flares". In: *Astrophysical Journal* 298, p. 400.

Fermi, E. (1949). "On the Origin of the Cosmic Radiation". In: *Physical Review* 75, p. 1169.

Frisch, U. and D. Sornette (1997). "Extreme deviations and applications". In: *Journal of Physics I* 7, p. 1155.

Frisch, U., Pouquet, A., Leorat, J., and Mazure, A. (1975). "Possibility of an inverse cascade of magnetic helicity in magnetohydrodynamic turbulence". In: *Journal of Fluid Mechanics* 68, p. 769.

Gardiner, C.W. (1997). *Handbook of Stochastic Methods*. Springer-Verlag.

Garrett, H.B., Schwank, D.C., and DeForest, S.E. (1981a). "A statistical analysis of the low-energy geosynchronous plasma environment. I. Electrons". In: *Planetary and Space Science* 29, p. 1021.

Garrett, H.B., Schwank, D.C., and DeForest, S.E. (1981b). "A statistical analysis of the low-energy geosynchronous plasma environment. II. Ions". In: *Planetary and Space Science* 29, p. 1045.

Giacalone, J. (2012). "Energetic charged particles associated with strong interplanetary shocks". In: *Astrophysical Journal* 761, p. 28.

Gotoh, T. and D. Fukayama (2001). "Pressure spectrum in homogeneous turbulence". In: *Physical Review Letters* 86, p. 3775.

Hamilton, D.C., Gloeckler, G., Ipavich, F.M., Stüdemann, W., Wilken, B., and Kremser, G. (1988). "Ring current development during the great geomagnetic storm of February 1986". In: *Journal of Geophysical Research: Space Physics* 93 (a12), p. 14343.

Howes, G.G., Dorland, W., Cowley, S.C., Hammett, G.W., Quataert, E., Schekochihin, A.A., and Tatsuno, T. (2008). "Kinetic Simulations of Magnetized Turbulence in Astrophysical Plasmas". In: *Physical Review Letters* 100, p. 065004.

Iroshnikov, P.S. (1963). "Turbulence of a Conducting Fluid in a Strong Magnetic Field". In: *Soviet Astronomy Letters* 7, p. 566.

Jian, L.K., Russell, C.T., Luhmann, J.G., Galvin, A.B., and Simunac, K.D.C. (2013). In: *AIP Conf. Series*. Ed. by Zank, G.P., Borovsky, J., and Bruno, R., et al., vol. 1539, p. 191.

Kallenrode, M.B. (1996). "A statistical survey of 5-MeV proton events at interplanetary shocks". In: *Journal of Geophysical Research: Space Physics* 101 (a11), p. 24393.

Kivelson, M.G. and C.T. Russell (1995). *Introduction to space physics*. Cmabridge University Press.

Klein, K.G., Howes, G.G., and TenBarge, J.M. (2014). "The violation of the Taylor hypothesis in measurements of solar wind turbulence". In: *Astrophysical Journal Letters* 790, p. L20.

Kolmogorov, A.N. (1941). "The local structure of turbulence in incompressible viscous fluid for very large Reynolds numbers". In: *Doklady Akademii Nauk SSSR* 30, p. 301.

Kraichnan, R.H. (1959). "The structure of isotropic turbulence at very high Reynolds numbers". In: *Journal of Fluid Mechanics* 5, p. 497.

Kraichnan, R.H. (1965). "Inertial Range Spectrum of Hydromagnetic Turbulence". In: *Physics of Fluids* 8, p. 1385.

Landi Degl'Innocenti, E. (2008). *Fisica Solare*. Milano: Springer-Verlag Italia.

Lario, D., Ho, G.C., Decker, R.B., Roelof, E.C., Desai, M.I., and Smith, C.W. (2003). "ACE Observations of Energetic Particles Associated with Transient Interplanetary Shocks". In: *AIP Conference Proceedings*. Vol. 679, p. 640.

Laurenza, M., Consolini, G., Storini, M., and Damiani, A. (2013). In: *AIP Conf. Series*. Ed. by Zank, G.P., Borovsky, J., and Bruno, R., et al., vol. 1539, p. 219.

Laurenza, M., Consolini, G., Storini, M., and Damiani, A. (2015). "Low frequency plasma turbulence and high energy particles at CIR-related shock waves". In: *Journal of Physics: Conference Series* 632, p. 012066.

Leamon, R.J., Smith, C.W., Ness, N.F., Matthaeus, W.H., and Wong, H.K. (1998). "Observational constraints on the dynamics of the interplanetary magnetic field dissipation range". In: *Journal of Geophysical Research* 103, p. 4775.

Leamon, R.J., Smith, C.W., Ness, N.F., and Wong, H.K. (1999). "Dissipation range dynamics: Kinetic Alfvèn waves and the importance of β_e". In: *Journal of Geophysical Research* 104, p. 22331.

Lee, M.A. (1983). "Coupled hydromagnetic wave excitation and ion acceleration at interplanetary traveling shocks". In: *Journal of Geophysical Research* 88, p. 6109.

Lee, M.A., Shapiro, V.D., and Sagdeev, R.Z. (1996). "Pickup ion energization by shock surfing". In: *Journal of Geophysical Research* 101, p. 4777.

Lee, M.A., Mewaldt, R.A., and Giacalone, J. (2012). "Shock Acceleration of Ions in the Heliosphere". In: *Space Science Review* 173, p. 247.

Lever, E.L., Quest, K.B., and Shapiro, V.D. (2001). "Shock surfing vs. shock drift acceleration". In: *Geophysical Research Letters* 28, p. 1367.

Lucarini, V. (2012). "Stochastic perturbations to dynamical systems: a response theory approach". In: *Journal of Statistical Physics* 146, p. 774.

Marsch, E. (2006). "Kinetic Physics of the Solar Corona and Solar Wind". In: *Living Review Solar Physics* 3, p. 1.

Matthaeus, W.H., Servidio, S., and Dmitruk, P. (2008). "Comment on 'Kinetic Simulations of Magnetized Turbulence in Astrophysical Plasmas'". In: *Physical Review Letters* 101, p. 149501.

Mewaldt, R.A., Cohen, C.M.S., Labrador, A.W., Leske, R.A., Mason, G.M., Desai, M.I., Looper, M.D., Mazur, J.E., Selesnick, R.S., and Haggerty, D.K. (2005). "Proton, helium , and electron spectra during the large solar particle events of October-November 2003". In: *Journal of Geophysical Research* 110 (A09S18).

Mewaldt, R.A., Looper, M.D., Cohen, C.M.S., Haggerty, D.K., Labrador, A.W., Leske, R.A., Mason, G.M., Mazur, J.E., and von Rosenvinge, T.T. (2012). "Energy Spectra, Composition, and Other Properties of Ground-Level Events During Solar Cycle 23". In: *Space Science Review* 171, p. 97.

Narita, Y. (2018). "Space-time structure and wavevector anisotropy in space plasma turbulence". In: *Living Review Solar Physics* 15, p. 2.

Narita, Y., Gary, S.P., Saito, S., Glassmeier, K.-H., and Motschmann, U. (2011). "Dispersion relation analysis of solar wind turbulence". In: *Geophysical Research Letters* 38, p. L05101.

Obukhov, A.M. (1962). "Some specific features of atmospheric turbulence". In: *Journal of Fluid Mechanics* 13, p. 77.

Ohsawa, Y. (1987). "Acceleration of energetic ions by a nearly perpendicular interplanetary shock". In: *Geophysical Research Letters* 14.2, p. 95.

Pallocchia, G., Laurenza, M., and Consolini, G. (2017). "On Weibull's Spectrum of Nonrelativistic Energetic Particles at IP Shocks: Observations and Theoretical Interpretation". In: *Astrophysical Journal* 837, p. 158.

Parker, E.N. (1958). "Dynamics of interplanetary gas and magnetic fields". In: *Astrophysical Journal* 128, p. 664.

Parker, E.N. (1961). "Sudden Expansion of the Corona Following a Large Solar Flare and the Attendant Magnetic Field and Cosmic Ray Effects". In: *Astrophysical Journal* 133, p. 1014.

Perri, S., Lepreti, F., Carbone, V., and Vulpiani, A. (2007). "Position and velocity space diffusion of test particles in stochastic electromagnetic fields". In: *Europhysics Letters* 78, p. 40003.

Perri, S., Yordanova, E., Carbone, V., VeltriP., Sorriso-Valvo, L., Bruno, R., and André, M. (2009). "Magnetic turbulence in space plasmas: Scale-dependent effects of anisotropy". In: *Journal of Geophysical Research* 114, p. 2102.

Perschke, C., Narita, Y., Motschmann, U., and Glassmeier, K.-H. (2016). "Observational Test for a Random Sweeping Model in Solar Wind Turbulence". In: *Physical Review Letters* 116, p. 125101.

Pesses, M.E., Decker, R.B., and Armstrong, T.P. (1982). "The acceleration of charged particles in interplanetary shock waves". In: *Space Science Review* 32, p. 185.

Politano, H. and A. Pouquet (1998). "von Kármán–Howarth equation for magnetohydrodynamics and its consequences on third-order longitudinal structure and correlation functions". In: *Physical Review E* 57, R21.

Reames, D.V. (1999). "Particle acceleration at the Sun and in the heliosphere". In: *Space Science Review* 90, p. 412.

Reynolds, O. (1883). "An Experimental Investigation of the Circumstances which determine whether the Motion of Water shall be Direct or Sinuous, and the Law of Resistance in Parallel Channels". In: *Philosophical Transactions of the Royal Society of London* 174, p. 935.

Richardson, J.D., Liu, Y., Wang, C., and Burlaga, L.F. (2006). "ICMES at very large distances". In: *Advances in Space Research* 38.3, p. 528.

Richardson, L.F. (1922). *Weather prediction by numerical process*. Cmabridge University Press.

Ruelle, D. (1998). "General linear response formula in statistical mechanics and the Fluctuation-Dissipation Theorem far from equilibrium". In: *Physics Letters A* 245, p. 855.

Sagdeev, R.Z. (1966). "Cooperative phenomena and shock waves in collisionless plasmas". In: *Reviews of Plasma Physics* 4, p. 23.

Sahraoui, F., Goldstein, M.L., Robert, P., and Khotyaintsev, Yu.V. (2009). "Evidence of a Cascade and Dissipation of Solar-Wind Turbulence at the Electron Gyroscale". In: *Physical Review Letters* 102, p. 231102.

Sahraoui, F., Huang, S.Y., Belmont, G., Goldstein, M.L., Retinò, A., Robert, P., and De Patoul, J. (2013). "Scaling of the electron dissipation range of solar wnd turbulence". In: *Astrophysical Journal* 777, p. 15.

Servidio, S., Matthaeus, W.H., and Carbone, V. (2008). "Statistical properties of ideal three-dimensional Hall magnetohydrodynamics: The spectral structure of the equilibrium ensemble". In: *Physics of Plasmas* 15, p. 042314.

Sorriso-Valvo, L., Marino, R., Carbone, V., Noullez, A., Lepreti, F., Veltri, P., Bruno, R., Bavassano, B., and Pietropaolo, E. (2007). "Observation of Inertial Energy Cascade in Interplanetary Space Plasma". In: *Physical Review Letters* 99, p. 115001.

Sreenivasan, K.R. (1995). "On the universality of the Kolmogorov constant". In: *Physics of Fluids* 7, p. 2778.

Stone, E.C., Burlaga, L.F., Ness, N.F., Acuña, M.H., Lepping, R.P., Connerney, J.E.P., and McDonald, F.B. (2005). "Crossing the Termination Shock

into the Heliosheath: Magnetic Fields". In: *Science* 309.5743, pp. 2027–2029.

Tylka, A.J., Cohen, C.M.S., Dietrich, W.F., Lee, M.A., Maclennan, C.G., Mewaldt, R.A., Ng, C.K., and Reames, D.V. (2005). "Shock geometry, seed populations, and the origin of variable elemental composition at high energies in large gradual solar particle events". In: *Astrophysical Journal* 625, p. 474.

Van Nes, P., Reinhard, R., Sanderson, T.R., and Wenzel, K.P. (1984). "The energy spectrum of 35- to 1600-keV proton associated with interplanetary shocks". In: *Journal of Geophysical Research* 89, p. 2122.

Webb, G.M., Zank, G.P., Ko, C.M., and Donohue, D.J. (1995). "Multidimensional Green's functions and the statistics of diffusive shock acceleration". In: *Astrophysical Journal* 453, p. 178.

Weibull, W. (1951). "A statistical distribution function of wide applicability". In: *Journal of Applied Mechanics* 18, p. 293.

Yuen, C.K. and D. Fraser (1979). *Digital spectral analysis*. Csiro, Melbourne.

Zank, G.P., Pauls, H.L., Cairns, I.H., and Webb, G.M. (1996). "Interstellar pickup ions and quasi-perpendicular shocks: Implications for the termination shock and interplanetary shocks". In: *Journal of Geophysical Research* 101, p. 457.

Zank, G.P., Li, G., Florinski, V., Hu, Q., Lario, D., and Smith, C.W. (2006). "Particle acceleration at perpendicular shock waves: Model and observations". In: *Journal of Geophysical Research* 111 (A06108).